

Spatial, spin, and charge symmetry projections for a Fermi-Hubbard model on a quantum computer

Kazuhiro Seki¹ and Seiji Yunoki^{1,2,3,4}

¹*Quantum Computational Science Research Team, RIKEN Center for Quantum Computing (RQC), Saitama 351-0198, Japan*

²*Computational Quantum Matter Research Team, RIKEN Center for Emergent Matter Science (CEMS), Saitama 351-0198, Japan*

³*Computational Materials Science Research Team, RIKEN Center for Computational Science (R-CCS), Hyogo 650-0047, Japan*

⁴*Computational Condensed Matter Physics Laboratory,*

RIKEN Cluster for Pioneering Research (CPR), Saitama 351-0198, Japan

(Dated: March 11, 2022)

We propose an extended version of the symmetry-adapted variational-quantum-eigensolver (VQE) and apply it to a two-component Fermi-Hubbard model on a bipartite lattice. In the extended symmetry-adapted VQE method, the Rayleigh quotient for the Hamiltonian and a parametrized quantum state in a properly chosen subspace is minimized within the subspace and is optimized among the variational parameters implemented on a quantum circuit to obtain variationally the ground state and the ground-state energy. The corresponding energy derivative with respect to a variational parameter is expressed as a Hellmann-Feynman-type formula of a generalized eigenvalue problem in the subspace, which thus allows us to use the parameter-shift rules for its evaluation. The natural-gradient-descent method is also generalized to optimize variational parameters in a quantum-subspace-expansion approach. As a subspace for approximating the ground state of the Hamiltonian, we consider a Krylov subspace generated by the Hamiltonian and a symmetry-projected variational state, and therefore the approximated ground state can restore the Hamiltonian symmetry that is broken in the parametrized variational state prepared on a quantum circuit. We show that spatial symmetry operations for fermions in an occupation basis can be expressed as a product of the nearest-neighbor fermionic SWAP operations on a quantum circuit. We also describe how the spin and charge symmetry operations, i.e., rotations, can be implemented on a quantum circuit. By numerical simulations, we demonstrate that the spatial, spin, and charge symmetry projections can improve the accuracy of the parametrized variational state, which can be further improved systematically by expanding the Krylov subspace without increasing the number of variational parameters.

I. INTRODUCTION

Recent technological advances in quantum devices [1–11] have suggested that quantum computation of quantum physics and chemistry systems [12] is becoming a reality in the not-so-distant future [13, 14]. Currently available quantum computers are, however, prone to noise and hence the size of a quantum circuit to be reliably executed is limited. Such quantum computers are called noisy intermediate-scale quantum (NISQ) computers [15]. Despite the limitation, NISQ computers with 50-100 qubits are anticipated to show advantage over classical computers with the best known algorithm for particular tasks (for example, see Refs. [9, 10, 16]). Thus, in parallel with research to accomplish fault-tolerant quantum computers, for which an increasing number of experimental developments towards realization of logical qubit operations has been reported recently [17–21], it is of importance to find practical applications of NISQ computers for further stimulating progress in the field of quantum computing. To this end, several quantum-classical hybrid algorithms and error mitigation schemes have been developed [22–25].

The variational-quantum eigensolver (VQE) [26–29] is one of the potentially promising quantum-classical hybrid schemes for solving eigenvalue problems in quantum chemistry and quantum physics with NISQ computers. For recent reviews on variational quantum algorithms, see for example Refs. [30–32]. In the VQE, the expectation value of a Hamiltonian of interest with respect to a variational state represented on a parametrized quantum circuit, i.e., the variational energy, is evaluated with a quantum computer, while variational pa-

rameters are optimized by minimizing the variational energy on a classical computer. Depending on the form of variational states and the assignment of tasks for quantum and classical computers, several variants of the VQE scheme have been proposed. For example, VQE-type approaches based on the quantum-subspace expansion (QSE) [33] performs subspace diagonalization in an appropriately chosen subspace to approximate the target state(s) (e.g. the ground state) better than the conventional VQE scheme, at a cost of polynomial numbers of additional measurements [34, 35]. Aiming at a systematic construction of the subspace, a Krylov subspace [36] generated by properly chosen initial states with a real-time evolution operator [37–39], an imaginary-time evolution operator [40, 41], or a Hamiltonian [42] is often adopted.

In addition, to exploit the Hamiltonian symmetry, several variants or extensions of the VQE approach have been proposed. For example, we have proposed the symmetry-adapted VQE (SAVQE) method to encompass the Hamiltonian symmetry in the VQE scheme [43]. In the SAVQE method, the symmetry that is broken in the variational state generated on a parametrized quantum circuit is restored with a symmetry-projection operator. The nonunitarity of the projection operator is treated classically as a post processing with increasing the number of measurements, a similar idea for treating Jastrow-type correlators reported earlier in Ref. [44]. Moreover, related schemes have been employed to restore symmetry in a continuous group such as the SU(2) total-spin conservation [45, 46] and the U(1) particle-number conservation [47, 48], where the integral over continuous parameters of the group in the projection operator is properly discretized.

Concerning the translational symmetry of periodic systems, another VQE-type scheme has been proposed to formulate directly in the reciprocal space [49–51]. Furthermore, in a different VQE variant, an appropriate penalty term is introduced into a cost function to obtain an eigenstate of the Hamiltonian in a desired symmetry sector [52, 53]. It should also be noted that the Hamiltonian symmetry can also be utilized to mitigate errors due to different noise channels [24]. Remarkably, recent experiments have demonstrated a significant improvement for mitigating errors in a VQE simulation of a Fermi-Hubbard model by an error mitigation technique based on the Hamiltonian symmetry, including spin- and particle-number conservations, time-reversal symmetry, particle-hole symmetry, and spatial symmetry [14].

In this paper, we propose a QSE-based VQE method that incorporates the symmetry of Hamiltonian. The main idea is based on the SAVQE method [43] and the quantum power method (QPM) [42], both of which have been developed recently by the present authors. In the proposed method, we construct a Krylov subspace by multiplying Hamiltonian power onto a quantum state that is obtained by applying the symmetry-projection operators to a single variational state prepared on a parametrized quantum circuit. We then perform a subspace diagonalization by minimizing the Rayleigh quotient for the Hamiltonian and the quantum states in the Krylov subspace, and obtain the lowest eigenvalue of the generalized eigenvalue problem that depends on the variational parameters. The variational parameters are optimized so as to minimize the lowest eigenvalue of the generalized eigenvalue problem, which gives us the variational ground-state energy with the optimal set of variational parameters that represents the variational ground state. Considering a two-component Fermi-Hubbard model in a ladder lattice structure, we numerically demonstrate the proposed method by showing that the estimated ground-state energy as well as the ground-state fidelity can be improved by the spatial, spin, and charge symmetry projections, and they are further improved systematically with expanding the subspace without increasing the number of variational parameters.

The rest of this paper is organized as follows. In Sec. II, we briefly summarize a general formalism of the QSE method that is relevant for our purpose. In Sec. III, we formulate the natural-gradient-descent (NGD) method for the QSE scheme, and we describe how the corresponding energy gradient and the Fubini-Study metric tensor can be evaluated with a quantum computer using the parameter-shift rule. We then describe in Sec. IV the Krylov-extended SAVQE by introducing the Krylov subspace generated by the Hamiltonian and a symmetry-projected variational state. In Sec. V, we define the Fermi-Hubbard model on a bipartite lattice, and we briefly review its spatial, spin, and charge symmetry. We then describe the corresponding symmetry-projection operators. In Sec. VI, we first show how the symmetry operations for a fermion model in general can be implemented on a quantum circuit, and then we explain the case of the spin and charge symmetry operations. In Sec. VII, we numerically demonstrate the proposed method for the Fermi-Hubbard model. A conclusion and a discussion are given in Sec. VIII. Additional details on

the NGD method and the fermionic symmetry operations are provided in Appendixes A and B, respectively. Matrix representations of typical two-qubit two-level unitary gates for quantum many-body systems, such as the Givens-rotation gate and the Bogoliubov-transformation gate, are provided in Appendix C. A simple parallelization scheme for classical simulation of the VQE method is described in Appendix D. A remark on the normalization factor of the symmetry-projected quantum state is made in Appendix E. Further numerical results for a different type of variational states are discussed in Appendix F.

II. FORMALISM OF QUANTUM-SUBSPACE EXPANSION

A. Trial state and variational principle

Consider a subspace

$$\mathcal{U} = \text{span}(|u_0\rangle, |u_1\rangle, \dots, |u_{d_{\mathcal{U}}-1}\rangle) \quad (1)$$

with $\dim \mathcal{U} \equiv d_{\mathcal{U}}$. The basis states $\{|u_i\rangle\}_{i=0}^{d_{\mathcal{U}}-1}$ should be linearly independent of each other but they are not necessarily orthonormalized. We assume that $|u_i\rangle$ has a form of

$$|u_i(\theta)\rangle = \hat{O}_i |\psi(\theta)\rangle, \quad (2)$$

where $|\psi(\theta)\rangle$ is a variational state (ansatz) parametrized by a set of N_v variational parameters $\theta = \{\theta_k\}_{k=1}^{N_v}$, assuming they are real, and \hat{O}_i is an operator independent of the variational parameters. \hat{O}_i is not necessarily unitary but it is assumed to be given as a linear combination of unitary operators. Note that by definition, the parametrized part $|\psi(\theta)\rangle$ is common to all $\{|u_i(\theta)\rangle\}_{i=0}^{d_{\mathcal{U}}-1}$ in Eq. (2).

We now intend to approximate the exact ground state $|\Psi_0\rangle$ of the Hamiltonian $\hat{\mathcal{H}}$ within the subspace \mathcal{U} . This can be done simply by assuming that a trial state $|\Psi_{\mathcal{U}}(\theta)\rangle$ for approximating the ground state $|\Psi_0\rangle$ is given by

$$|\Psi_{\mathcal{U}}(\theta)\rangle = \sum_{i=0}^{d_{\mathcal{U}}-1} v_i(\theta) |u_i(\theta)\rangle \quad (3)$$

in the subspace \mathcal{U} , where $\mathbf{v}(\theta) = \{v_i(\theta)\}_{i=0}^{d_{\mathcal{U}}-1}$ are coefficients to be determined. According to the variational principle, the optimal variational parameters θ_{opt} are obtained by minimizing the expectation value of the Hamiltonian $\hat{\mathcal{H}}$, i.e., the variational energy, with respect to both θ and $\mathbf{v}(\theta)$:

$$\theta_{\text{opt}} \equiv \arg \min_{\theta} \left\{ \min_{\mathbf{v}(\theta)} \left\{ \frac{\langle \Psi_{\mathcal{U}}(\theta) | \hat{\mathcal{H}} | \Psi_{\mathcal{U}}(\theta) \rangle}{\langle \Psi_{\mathcal{U}}(\theta) | \Psi_{\mathcal{U}}(\theta) \rangle} \right\} \right\}. \quad (4)$$

B. Subspace diagonalization

Let us consider the optimization with respect to $\mathbf{v}(\theta)$ for a given set of variational parameters θ in Eq. (4) and denote the optimal coefficients as $\mathbf{v}_0(\theta) \equiv \{v_{i,0}(\theta)\}_{i=0}^{d_{\mathcal{U}}-1}$, i.e.,

$$\mathbf{v}_0(\theta) = \arg \min_{\mathbf{v}(\theta)} \left\{ \frac{\langle \Psi_{\mathcal{U}}(\theta) | \hat{\mathcal{H}} | \Psi_{\mathcal{U}}(\theta) \rangle}{\langle \Psi_{\mathcal{U}}(\theta) | \Psi_{\mathcal{U}}(\theta) \rangle} \right\}. \quad (5)$$

The optimal coefficients $\mathbf{v}_0(\boldsymbol{\theta})$ subject to a normalization condition, e.g., $\langle \Psi_{\mathcal{U}}(\boldsymbol{\theta}) | \Psi_{\mathcal{U}}(\boldsymbol{\theta}) \rangle = 1$, can be determined by solving the generalized eigenvalue problem [42]

$$\mathbf{H}(\boldsymbol{\theta})\mathbf{v}_0(\boldsymbol{\theta}) = E_0(\boldsymbol{\theta})\mathbf{S}(\boldsymbol{\theta})\mathbf{v}_0(\boldsymbol{\theta}), \quad (6)$$

where $\mathbf{H}(\boldsymbol{\theta})$ is the Hamiltonian matrix with its element

$$[\mathbf{H}(\boldsymbol{\theta})]_{ij} = \langle u_i(\boldsymbol{\theta}) | \hat{\mathcal{H}} | u_j(\boldsymbol{\theta}) \rangle = \langle \psi(\boldsymbol{\theta}) | \hat{\mathcal{O}}_i^\dagger \hat{\mathcal{H}} \hat{\mathcal{O}}_j | \psi(\boldsymbol{\theta}) \rangle, \quad (7)$$

$\mathbf{S}(\boldsymbol{\theta})$ is the overlap matrix with its element

$$[\mathbf{S}(\boldsymbol{\theta})]_{ij} = \langle u_i(\boldsymbol{\theta}) | u_j(\boldsymbol{\theta}) \rangle = \langle \psi(\boldsymbol{\theta}) | \hat{\mathcal{O}}_i^\dagger \hat{\mathcal{O}}_j | \psi(\boldsymbol{\theta}) \rangle, \quad (8)$$

and $E_0(\boldsymbol{\theta})$ is the smallest eigenvalue. The trial state

$$|\Psi_{\mathcal{U}}^{(0)}(\boldsymbol{\theta})\rangle \equiv \sum_{i=0}^{d_{\mathcal{U}}-1} v_{i,0}(\boldsymbol{\theta}) |u_i(\boldsymbol{\theta})\rangle \quad (9)$$

with $[v_0]_i = v_{i,0}$ being the i th entry of the corresponding eigenvector in Eq. (6) is normalized as long as the eigenvector $\mathbf{v}_0(\boldsymbol{\theta})$ is normalized with respect to $\mathbf{S}(\boldsymbol{\theta})$, i.e.,

$$\langle \Psi_{\mathcal{U}}^{(0)}(\boldsymbol{\theta}) | \Psi_{\mathcal{U}}^{(0)}(\boldsymbol{\theta}) \rangle = \mathbf{v}_0^\dagger(\boldsymbol{\theta}) \mathbf{S}(\boldsymbol{\theta}) \mathbf{v}_0(\boldsymbol{\theta}) = 1, \quad (10)$$

where $\mathbf{v}_0^\dagger(\boldsymbol{\theta}) = [\mathbf{v}_0^T(\boldsymbol{\theta})]^*$.

C. Energy and other expectation values

The smallest eigenvalue $E_0(\boldsymbol{\theta})$ of the generalized eigenvalue problem in Eq. (6) corresponds to the minimum value of the Rayleigh quotient, i.e.,

$$E_0(\boldsymbol{\theta}) = \min_{\mathbf{v}(\boldsymbol{\theta})} \left\{ \frac{\langle \Psi_{\mathcal{U}}(\boldsymbol{\theta}) | \hat{\mathcal{H}} | \Psi_{\mathcal{U}}(\boldsymbol{\theta}) \rangle}{\langle \Psi_{\mathcal{U}}(\boldsymbol{\theta}) | \Psi_{\mathcal{U}}(\boldsymbol{\theta}) \rangle} \right\} = \mathbf{v}_0^\dagger(\boldsymbol{\theta}) \mathbf{H}(\boldsymbol{\theta}) \mathbf{v}_0(\boldsymbol{\theta}), \quad (11)$$

where the normalization condition for $|\Psi_{\mathcal{U}}^{(0)}(\boldsymbol{\theta})\rangle$ in Eq. (10) is used in the second equality. Therefore, the approximated ground-state energy of the Hamiltonian $\hat{\mathcal{H}}$ is obtained by minimizing $E_0(\boldsymbol{\theta})$ with respect to the variational parameters $\boldsymbol{\theta}$,

$$\begin{aligned} E_0(\boldsymbol{\theta}_{\text{opt}}) &= \min_{\boldsymbol{\theta}} \{E_0(\boldsymbol{\theta})\} = \min_{\boldsymbol{\theta}} \left\{ \frac{\langle \Psi_{\mathcal{U}}^{(0)}(\boldsymbol{\theta}) | \hat{\mathcal{H}} | \Psi_{\mathcal{U}}^{(0)}(\boldsymbol{\theta}) \rangle}{\langle \Psi_{\mathcal{U}}^{(0)}(\boldsymbol{\theta}) | \Psi_{\mathcal{U}}^{(0)}(\boldsymbol{\theta}) \rangle} \right\} \\ &= \min_{\boldsymbol{\theta}} \left\{ \min_{\mathbf{v}(\boldsymbol{\theta})} \left\{ \frac{\langle \Psi_{\mathcal{U}}(\boldsymbol{\theta}) | \hat{\mathcal{H}} | \Psi_{\mathcal{U}}(\boldsymbol{\theta}) \rangle}{\langle \Psi_{\mathcal{U}}(\boldsymbol{\theta}) | \Psi_{\mathcal{U}}(\boldsymbol{\theta}) \rangle} \right\} \right\}, \quad (12) \end{aligned}$$

and the optimized variational parameters $\boldsymbol{\theta}_{\text{opt}}$ give us the approximated ground state $|\Psi_{\mathcal{U}}^{(0)}(\boldsymbol{\theta}_{\text{opt}})\rangle$. Once a set of optimal variational parameters $\boldsymbol{\theta}_{\text{opt}}$ is obtained, the ground-state expectation value of an observable \hat{A} can be approximated as

$$\langle \Psi_0 | \hat{A} | \Psi_0 \rangle \approx \langle \Psi_{\mathcal{U}}^{(0)}(\boldsymbol{\theta}_{\text{opt}}) | \hat{A} | \Psi_{\mathcal{U}}^{(0)}(\boldsymbol{\theta}_{\text{opt}}) \rangle = \mathbf{v}_0^\dagger(\boldsymbol{\theta}_{\text{opt}}) \mathbf{A}(\boldsymbol{\theta}_{\text{opt}}) \mathbf{v}_0(\boldsymbol{\theta}_{\text{opt}}), \quad (13)$$

where $[\mathbf{A}(\boldsymbol{\theta})]_{ij} = \langle u_i(\boldsymbol{\theta}) | \hat{A} | u_j(\boldsymbol{\theta}) \rangle = \langle \psi(\boldsymbol{\theta}) | \hat{\mathcal{O}}_i^\dagger \hat{A} \hat{\mathcal{O}}_j | \psi(\boldsymbol{\theta}) \rangle$ and the normalization condition for $|\Psi_{\mathcal{U}}^{(0)}(\boldsymbol{\theta}_{\text{opt}})\rangle$ in Eq. (10) is assumed.

III. PARAMETER-OPTIMIZATION METHOD

A. Natural-gradient-descent method

The NGD method optimizes $\boldsymbol{\theta}$ by minimizing $E_0(\boldsymbol{\theta})$ with the following iteration [54]:

$$\boldsymbol{\theta}^{(x+1)} = \boldsymbol{\theta}^{(x)} - \tau [\mathbf{G}(\boldsymbol{\theta}^{(x)})]^{-1} \nabla E_0(\boldsymbol{\theta}^{(x)}), \quad (14)$$

where $\boldsymbol{\theta}^{(x)} = \{\theta_k^{(x)}\}_{k=1}^{N_{\mathcal{V}}}$ are the variational parameters at the x th iteration and $\tau > 0$ is a parameter called learning rate. $\mathbf{G}(\boldsymbol{\theta})$ is the Fubini-Study metric tensor [55–57] defined below and $[\nabla E_0(\boldsymbol{\theta})]_k = \partial E_0(\boldsymbol{\theta}) / \partial \theta_k$ is the energy gradient with respect to the variational parameter θ_k . The gradient descent (GD) method can be obtained by setting $\mathbf{G} = \mathbf{I}$ in Eq. (14). The initial variational parameters $\boldsymbol{\theta}^{(1)}$ can be set arbitrary. In the following, we shall derive explicit forms of the energy gradient and the Fubini-Study metric tensor for a QSE-based approach.

From Eqs. (6) and (10) and the Hermiticity of $\mathbf{H}(\boldsymbol{\theta})$ and $\mathbf{S}(\boldsymbol{\theta})$, the energy derivative is given by

$$\frac{\partial E_0(\boldsymbol{\theta})}{\partial \theta_k} = \mathbf{v}_0^\dagger(\boldsymbol{\theta}) \left(\frac{\partial \mathbf{H}(\boldsymbol{\theta})}{\partial \theta_k} - E_0(\boldsymbol{\theta}) \frac{\partial \mathbf{S}(\boldsymbol{\theta})}{\partial \theta_k} \right) \mathbf{v}_0(\boldsymbol{\theta}). \quad (15)$$

Equation (15) can be considered as a variant of the Hellmann-Feynman theorem for a generalized eigenvalue problem in the sense that the energy derivative does not require the derivative of the eigenvector $\mathbf{v}_0(\boldsymbol{\theta})$. The difference from the Hellmann-Feynman theorem for a standard eigenvalue problem is that Eq. (15) involves the derivative of the overlap matrix $\mathbf{S}(\boldsymbol{\theta})$.

The Fubini-Study metric tensor $\mathbf{G}(\boldsymbol{\theta})$ is given by

$$[\mathbf{G}(\boldsymbol{\theta})]_{kl} = \text{Re} \left[\gamma_{kl}(\boldsymbol{\theta}) - \beta_k^*(\boldsymbol{\theta}) \beta_l(\boldsymbol{\theta}) \right], \quad (16)$$

where

$$\gamma_{kl}(\boldsymbol{\theta}) = \langle \partial_k \Psi_{\mathcal{U}}^{(0)}(\boldsymbol{\theta}) | \partial_l \Psi_{\mathcal{U}}^{(0)}(\boldsymbol{\theta}) \rangle \quad (17)$$

and

$$\beta_k(\boldsymbol{\theta}) = \langle \Psi_{\mathcal{U}}^{(0)}(\boldsymbol{\theta}) | \partial_k \Psi_{\mathcal{U}}^{(0)}(\boldsymbol{\theta}) \rangle \quad (18)$$

with $\partial_k \equiv \partial / \partial \theta_k$ (see Appendix A for details). Note that our definition of β_k in Eq. (18) differs from that in Ref. [55] by a multiplicative factor $-i$. The derivative of the normalization condition $\partial_k \langle \Psi_{\mathcal{U}}^{(0)}(\boldsymbol{\theta}) | \Psi_{\mathcal{U}}^{(0)}(\boldsymbol{\theta}) \rangle = 0$ implies that $\beta_k(\boldsymbol{\theta})$ is pure imaginary and hence $\mathbf{G}(\boldsymbol{\theta})$ is a real symmetric matrix. By substituting

$$|\partial_k \Psi_{\mathcal{U}}^{(0)}(\boldsymbol{\theta})\rangle = \sum_i \partial_k v_{i,0}(\boldsymbol{\theta}) |u_i(\boldsymbol{\theta})\rangle + \sum_i v_{i,0}(\boldsymbol{\theta}) |\partial_k u_i(\boldsymbol{\theta})\rangle \quad (19)$$

into Eqs. (17) and (18), we obtain that

$$\begin{aligned} \gamma_{kl}(\boldsymbol{\theta}) &= \sum_{ij} (\partial_k v_{i,0}^*) (\partial_l v_{j,0}) \langle u_i | u_j \rangle + \sum_{ij} v_{i,0}^* v_{j,0} \langle \partial_k u_i | \partial_l u_j \rangle \\ &+ \sum_{ij} (\partial_k v_{i,0}^*) v_{j,0} \langle u_i | \partial_l u_j \rangle + \sum_{ij} v_{i,0}^* (\partial_l v_{j,0}) \langle \partial_k u_i | u_j \rangle \\ &= (\partial_k \mathbf{v}_0)^\dagger \mathbf{S}(\partial_l \mathbf{v}_0) + \mathbf{v}_0^\dagger \mathbf{S}_{(k,l)} \mathbf{v}_0 \\ &+ (\partial_k \mathbf{v}_0)^\dagger \mathbf{S}_{(,l)} \mathbf{v}_0 + \mathbf{v}_0^\dagger [\mathbf{S}_{(,k)}]^\dagger (\partial_l \mathbf{v}_0) \quad (20) \end{aligned}$$

and

$$\begin{aligned}\beta_k(\boldsymbol{\theta}) &= \sum_{ij} v_{i,0}^* (\partial_k v_{j,0}) \langle u_i | u_j \rangle + \sum_{ij} v_{i,0}^* v_{j,0} \langle u_i | \partial_k u_j \rangle \\ &= \mathbf{v}_0^\dagger \mathbf{S}(\partial_k \mathbf{v}_0) + \mathbf{v}_0^\dagger \mathbf{S}_{(k)} \mathbf{v}_0,\end{aligned}\quad (21)$$

where $[\mathbf{S}_{(k)}(\boldsymbol{\theta})]_{ij} \equiv \langle u_i(\boldsymbol{\theta}) | \partial_k u_j(\boldsymbol{\theta}) \rangle$ and $[\mathbf{S}_{(k,l)}(\boldsymbol{\theta})]_{ij} \equiv \langle \partial_k u_i(\boldsymbol{\theta}) | \partial_l u_j(\boldsymbol{\theta}) \rangle$. Note that the $\boldsymbol{\theta}$ dependence of $|u_i\rangle$, \mathbf{v}_0 , and \mathbf{S} is implicitly assumed in the right-hand sides of Eqs. (20) and (21). We should also note that $[\mathbf{S}_{(k,l)}(\boldsymbol{\theta})]^\dagger = \mathbf{S}_{(l,k)}(\boldsymbol{\theta})$ and hence not all matrices $\mathbf{S}_{(k,l)}(\boldsymbol{\theta})$ are independent.

To obtain the derivative of the eigenvector $\mathbf{v}_0(\boldsymbol{\theta})$ with respect to the variational parameters $\boldsymbol{\theta}$, let us first expand it in the subspace \mathcal{U} as

$$\frac{\partial \mathbf{v}_0(\boldsymbol{\theta})}{\partial \theta_k} = \sum_{n=0}^{d_{\mathcal{U}}-1} c_{k,n} \mathbf{v}_n(\boldsymbol{\theta}), \quad (22)$$

where \mathbf{v}_n is the n th eigenvector satisfying $\mathbf{H}(\boldsymbol{\theta}) \mathbf{v}_n(\boldsymbol{\theta}) = E_n(\boldsymbol{\theta}) \mathbf{S}(\boldsymbol{\theta}) \mathbf{v}_n(\boldsymbol{\theta})$ with $\mathbf{v}_m^\dagger(\boldsymbol{\theta}) \mathbf{S}(\boldsymbol{\theta}) \mathbf{v}_n(\boldsymbol{\theta}) = \delta_{mn}$ for $0 \leq m, n \leq d_{\mathcal{U}} - 1$, and $\{c_{k,n}\}_{n=0}^{d_{\mathcal{U}}-1}$ are complex numbers to be determined. By taking the derivative of $\mathbf{H}(\boldsymbol{\theta}) \mathbf{v}_n(\boldsymbol{\theta}) = E_n(\boldsymbol{\theta}) \mathbf{S}(\boldsymbol{\theta}) \mathbf{v}_n(\boldsymbol{\theta})$, multiplying $\mathbf{v}_m^\dagger(\boldsymbol{\theta})$ from the left on it, and using $\mathbf{v}_m^\dagger(\boldsymbol{\theta}) \mathbf{S}(\boldsymbol{\theta}) \mathbf{v}_n(\boldsymbol{\theta}) = \delta_{mn}$ for $n \neq 0$, we find that $c_{k,n} = \frac{\mathbf{v}_n^\dagger(\partial_k \mathbf{H} - E_0 \partial_k \mathbf{S}) \mathbf{v}_0}{E_0 - E_n} \mathbf{v}_n$ for $n \neq 0$ and hence

$$\frac{\partial \mathbf{v}_0(\boldsymbol{\theta})}{\partial \theta_k} = c_{k,0} \mathbf{v}_0(\boldsymbol{\theta}) + \sum_{n \neq 0}^{d_{\mathcal{U}}-1} \frac{\mathbf{v}_n^\dagger(\boldsymbol{\theta}) \left(\frac{\partial \mathbf{H}(\boldsymbol{\theta})}{\partial \theta_k} - E_0(\boldsymbol{\theta}) \frac{\partial \mathbf{S}(\boldsymbol{\theta})}{\partial \theta_k} \right) \mathbf{v}_0(\boldsymbol{\theta})}{E_0(\boldsymbol{\theta}) - E_n(\boldsymbol{\theta})} \mathbf{v}_n(\boldsymbol{\theta}), \quad (23)$$

where $E_0(\boldsymbol{\theta}) \neq E_n(\boldsymbol{\theta})$ is assumed. For the remaining coefficient $c_{k,0}$, the derivative of the normalization condition $\partial_k \langle \Psi_{\mathcal{U}}^{(0)}(\boldsymbol{\theta}) | \Psi_{\mathcal{U}}^{(0)}(\boldsymbol{\theta}) \rangle = \partial_k (\mathbf{v}_0^\dagger(\boldsymbol{\theta}) \mathbf{S}(\boldsymbol{\theta}) \mathbf{v}_0(\boldsymbol{\theta})) = 0$ implies that

$$\text{Re} c_{k,0} = -\frac{1}{2} \mathbf{v}_0^\dagger(\boldsymbol{\theta}) \frac{\partial \mathbf{S}(\boldsymbol{\theta})}{\partial \theta_k} \mathbf{v}_0(\boldsymbol{\theta}), \quad (24)$$

$$\text{Im} c_{k,0}: \text{undetermined}. \quad (25)$$

As we shall discuss below, the coefficient $c_{k,0}$ can be chosen arbitrarily as far as the Fubini-Study metric tensor $\mathbf{G}(\boldsymbol{\theta})$ is concerned. For numerical simulations in Sec. VII, we set that $\text{Im} c_{k,0} = 0$.

Here are two remarks regarding the coefficient $c_{k,0}$. First, $\text{Re} c_{k,0}$ in Eq. (24) ensures that $\beta_k(\boldsymbol{\theta})$ is pure imaginary [see the discussion below Eq. (18)], which follows from Eq. (21) because one can easily show that $\mathbf{v}_0^\dagger \mathbf{S}(\partial_k \mathbf{v}_0) = c_{k,0}$ and $\text{Re} \left[\mathbf{v}_0^\dagger \mathbf{S}_{(k)} \mathbf{v}_0 \right] = \frac{1}{2} \mathbf{v}_0^\dagger (\partial_k \mathbf{S}) \mathbf{v}_0$. This is a natural generalization of the corresponding result for real symmetric $\mathbf{H}(\boldsymbol{\theta})$ and $\mathbf{S}(\boldsymbol{\theta})$ in a real inner product space reported in Ref. [58] to a Hermitian case in a complex inner product space. Second, the Fubini-Study metric tensor $\mathbf{G}(\boldsymbol{\theta})$ is independent of $c_{k,0}$. To prove this statement, let us consider a shift of the coefficient $c_{k,0} \mapsto c_{k,0} + \Delta c_{k,0}$, i.e.,

$$\frac{\partial \mathbf{v}_0(\boldsymbol{\theta})}{\partial \theta_k} \mapsto \frac{\partial \mathbf{v}_0(\boldsymbol{\theta})}{\partial \theta_k} + \Delta c_{k,0} \mathbf{v}_0(\boldsymbol{\theta}). \quad (26)$$

Then, $\gamma_{kl}(\boldsymbol{\theta})$ and $\beta_k^*(\boldsymbol{\theta}) \beta_l(\boldsymbol{\theta})$ are transformed accordingly as

$$\gamma_{kl}(\boldsymbol{\theta}) \mapsto \gamma_{kl}(\boldsymbol{\theta}) + \Delta c_{k,0}^* \Delta c_{l,0} + \Delta c_{k,0}^* \beta_l(\boldsymbol{\theta}) + \Delta c_{l,0} \beta_k^*(\boldsymbol{\theta}) \quad (27)$$

and

$$\begin{aligned}\beta_k^*(\boldsymbol{\theta}) \beta_l(\boldsymbol{\theta}) &\mapsto (\beta_k^*(\boldsymbol{\theta}) + \Delta c_{k,0}^*) (\beta_l(\boldsymbol{\theta}) + \Delta c_{l,0}) \\ &= \beta_k^*(\boldsymbol{\theta}) \beta_l(\boldsymbol{\theta}) + \Delta c_{k,0}^* \Delta c_{l,0} + \Delta c_{k,0}^* \beta_l(\boldsymbol{\theta}) + \Delta c_{l,0} \beta_k^*(\boldsymbol{\theta}).\end{aligned}\quad (28)$$

Therefore, the Fubini-Study metric tensor $\mathbf{G}(\boldsymbol{\theta})$ is invariant under the shift in Eq. (26), i.e.,

$$\mathbf{G}(\boldsymbol{\theta}) \mapsto \mathbf{G}(\boldsymbol{\theta}). \quad (29)$$

Notice that the transformations in Eqs. (27) and (28) are similar to those considered in Ref. [55], where the Fubini-Study metric tensor $\mathbf{G}(\boldsymbol{\theta})$ is constructed so as to be invariant under multiplication of a global phase factor to the state $|\Psi_{\mathcal{U}}^{(0)}(\boldsymbol{\theta})\rangle$. Indeed, the former transformations are exactly the same as the latter ones if $\Delta c_{k,0}$ and $\Delta c_{l,0}$ in Eqs. (27) and (28) are pure imaginary. This also implies that the undetermined and in principle arbitrarily chosen $\text{Im} c_{k,0}$ in Eq. (25) can be absorbed into the global phase factor of the state $|\Psi_{\mathcal{U}}^{(0)}(\boldsymbol{\theta})\rangle$, which is analogous to the case of the first-order perturbation theory for a standard (i.e., not a generalized) Hermitian eigenvalue problem in quantum mechanics, where the imaginary part of the coefficient corresponding to $c_{k,0}$ is also undetermined [59]. Since $\partial_k \mathbf{v}_0(\boldsymbol{\theta})$ appears only in the Fubini-Study metric tensor $\mathbf{G}(\boldsymbol{\theta})$ in the present study, $\Delta c_{k,0}$ and hence $c_{k,0}$ can be chosen arbitrarily.

B. Derivatives

We now derive analytical expressions of the derivatives, assuming that $|\psi(\boldsymbol{\theta})\rangle$ in Eq. (2) has a particular form of

$$|\psi(\boldsymbol{\theta})\rangle \equiv \prod_{k=N_v}^1 \hat{U}_k(\theta_k) \hat{W} |0\rangle^{\otimes N}, \quad (30)$$

where $\hat{U}_k(\theta_k)$ is a unitary operator parametrized by θ_k and \hat{W} is a unitary operator independent of the variational parameters. Since $\{\hat{U}_k(\theta_k)\}_{k=1}^{N_v}$ and \hat{W} are unitary, $|\psi(\boldsymbol{\theta})\rangle$ can be prepared efficiently on a quantum computer. Moreover, we assume that $\hat{U}_k(\theta_k)$ in Eq. (30) is an exponential of an involutory operator \hat{P}_k of the form

$$\hat{U}_k(\theta_k) = e^{-i\hat{P}_k \theta_k / 2} = \hat{1} \cos \frac{\theta_k}{2} - i\hat{P}_k \sin \frac{\theta_k}{2}, \quad (31)$$

where $\hat{1}$ is the identity operator and the second equality is because of $\hat{P}_k^2 = \hat{1}$.

According to the parameter-shift rules [60–62], the derivatives appearing in Eqs. (15) and (23) can be evaluated as

$$\frac{\partial \mathbf{H}(\boldsymbol{\theta})}{\partial \theta_k} = \frac{1}{2} \left[\mathbf{H}(\boldsymbol{\theta} + \frac{\pi}{2} \mathbf{e}_k) - \mathbf{H}(\boldsymbol{\theta} - \frac{\pi}{2} \mathbf{e}_k) \right] \quad (32)$$

and

$$\frac{\partial \mathbf{S}(\boldsymbol{\theta})}{\partial \theta_k} = \frac{1}{2} \left[\mathbf{S}(\boldsymbol{\theta} + \frac{\pi}{2} \mathbf{e}_k) - \mathbf{S}(\boldsymbol{\theta} - \frac{\pi}{2} \mathbf{e}_k) \right], \quad (33)$$

where $[\mathbf{e}_k]_{k'} = \delta_{kk'}$ is the N_v -dimensional basis vector. Note that the derivative of the parametrized state $|u_i(\boldsymbol{\theta})\rangle$ in Eq. (2) itself is also evaluated simply as

$$|\partial_k u_i(\boldsymbol{\theta})\rangle = \frac{1}{2} |u_i(\boldsymbol{\theta} + \pi \mathbf{e}_k)\rangle. \quad (34)$$

Instead of Eqs. (32) and (33), the derivatives of $\mathbf{H}(\boldsymbol{\theta})$ and $\mathbf{S}(\boldsymbol{\theta})$ can also be written as

$$\frac{\partial \mathbf{H}(\boldsymbol{\theta})}{\partial \theta_k} = \mathbf{H}_{(,k)}(\boldsymbol{\theta}) + [\mathbf{H}_{(,k)}(\boldsymbol{\theta})]^\dagger \quad (35)$$

and

$$\frac{\partial \mathbf{S}(\boldsymbol{\theta})}{\partial \theta_k} = \mathbf{S}_{(,k)}(\boldsymbol{\theta}) + [\mathbf{S}_{(,k)}(\boldsymbol{\theta})]^\dagger, \quad (36)$$

where $[\mathbf{H}_{(,k)}(\boldsymbol{\theta})]_{ij} \equiv \langle u_i(\boldsymbol{\theta}) | \hat{\mathcal{H}} | \partial_k u_j(\boldsymbol{\theta}) \rangle$. By substituting Eq. (34) into Eqs. (35) and (36), different analytical expressions for the derivatives can be obtained. As far as numerical simulations are concerned, Eqs. (35) and (36) are more preferable than Eqs. (32) and (33). This is because the number of the parametrized states required for Eqs. (35) and (36) is $N_v + 1$, i.e., $|\psi(\boldsymbol{\theta})\rangle$ and $\{|\psi(\boldsymbol{\theta} + \pi \mathbf{e}_k)\rangle\}_{k=1}^{N_v}$, while Eqs. (32) and (33) require $2N_v$ states $\{|\psi(\boldsymbol{\theta} \pm \frac{\pi}{2} \mathbf{e}_k)\rangle\}_{k=1}^{N_v}$, and thus the numerical complexity is approximately half.

IV. KRYLOV-EXTENDED SYMMETRY-ADAPTED VQE

Equation (9) implies that the selection of the subspace \mathcal{U} is crucial for approximating the ground state (or any target eigenstate) of a Hamiltonian $\hat{\mathcal{H}}$. In the Krylov-subspace SAVQE for the ground state calculation, the subspace \mathcal{U} is constructed as

$$\begin{aligned} \mathcal{U} &= \mathcal{K}_{d_u}(\hat{\mathcal{H}}, \hat{\mathcal{P}}|\psi(\boldsymbol{\theta})\rangle) \\ &= \text{span}(\hat{\mathcal{P}}|\psi(\boldsymbol{\theta})\rangle, \hat{\mathcal{H}}\hat{\mathcal{P}}|\psi(\boldsymbol{\theta})\rangle, \dots, \hat{\mathcal{H}}^{d_u-1}\hat{\mathcal{P}}|\psi(\boldsymbol{\theta})\rangle), \end{aligned} \quad (37)$$

where $\hat{\mathcal{P}}$ is a symmetry-projection operator and by definition $\hat{\mathcal{H}}$ and $\hat{\mathcal{P}}$ commute to each other, i.e., $[\hat{\mathcal{H}}, \hat{\mathcal{P}}] = 0$. The explicit form of $\hat{\mathcal{P}}$ is determined by considering the Hamiltonian symmetry and the details are described in Sec. V D. $|\psi(\boldsymbol{\theta})\rangle$ is a quantum circuit ansatz parametrized by the variational parameters $\boldsymbol{\theta} = \{\theta_k\}_{k=1}^{N_v}$ as in Eq. (30) and generally breaks the symmetry of the Hamiltonian \mathcal{H} . With the projection operator $\hat{\mathcal{P}}$, the state $\hat{\mathcal{P}}|\psi(\boldsymbol{\theta})\rangle$ is projected onto the symmetry sector relevant to the ground state. It is obvious that the Krylov subspace in Eq. (37) is a special case of the more general subspace in Eq. (1) with the operator $\hat{\mathcal{O}}_n$ in Eq. (2) given now by

$$\hat{\mathcal{O}}_n = \hat{\mathcal{H}}^n \hat{\mathcal{P}}. \quad (38)$$

In the VQE scheme, each term in the matrix elements of $\mathbf{H}(\boldsymbol{\theta})$ and $\mathbf{S}(\boldsymbol{\theta})$ for a given set of the variational parameters $\boldsymbol{\theta}$ is evaluated on a quantum computer, while a classical computer is employed to solve the generalized eigenvalue problem in Eq. (6) and to optimize the variational parameters, here using

the NGD method described in Sec. III, for which each term in the matrix elements of the Fubini-Study tensor $\mathbf{G}(\boldsymbol{\theta})$ is also evaluated on a quantum computer. As explained in the next section, the nonunitary projection operator $\hat{\mathcal{P}}$ can be expressed by a linear combination of unitary operators and hence can be implemented on a quantum computer with the appropriate postprocessing [43].

To evaluate the expectation value of $\hat{\mathcal{H}}^n$ on a quantum computer, several direct [63–65] and approximate [66, 67] methods have been proposed recently. For a recent review, see for example Ref. [68]. Here, we employ the QPM, a scheme introduced in Ref. [42], where the Hamiltonian power $\hat{\mathcal{H}}^n$ is directly treated by approximating it with a linear combination of unitary time-evolution operators at $n + 1$ different times. Using the second-order symmetric Suzuki-Trotter (ST) decomposition [69, 70], the Hamiltonian power $\hat{\mathcal{H}}^n$ is approximated as [42]

$$\hat{\mathcal{H}}^n = \hat{\mathcal{H}}_{\text{ST}}^n(\Delta) + O(\Delta^2), \quad (39)$$

where

$$\hat{\mathcal{H}}_{\text{ST}}^n(\Delta) = \frac{i^n}{\Delta^n} \sum_{k=0}^n (-1)^k \binom{n}{k} [\hat{S}_2(\Delta/2)]^{n-2k}, \quad (40)$$

and Δ is a parameter and should be in general a small real number. $\hat{S}_2(\Delta/2)$ is the second-order symmetric ST decomposition of the time-evolution operator $e^{-i\hat{\mathcal{H}}\Delta/2}$ and $O(\Delta^2)$ in Eq. (39) is the leading systematic error. The explicit form of $\hat{S}_2(\Delta/2)$ depends on the Hamiltonian $\hat{\mathcal{H}}$ and it is given in Sec. VII B for the two-component Fermi-Hubbard model in a ladder lattice structure.

As described in detail in Ref. [42], the order of the leading systematic error can be eliminated systematically with the Richardson extrapolation. For instance, the first-order Richardson extrapolation $\hat{\mathcal{H}}_{\text{ST}(1)}^n(\Delta)$ of $\hat{\mathcal{H}}_{\text{ST}}^n(\Delta)$ can be given by

$$\hat{\mathcal{H}}_{\text{ST}(1)}^n(\Delta) = \frac{1}{3} [4\hat{\mathcal{H}}_{\text{ST}}^n(\Delta/2) - \hat{\mathcal{H}}_{\text{ST}}^n(\Delta)], \quad (41)$$

which approximates $\hat{\mathcal{H}}^n$ to $O(\Delta^4)$, i.e.,

$$\hat{\mathcal{H}}^n = \hat{\mathcal{H}}_{\text{ST}(1)}^n(\Delta) + O(\Delta^4). \quad (42)$$

By using Eq. (41), we can approximate $\hat{\mathcal{O}}_n$ in Eq. (38) as

$$\hat{\mathcal{O}}_n \approx \hat{\mathcal{H}}_{\text{ST}(1)}^n(\Delta) \hat{\mathcal{P}}. \quad (43)$$

Accordingly, the Hamiltonian matrix and the overlap matrix are given respectively as

$$[\mathbf{H}(\boldsymbol{\theta})]_{ij} \approx \langle \psi(\boldsymbol{\theta}) | \hat{\mathcal{P}} \hat{\mathcal{H}}_{\text{ST}(1)}^i(\Delta) \hat{\mathcal{H}} \hat{\mathcal{H}}_{\text{ST}(1)}^j(\Delta) \hat{\mathcal{P}} | \psi(\boldsymbol{\theta}) \rangle \quad (44)$$

and

$$[\mathbf{S}(\boldsymbol{\theta})]_{ij} \approx \langle \psi(\boldsymbol{\theta}) | \hat{\mathcal{P}} \hat{\mathcal{H}}_{\text{ST}(1)}^i(\Delta) \hat{\mathcal{H}}_{\text{ST}(1)}^j(\Delta) \hat{\mathcal{P}} | \psi(\boldsymbol{\theta}) \rangle, \quad (45)$$

where $\hat{\mathcal{P}}^\dagger = \hat{\mathcal{P}}$ and $[\hat{\mathcal{H}}_{\text{ST}(1)}^n]^\dagger = \hat{\mathcal{H}}_{\text{ST}(1)}^n$ are used. On the other hand, because of $[\hat{\mathcal{H}}, \hat{\mathcal{P}}] = 0$, we can also approximate $\hat{\mathcal{O}}_n$ in Eq. (38) as

$$\hat{\mathcal{O}}_n \approx \hat{\mathcal{P}} \hat{\mathcal{H}}_{\text{ST}(1)}^n(\Delta). \quad (46)$$

Correspondingly, the Hamiltonian matrix and the overlap matrix can be given respectively as

$$[\mathbf{H}(\boldsymbol{\theta})]_{ij} \approx \langle \psi(\boldsymbol{\theta}) | \hat{\mathcal{H}}_{\text{ST}(1)}^i(\Delta) \hat{\mathcal{H}} \hat{\mathcal{P}} \hat{\mathcal{H}}_{\text{ST}(1)}^j(\Delta) | \psi(\boldsymbol{\theta}) \rangle \quad (47)$$

and

$$[\mathbf{S}(\boldsymbol{\theta})]_{ij} \approx \langle \psi(\boldsymbol{\theta}) | \hat{\mathcal{H}}_{\text{ST}(1)}^i(\Delta) \hat{\mathcal{P}} \hat{\mathcal{H}}_{\text{ST}(1)}^j(\Delta) | \psi(\boldsymbol{\theta}) \rangle, \quad (48)$$

where $\hat{\mathcal{P}}^2 = \hat{\mathcal{P}}$ is also used. Although the apparent forms of $[\mathbf{H}(\boldsymbol{\theta})]_{ij}$ ($[\mathbf{S}(\boldsymbol{\theta})]_{ij}$) in Eqs. (44) and (47) [Eqs. (45) and (48)] are different, they are exactly the same up to $O(\Delta^4)$ because of $[\hat{\mathcal{P}}, \hat{\mathcal{H}}_{\text{ST}(1)}^n] = O(\Delta^4)$.

An important difference between Eqs. (44) and (45) and Eqs. (47) and (48) is that the latter formulas contain the projection operator $\hat{\mathcal{P}}$ only once for each matrix element. This is advantageous for quantum-classical hybrid computing because the number of measurements required for Eqs. (47) and (48) is smaller than that for Eqs. (44) and (45) by a factor of the number of terms in $\hat{\mathcal{P}}$, assuming that $\hat{\mathcal{P}}$ is given by a linear combination of unitary operators. For this reason, we adopt Eqs. (47) and (48) for numerical simulations in Sec. VII. It should be noted that, due to the presence of the projection operator $\hat{\mathcal{P}}$, the number of measurements required for evaluating the Hamiltonian and overlap matrices in Eqs. (47) and (48) is increased by a factor of the number of terms in $\hat{\mathcal{P}}$ from that discussed in Ref. [42].

After optimizing the variational parameters $\boldsymbol{\theta} = \{\theta_k\}_{k=1}^{N_v}$ in Eq. (12), we obtain the approximated ground state $|\Psi_{\mathcal{U}}^{(0)}(\boldsymbol{\theta}_{\text{opt}})\rangle$ in the Krylov subspace \mathcal{U} defined in Eq. (37), i.e.,

$$|\Psi_0\rangle \approx |\Psi_{\mathcal{U}}^{(0)}(\boldsymbol{\theta}_{\text{opt}})\rangle = \sum_{i=0}^{d_{\mathcal{U}}-1} v_{i,0}(\boldsymbol{\theta}_{\text{opt}}) \hat{\mathcal{P}} \hat{\mathcal{H}}_{\text{ST}(1)}^i(\Delta) | \psi(\boldsymbol{\theta}_{\text{opt}}) \rangle. \quad (49)$$

The expectation value of any quantity $\hat{\mathcal{O}}$ with respect to $|\Psi_{\mathcal{U}}^{(0)}(\boldsymbol{\theta}_{\text{opt}})\rangle$ is then evaluated simply as

$$\begin{aligned} \langle \Psi_0 | \hat{\mathcal{O}} | \Psi_0 \rangle &\approx \frac{\langle \Psi_{\mathcal{U}}^{(0)}(\boldsymbol{\theta}_{\text{opt}}) | \hat{\mathcal{O}} | \Psi_{\mathcal{U}}^{(0)}(\boldsymbol{\theta}_{\text{opt}}) \rangle}{\langle \Psi_{\mathcal{U}}^{(0)}(\boldsymbol{\theta}_{\text{opt}}) | \Psi_{\mathcal{U}}^{(0)}(\boldsymbol{\theta}_{\text{opt}}) \rangle} \\ &= \frac{\mathbf{v}_0^\dagger(\boldsymbol{\theta}_{\text{opt}}) \mathbf{O}(\boldsymbol{\theta}_{\text{opt}}) \mathbf{v}_0(\boldsymbol{\theta}_{\text{opt}})}{\mathbf{v}_0^\dagger(\boldsymbol{\theta}_{\text{opt}}) \mathbf{S}(\boldsymbol{\theta}_{\text{opt}}) \mathbf{v}_0(\boldsymbol{\theta}_{\text{opt}})}, \end{aligned} \quad (50)$$

where

$$[\mathbf{O}(\boldsymbol{\theta})]_{ij} = \langle \psi(\boldsymbol{\theta}) | \hat{\mathcal{H}}_{\text{ST}(1)}^i(\Delta) \hat{\mathcal{O}} \hat{\mathcal{P}} \hat{\mathcal{H}}_{\text{ST}(1)}^j(\Delta) | \psi(\boldsymbol{\theta}) \rangle \quad (51)$$

and $[\hat{\mathcal{O}}, \hat{\mathcal{P}}] = 0$ is assumed. This is easily generalized for a quantity $\hat{\mathcal{O}}$ with $[\hat{\mathcal{O}}, \hat{\mathcal{P}}] \neq 0$.

V. MODEL, SYMMETRY, AND PROJECTION OPERATOR

A. Fermi-Hubbard model

As a demonstration, we apply the extended SAVQE method to the two-component Fermi-Hubbard model. The Hamilto-

nian $\hat{\mathcal{H}}$ of the Fermi-Hubbard model is given by

$$\hat{\mathcal{H}} = -t \sum_{\langle i,j \rangle, \sigma} (\hat{c}_{i\sigma}^\dagger \hat{c}_{j\sigma} + \text{H.c.}) + U_H \sum_i \left(\hat{n}_{i\uparrow} - \frac{1}{2} \right) \left(\hat{n}_{i\downarrow} - \frac{1}{2} \right), \quad (52)$$

where $\hat{c}_{i\sigma}^\dagger$ ($\hat{c}_{i\sigma}$) is the creation (annihilation) operator of a fermion at site i ($= 1, 2, \dots, L$) with spin σ ($= \uparrow, \downarrow$) on a lattice having L sites, and $\hat{n}_{i\sigma} = \hat{c}_{i\sigma}^\dagger \hat{c}_{i\sigma}$ is the fermion density operator. t and U_H are the hopping and the on-site interaction parameters, respectively, and $\langle i, j \rangle$ runs over all nearest-neighbor pairs of sites i and j . We assume that $t > 0$ and $U_H > 0$.

We adopt the Jordan-Wigner transformation [71, 72] of the form

$$\hat{c}_{i\sigma}^\dagger \stackrel{\text{JWT}}{=} \frac{1}{2} (\hat{X}_{i\sigma} - i \hat{Y}_{i\sigma}) \prod_{k < i_\sigma} \hat{Z}_k \quad (53)$$

and

$$\hat{c}_{i\sigma} \stackrel{\text{JWT}}{=} \frac{1}{2} (\hat{X}_{i\sigma} + i \hat{Y}_{i\sigma}) \prod_{k < i_\sigma} \hat{Z}_k, \quad (54)$$

where “ $\stackrel{\text{JWT}}{=}$ ” implies that the Jordan-Wigner transformation transforms fermion operators on the left-hand side to a qubit representation on the right-hand side, and \hat{X}_{i_σ} , \hat{Y}_{i_σ} , and \hat{Z}_{i_σ} are the Pauli operators at qubit i_σ . We use the convention that the qubits are ordered as $i_\uparrow = i$ ($= 1, 2, \dots, L$) and $i_\downarrow = i + L$ ($= L + 1, L + 2, \dots, 2L$) with the total number of qubits being $N = 2L$ in Eqs. (53) and (54). The fermion density operator is given by

$$\hat{n}_{i\sigma} = \hat{c}_{i\sigma}^\dagger \hat{c}_{i\sigma} \stackrel{\text{JWT}}{=} \frac{1}{2} (1 - \hat{Z}_{i_\sigma}), \quad (55)$$

and thus it is plausible to say that the single-particle state (i, σ) is occupied (unoccupied) if the i_σ -th qubit state is $|1\rangle_{i_\sigma}$ ($|0\rangle_{i_\sigma}$) because $\hat{n}_{i\sigma}|1\rangle_{i_\sigma} = |1\rangle_{i_\sigma}$ ($\hat{n}_{i\sigma}|0\rangle_{i_\sigma} = |0\rangle_{i_\sigma}$), where $|1\rangle_{i_\sigma}$ and $|0\rangle_{i_\sigma}$ are the eigenstates of Pauli operator \hat{Z}_{i_σ} at qubit i_σ , i.e., $\hat{Z}_{i_\sigma}|0\rangle_{i_\sigma} = |0\rangle_{i_\sigma}$ and $\hat{Z}_{i_\sigma}|1\rangle_{i_\sigma} = -|1\rangle_{i_\sigma}$. The Fermi-Hubbard Hamiltonian in the qubit representation reads

$$\hat{\mathcal{H}} \stackrel{\text{JWT}}{=} -\frac{t}{2} \sum_{\sigma} \sum_{\langle i_\sigma, j_\sigma \rangle} (\hat{X}_{i_\sigma} \hat{X}_{j_\sigma} + \hat{Y}_{i_\sigma} \hat{Y}_{j_\sigma}) \hat{Z}_{\text{JW}, i_\sigma j_\sigma} + \frac{U_H}{4} \sum_{i=1}^L \hat{Z}_i \hat{Z}_{i+L}, \quad (56)$$

where $\hat{Z}_{\text{JW}, ij} = \prod_{i \leq k \leq j} \hat{Z}_k$ is the Jordan-Wigner string for $i \leq k \leq j$ and $\hat{Z}_{\text{JW}, ij} = \hat{1}$ for $i = j \pm 1$.

In this paper, we consider the Fermi-Hubbard model in a 4×2 lattice under open-boundary conditions (see Fig. 1) at half filling. Therefore, to represent the variational state, we use $N = 16$ qubits, where the first 8 qubits are assigned to the single-particle states labeled by site i and spin \uparrow , and the remaining 8 qubits are assigned to the single-particle states labeled by site i and spin \downarrow (also see Fig. 8).

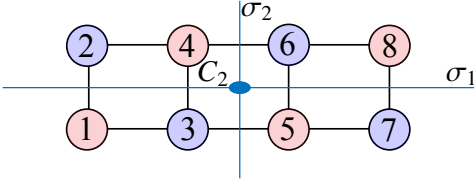


FIG. 1. Geometry of a 4×2 lattice in which the Fermi-Hubbard model is defined. Circles represent sites that are labeled by the numbers shown inside the circles. The hopping term is present only between the nearest-neighboring sites connected by black solid lines. The lattice sites belonging to A (B) sublattice are denoted with red (blue) circles. The two-fold rotational axis (C_2) and the mirror planes (σ_1, σ_2) for the C_{2v} symmetry are also indicated in the figure.

B. Hamiltonian symmetry

We now consider the Hamiltonian symmetry. From the particular geometry of the cluster shown in Fig. 1, it is obvious that the model has the C_{2v} point-group symmetry, i.e.,

$$[\hat{\mathcal{H}}, \hat{g}_m] = 0, \quad (57)$$

where \hat{g}_m is a group element of C_{2v} . We note that the 4×2 cluster itself possesses the D_{2h} point-group symmetry that has 8 symmetry operations (i.e., symmetry elements), and the C_{2v} group is a subgroup of the D_{2h} group. Indeed, the D_{2h} group can be seen as a direct-product group of the C_{2v} group and the C_i group, i.e., $D_{2h} = C_{2v} \times C_i$. However, in a pure two-dimensional space, the inversion and the two-fold rotation around the principal axis are equivalent. Therefore, among the 8 symmetry operations in the D_{2h} group, only the 4 symmetry operations, which are all the symmetry operations of the C_{2v} group, are independent. This is the reason why we consider the C_{2v} point-group symmetry here.

It can also be shown that the Fermi-Hubbard model considered here is spin symmetric, i.e.,

$$[\hat{\mathcal{H}}, \hat{S}^2] = 0, \quad [\hat{\mathcal{H}}, \hat{S}_z] = 0, \quad (58)$$

where $\hat{S}^2 = \hat{S}_x^2 + \hat{S}_y^2 + \hat{S}_z^2$, $\hat{S}_x = \sum_i \hat{S}_i^x$, $\hat{S}_y = \sum_i \hat{S}_i^y$, and $\hat{S}_z = \sum_i \hat{S}_i^z$ with

$$\hat{S}_i^x = \hat{\mathbf{c}}_i^\dagger \mathbf{s}_x \hat{\mathbf{c}}_i = \frac{1}{2} (\hat{c}_{i\uparrow}^\dagger \hat{c}_{i\downarrow} + \hat{c}_{i\downarrow}^\dagger \hat{c}_{i\uparrow}), \quad (59)$$

$$\hat{S}_i^y = \hat{\mathbf{c}}_i^\dagger \mathbf{s}_y \hat{\mathbf{c}}_i = \frac{1}{2i} (\hat{c}_{i\uparrow}^\dagger \hat{c}_{i\downarrow} - \hat{c}_{i\downarrow}^\dagger \hat{c}_{i\uparrow}), \quad (60)$$

$$\hat{S}_i^z = \hat{\mathbf{c}}_i^\dagger \mathbf{s}_z \hat{\mathbf{c}}_i = \frac{1}{2} (\hat{n}_{i\uparrow} - \hat{n}_{i\downarrow}). \quad (61)$$

Here, we have introduced that $\hat{\mathbf{c}}_i^\dagger = [\hat{c}_{i\uparrow}^\dagger \ \hat{c}_{i\downarrow}^\dagger]$ and

$$\mathbf{s}_x = \frac{1}{2} \begin{bmatrix} 0 & 1 \\ 1 & 0 \end{bmatrix}, \quad \mathbf{s}_y = \frac{1}{2} \begin{bmatrix} 0 & -i \\ i & 0 \end{bmatrix}, \quad \mathbf{s}_z = \frac{1}{2} \begin{bmatrix} 1 & 0 \\ 0 & -1 \end{bmatrix}. \quad (62)$$

Hereafter, we refer to Eq. (58) as the S symmetry.

Due to the bipartite structure of the hopping term (see Fig. 1), the Fermi-Hubbard model has another symmetry [73]

$$[\hat{\mathcal{H}}, \hat{\eta}^2] = 0, \quad [\hat{\mathcal{H}}, \hat{\eta}_z] = 0, \quad (63)$$

where $\hat{\eta}^2 = \hat{\eta}_x^2 + \hat{\eta}_y^2 + \hat{\eta}_z^2$, $\hat{\eta}_x = \sum_i \hat{\eta}_i^x$, $\hat{\eta}_y = \sum_i \hat{\eta}_i^y$, and $\hat{\eta}_z = \sum_i \hat{\eta}_i^z$ with

$$\hat{\eta}_i^x = \hat{\mathbf{b}}_i^\dagger \mathbf{s}_x \hat{\mathbf{b}}_i = \frac{e^{i\phi_i}}{2} (\hat{c}_{i\uparrow}^\dagger \hat{c}_{i\downarrow}^\dagger + \hat{c}_{i\downarrow} \hat{c}_{i\uparrow}), \quad (64)$$

$$\hat{\eta}_i^y = \hat{\mathbf{b}}_i^\dagger \mathbf{s}_y \hat{\mathbf{b}}_i = \frac{e^{i\phi_i}}{2i} (\hat{c}_{i\uparrow}^\dagger \hat{c}_{i\downarrow}^\dagger - \hat{c}_{i\downarrow} \hat{c}_{i\uparrow}), \quad (65)$$

$$\hat{\eta}_i^z = \hat{\mathbf{b}}_i^\dagger \mathbf{s}_z \hat{\mathbf{b}}_i = \frac{1}{2} (\hat{n}_{i\uparrow} + \hat{n}_{i\downarrow} - 1). \quad (66)$$

Here, we have introduced that $\hat{\mathbf{b}}_i^\dagger = [\hat{c}_{i\uparrow}^\dagger \ e^{i\phi_i} \hat{c}_{i\downarrow}^\dagger]$ and

$$e^{i\phi_i} = e^{-i\phi_i} = \begin{cases} +1 & \text{for } i \in A \text{ sublattice} \\ -1 & \text{for } i \in B \text{ sublattice} \end{cases} \quad (67)$$

with A and B sublattices being indicated in Fig. 1. Hereafter, we refer to Eq. (63) as the η symmetry. Note that, as in the case of the spin operators \hat{S}_i^α with $\alpha = x, y, z$, the η operators $\hat{\eta}_i^\alpha$ in Eqs. (64)-(66) satisfy the commutation relations of the angular momentum. It is also important to note that $[\hat{S}_i^\alpha, \hat{\eta}_i^\beta] = 0$ with $\alpha, \beta = x, y, z$. Therefore, any eigenstate of $\hat{\mathcal{H}}$ can be simultaneously an eigenstate of \hat{S}^2 , \hat{S}_z , $\hat{\eta}^2$, and $\hat{\eta}_z$, and thus it is characterized with these eigenvalues.

C. Spin- and η -singlet ground state

Via the particle-hole transformation for spin-down fermions

$$\hat{c}_{i\downarrow} \mapsto e^{-i\phi_i} \hat{c}_{i\downarrow}^\dagger \quad (68)$$

with spin-up fermions unaltered, the spin and the η operators are transformed into each other because $\hat{\mathbf{c}}_i^\dagger \mapsto \hat{\mathbf{b}}_i^\dagger$ and $\hat{\mathbf{b}}_i^\dagger \mapsto \hat{\mathbf{c}}_i^\dagger$, assuming that $e^{i\phi_i}$ is given in Eq. (67). As stated above, this observation also implies that the η operators satisfy the same commutation relations as the spin operators. Note that a unitary operator $\hat{U}_i^{\text{ph}} = \hat{c}_{i\downarrow} + e^{-i\phi_i} \hat{c}_{i\downarrow}^\dagger$ [74] satisfies the relation $(\hat{U}_i^{\text{ph}})^\dagger \hat{c}_{i\downarrow} \hat{U}_i^{\text{ph}} = e^{-i\phi_i} \hat{c}_{i\downarrow}^\dagger$, which corresponds to the mapping in Eq. (68).

With the same particle-hole transformation, the repulsive Fermi-Hubbard model on a bipartite lattice maps to the attractive Fermi-Hubbard model on the same lattice [75]. The particle-hole transformation is useful to gain insight into the correspondence between the repulsive and attractive Fermi-Hubbard models as well as that between the spin and charge degrees of freedom (see for example Refs. [76–79]). Indeed, the fact [80] that the ground state of the attractive Fermi-Hubbard model for even number of fermions in the absence of magnetic field has $S = 0$ (i.e., spin singlet) implies that the ground state of the repulsive Fermi-Hubbard model on a bipartite lattice at half filling has $\eta = 0$ (i.e., η singlet). Furthermore, the ground state of the repulsive Fermi-Hubbard model on a bipartite lattice at half filling is proved to have $S = \frac{1}{2} \||B| - |A|\|$, where $|B|$ ($|A|$) is the number of sites in the B (A) sublattice [80]. Since $|B| = |A|$ in the present case, the ground state has $S = 0$.

D. Projection operators

To take into account the spatial, S , and η symmetry, we adopt the projection operator $\hat{\mathcal{P}}$ of the form

$$\hat{\mathcal{P}} = \hat{\mathcal{P}}^{(\eta)} \hat{\mathcal{P}}^{(S)} \hat{\mathcal{P}}^{(\alpha)}, \quad (69)$$

where $\hat{\mathcal{P}}^{(\alpha)}$, $\hat{\mathcal{P}}^{(S)}$, and $\hat{\mathcal{P}}^{(\eta)}$ are the projection operators of the spatial, S , and η symmetry, respectively. In this section, we specify the form of these projection operators. Note that these three projection operators commute with each other.

1. Spatial symmetry

The projection operator of the spatial symmetry for an irreducible representation α of group \mathcal{G} is given by [81]

$$\hat{\mathcal{P}}_{\mu\nu}^{(\alpha)} = \frac{d_\alpha}{|\mathcal{G}|} \sum_{\hat{g}_m \in \mathcal{G}} [D_{\mu\nu}^{(\alpha)}(\hat{g}_m)]^* \hat{g}_m, \quad (70)$$

where $|\mathcal{G}|$ is the number of group elements in \mathcal{G} (i.e., order of group \mathcal{G}), d_α is the dimension of the irreducible representation α , $D_{\mu\nu}^{(\alpha)}(\hat{g}_m)$ is the (μ, ν) entry of the representation matrix in the irreducible representation α for the symmetry operation \hat{g}_m , and the sum runs over all the group elements. The character of the representation matrix $D_{\mu\nu}^{(\alpha)}(\hat{g}_m)$ is defined by $\chi^{(\alpha)}(\hat{g}_m) = \sum_{\mu=1}^{d_\alpha} D_{\mu\mu}^{(\alpha)}(\hat{g}_m)$. Note that $D_{\mu\nu}^{(\alpha)}$ satisfies the orthogonality relation

$$\sum_{\hat{g}_m \in \mathcal{G}} [D_{\mu\nu}^{(\alpha)}(\hat{g}_m)]^* D_{\mu'\nu'}^{(\alpha')}(\hat{g}_m) = \frac{|\mathcal{G}|}{d_\alpha} \delta_{\alpha\alpha'} \delta_{\mu\mu'} \delta_{\nu\nu'}. \quad (71)$$

$\hat{\mathcal{P}}_{\mu\nu}^{(\alpha)}$ extracts a basis state $|\alpha\mu\rangle$ from $|\alpha\nu\rangle$, i.e., $\hat{\mathcal{P}}_{\mu\nu}^{(\alpha)}|\alpha\nu\rangle = |\alpha\mu\rangle$, where $|\alpha\nu\rangle$ is a state such that $\hat{g}_m|\alpha\nu\rangle = \sum_{\mu} D_{\mu\nu}^{(\alpha)}(\hat{g}_m)|\alpha\mu\rangle$. Strictly speaking, $\hat{\mathcal{P}}_{\mu\nu}^{(\alpha)}$ is a projection operator only when $\mu = \nu$ because $\hat{\mathcal{P}}_{\mu\nu}^{(\alpha)} \hat{\mathcal{P}}_{\nu'\mu'}^{(\alpha')} = \delta_{\alpha\alpha'} \delta_{\nu\nu'} \hat{\mathcal{P}}_{\mu\mu'}^{(\alpha)}$, but here we loosely use the term ‘‘projection operator’’ for $\hat{\mathcal{P}}_{\mu\nu}^{(\alpha)}$.

For the point group C_{2v} , $|\mathcal{G}| = 4$, $d_\alpha = 1$, and $\{\hat{g}_m\}_{m=1}^{|\mathcal{G}|} = \{\hat{I}, \hat{C}_2, \hat{\sigma}_1, \hat{\sigma}_2\}$, where \hat{C}_2 is the π rotation about the center of the 4×2 cluster, and σ_1 and σ_2 are reflections with respect to the corresponding planes (see Fig. 1). Omitting the subscript $\mu\nu$ in Eq. (70) because of $d_\alpha = 1$, we have

$$\hat{\mathcal{P}}^{(\alpha)} = \frac{1}{4} \sum_{m=1}^4 [\chi^{(\alpha)}(\hat{g}_m)]^* \hat{g}_m. \quad (72)$$

The ground state of the Fermi-Hubbard model studied here belongs to the irreducible representation $\alpha = A_1$, in which $\chi^{(\alpha)}(\hat{g}_m) = 1$ for all \hat{g}_m .

2. S and η symmetry

Since both S and η operators satisfy the same commutation relations of the angular momentum, we denote by J either S or

η for convenience. According to the theory of rotation group, the projection operator of the J symmetry ($J = S, \eta$) is given by [82–85]

$$\hat{\mathcal{P}}_{MK}^{(J)} = \frac{2J+1}{\Omega} \int d\omega [D_{MK}^{(J)}(\omega)]^* \hat{R}(\omega), \quad (73)$$

where

$$\hat{R}(\omega) = e^{-i\alpha\hat{J}_z} e^{-i\beta\hat{J}_y} e^{-i\gamma\hat{J}_z} \quad (74)$$

is the rotation operator with $\omega = (\alpha, \beta, \gamma)$, i.e., the parameters of rotation group (Euler angles) specifying the group element, and

$$\Omega = \int d\omega = \int_0^{2\pi} d\alpha \int_0^\pi d\beta \sin\beta \int_0^{2\pi} d\gamma = 8\pi^2 \quad (75)$$

defines the volume of the parameter ω space.

$D_{MK}^{(J)}(\omega)$ in Eq. (73) is the Wigner’s D function defined by

$$D_{MK}^{(J)}(\omega) = \langle JM | \hat{R}(\omega) | JK \rangle = e^{-i\alpha M} d_{MK}^{(J)}(\beta) e^{-i\gamma K} \quad (76)$$

with $|JM\rangle$ being an eigenstate of \hat{J}^2 and \hat{J}_z such that $\hat{J}^2|JM\rangle = J(J+1)|JM\rangle$ and $\hat{J}_z|JM\rangle = M|JM\rangle$, and

$$d_{MK}^{(J)}(\beta) = \langle JM | e^{-i\beta\hat{J}_y} | JK \rangle \quad (77)$$

is the Wigner’s small d function that is real [86–88]. Note that the Wigner’s D function $D_{MK}^{(J)}(\omega)$ satisfies the orthogonality relation

$$\int d\omega [D_{MK}^{(J)}(\omega)]^* D_{M'K'}^{(J')}(\omega) = \frac{\Omega}{2J+1} \delta_{JJ'} \delta_{MM'} \delta_{KK'}. \quad (78)$$

Therefore, $\hat{\mathcal{P}}_{MK}^{(J)}$ extracts a basis state $|JM\rangle$ from $|JK\rangle$, i.e., $\hat{\mathcal{P}}_{MK}^{(J)}|JK\rangle = |JM\rangle$ because $\hat{R}(\omega)|JK\rangle = \sum_M D_{MK}^{(J)}(\omega)|JM\rangle$. In Eqs. (75) and (78), J is assumed to be integer. For a half integer J , the range of either α or γ integration should be $[0, 4\pi]$ and hence $\Omega = 16\pi^2$ [81, 85, 88]. Details on $D_{MK}^{(J)}(\omega)$ and $d_{MK}^{(J)}(\beta)$ can be found, for example, in Ref. [88].

Since our target state is the ground state of the Fermi-Hubbard model in the sector of $\eta_z = 0$ (i.e., half filling) and $S_z = 0$ (i.e., zero magnetization), we can set $M = 0$ in Eq. (73) for both $J = \eta$ and S . In addition, the variational state $|\psi(\theta)\rangle$, whose concrete form is described in Sec. VII A, is constructed to satisfy $\hat{J}_z|\psi(\theta)\rangle = 0$, implying that we can set $K = 0$ in Eq. (73) for $J = \eta$ and S . For $K = M = 0$, the Wigner’s D function is given by

$$D_{00}^J(\omega) = d_{00}^J(\beta) = P_J(\cos\beta), \quad (79)$$

where P_J is the J th order Legendre polynomial. By integrating out γ , the state $\hat{\mathcal{P}}^{(J)}|\psi(\theta)\rangle \equiv \hat{\mathcal{P}}_{00}^{(J)}|\psi(\theta)\rangle$ is given by [89]

$$\begin{aligned} \hat{\mathcal{P}}^{(J)}|\psi(\theta)\rangle &= \frac{2J+1}{4\pi} \int_0^{2\pi} d\alpha \int_0^\pi d\beta \sin\beta P_J(\cos\beta) \\ &\times e^{-i\alpha\hat{J}_z} e^{-i\beta\hat{J}_y} |\psi(\theta)\rangle. \end{aligned} \quad (80)$$

Furthermore, when a matrix element $\langle \psi' | \hat{\mathcal{P}}^{(J)} | \psi(\theta) \rangle$ with $\hat{J}_z | \psi' \rangle = 0$ is considered, one can also integrate out α as [89]

$$\begin{aligned} \langle \psi' | \hat{\mathcal{P}}^{(J)} | \psi(\theta) \rangle &= \frac{2J+1}{2} \int_0^\pi d\beta \sin\beta P_J(\cos\beta) \\ &\times \langle \psi' | e^{-i\beta \hat{J}_y} | \psi(\theta) \rangle. \end{aligned} \quad (81)$$

Examples of $|\psi'\rangle$ particularly relevant for the present study include $|\psi(\theta)\rangle$, $\hat{\mathcal{H}}|\psi(\theta)\rangle$, and $\hat{J}^2|\psi(\theta)\rangle$. Moreover, Eqs. (80) and (81) still hold even when $|\psi(\theta)\rangle$ in these equations is replaced with $\hat{\mathcal{H}}_{\text{ST}(1)}^n |\psi(\theta)\rangle$ because $\hat{J}_z \hat{\mathcal{H}}_{\text{ST}(1)}^n |\psi(\theta)\rangle = 0$ for the ST decomposition employed (see Sec. VII B).

E. Projection operator as a linear combination of unitaries

Since the rotation group is a continuous group, $\hat{\mathcal{P}}^{(J)}$ involves integration over continuous variables, i.e., Euler angles, as in Eqs. (80) and (81). However, for numerical simulations as well as quantum-classical hybrid calculations, a proper discretization of the integration is necessary. The integration over α and β in Eq. (80) can be discretized with the trapezoidal rule and the Gauss-Legendre quadrature, respectively. By omitting irrelevant normalization factor, $\hat{\mathcal{P}}^{(J)}|\psi(\theta)\rangle$ is now approximated as

$$\begin{aligned} &\hat{\mathcal{P}}^{(J)}|\psi(\theta)\rangle \\ &\approx \frac{2J+1}{2N_{J,\text{azimuth}}} \sum_{i=1}^{N_{J,\text{azimuth}}} \sum_{j=1}^{N_{J,\text{polar}}} w_{j,J} P_J(\cos\beta_{j,J}) e^{-i\alpha_{i,J} \hat{J}_z} e^{-i\beta_{j,J} \hat{J}_y} |\psi(\theta)\rangle, \end{aligned} \quad (82)$$

where $\{\alpha_{i,J}\}_{i=1}^{N_{J,\text{azimuth}}}$ are $N_{J,\text{azimuth}}$ azimuth angles equally spaced in $[0, 2\pi]$, $\{\beta_{j,J}\}_{j=1}^{N_{J,\text{polar}}}$ are polar angles such that $P_{N_{J,\text{polar}}}(\cos\beta_{j,J}) = 0$, and $\{w_{j,J}\}_{j=1}^{N_{J,\text{polar}}}$ are the corresponding integration weight of the Gauss-Legendre quadrature.

The full symmetry-projected state is now given approximately as

$$\begin{aligned} &\hat{\mathcal{P}}^{(\eta)} \hat{\mathcal{P}}^{(S)} \hat{\mathcal{P}}^{(\alpha)} |\psi(\theta)\rangle \\ &\approx \frac{2\eta+1}{2N_{\eta,\text{azimuth}}} \frac{2S+1}{2N_{S,\text{azimuth}}} \frac{d_\alpha}{|\mathcal{G}|} \sum_{i=1}^{N_{\eta,\text{azimuth}}} \sum_{j=1}^{N_{\eta,\text{polar}}} \sum_{k=1}^{N_{S,\text{azimuth}}} \sum_{l=1}^{N_{S,\text{polar}}} \sum_{m=1}^{|\mathcal{G}|} \\ &\times w_{j,\eta} w_{l,S} P_\eta(\cos\beta_{j,\eta}) P_S(\cos\beta_{l,S}) \left[\chi^{(\alpha)}(\hat{g}_m) \right]^* \\ &\times e^{-i\alpha_{i,\eta} \hat{J}_z} e^{-i\beta_{j,\eta} \hat{J}_y} e^{-i\alpha_{k,S} \hat{J}_z} e^{-i\beta_{l,S} \hat{J}_y} \hat{g}_m |\psi(\theta)\rangle. \end{aligned} \quad (83)$$

Note that the operators in the last line are unitary and thus the symmetry-projected state is evaluated by applying a linear combination of unitary operators to the state. The symmetry-projected state given in Eq. (83) is in general not normalized even though the state $|\psi(\theta)\rangle$ is normalized. However, this is not a problem because the normalization of states spanning the Krylov subspace \mathcal{U} is not required (see Sec II and Sec IV) but the normalization of the approximated ground state is guaranteed by Eq. (10).

A matrix element similar to that in Eq. (81) but for the full projection operators can be evaluated simply by setting

$N_{J,\text{azimuth}} = 1$ and $e^{-i\alpha_{i,J} \hat{J}_z} = \hat{I}$ in Eq. (83) and taking the overlap with $\langle \psi' |$, i.e.,

$$\begin{aligned} &\langle \psi' | \hat{\mathcal{P}}^{(\eta)} \hat{\mathcal{P}}^{(S)} \hat{\mathcal{P}}^{(\alpha)} | \psi(\theta) \rangle \\ &\approx \frac{2\eta+1}{2} \frac{2S+1}{2} \frac{d_\alpha}{|\mathcal{G}|} \sum_{j=1}^{N_{\eta,\text{polar}}} \sum_{l=1}^{N_{S,\text{polar}}} \sum_{m=1}^{|\mathcal{G}|} \\ &\times w_{j,\eta} w_{l,S} P_\eta(\cos\beta_{j,\eta}) P_S(\cos\beta_{l,S}) \left[\chi^{(\alpha)}(\hat{g}_m) \right]^* \\ &\times \langle \psi' | e^{-i\beta_{j,\eta} \hat{J}_y} e^{-i\beta_{l,S} \hat{J}_y} \hat{g}_m | \psi(\theta) \rangle. \end{aligned} \quad (84)$$

Concerning quantum-classical hybrid calculations, Eq. (84) implies that the matrix element on the left-hand side can be estimated by evaluating the matrix elements $\left\{ \left\{ \left\{ \langle \psi' | e^{-i\beta_{j,\eta} \hat{J}_y} e^{-i\beta_{l,S} \hat{J}_y} \hat{g}_m | \psi(\theta) \rangle \right\}_{m=1}^{|\mathcal{G}|} \right\}_{l=1}^{N_{S,\text{polar}}} \right\}_{j=1}^{N_{\eta,\text{polar}}}$ with $N_{\eta,\text{polar}} N_{S,\text{polar}} |\mathcal{G}|$ different circuit structures using quantum computers, and then adding all of them with the proper weights on classical computers. We should recall that $d_\alpha = 1$ and $|\mathcal{G}| = 4$ for the C_{2v} point group, $P_\eta(\cos\beta_{j,\eta}) = 1$ for $\eta = 0$, $P_S(\cos\beta_{l,S}) = 1$ for $S = 0$, and $\chi^{(\alpha)}(\hat{g}_m) = 1$ for $\alpha = A_1$.

While Eq. (84) suffices for our purpose, we briefly discuss how many of the integration points $N_{J,\text{polar}}$ and $N_{J,\text{azimuth}}$ in Eq. (83) are required for the variational state $|\psi(\theta)\rangle$ that will be described in Sec. VII A. We find numerically that typically $N_{S,\text{polar}} = 2$ and $N_{S,\text{azimuth}} = 4$ ($N_{\eta,\text{polar}} = 3$ and $N_{\eta,\text{azimuth}} = 5$) are enough to ensure that the calculated value of S (η) with respect to the state $\hat{\mathcal{P}}|\psi(\theta)\rangle$ can be regarded as integer within the double-precision arithmetic. We also find that typically the lowest-order Lebedev quadrature $\hat{\mathcal{P}}^{(J)} \approx \sum_{i=1}^6 e^{-i\alpha_{i,J} \hat{J}_z} e^{-i\beta_{i,J} \hat{J}_y}$, which uses six integration points $(\alpha_{i,J}, \beta_{i,J}) = (0, 0), (0, \pi/2), (\pi/2, \pi/2), (\pi, \pi/2), (3\pi/2, \pi/2),$ and $(0, \pi)$ with equal integration weights, is adequate at least for the S -symmetry projection. On the other hand, when we use Eq. (84), where $N_{J,\text{azimuth}} = 1$ by construction, we find that typically $N_{S,\text{polar}} = 2$ ($N_{\eta,\text{polar}} = 3$) is sufficient to evaluate S (η) within the double-precision arithmetic. However, to ensure that the symmetry projection is made essentially exactly, we set $N_{J,\text{polar}} = 4$ for both $J = S$ and η projections in our numerical simulations.

VI. SYMMETRY OPERATION ON QUANTUM CIRCUIT

In this section, we describe how the spatial symmetry operators \hat{g}_m and the rotation operators $e^{-i\alpha \hat{J}_y}$ and $e^{-i\beta \hat{J}_z}$ with $J = S, \eta$ for fermions can be implemented on a quantum circuit, assuming the qubit representation of fermion operators by the Jordan-Wigner transformation in Eqs. (53) and (54).

A. Quantum circuit for spatial symmetry operations

Let \hat{g}_m be a spatial-symmetry operation that transfers the local state at the i th qubit to the $m(i)$ th qubit. Such operation

can be represented as a permutation

$$\sigma_m \equiv \underbrace{\begin{pmatrix} N & N-1 & \cdots & 2 & 1 \\ m(N) & m(N-1) & \cdots & m(2) & m(1) \end{pmatrix}}_{N \text{ columns}} \quad (85)$$

where N is the number of qubits. We first briefly review an implementation of the spatial-symmetry operations for spins, and then proceed to the spatial-symmetry operations for fermions.

1. Spatial symmetry operations for spins

For a system composed of spins, each having spin 1/2, the spatial-symmetry operator \hat{g}_m can be expressed as a product of nearest-neighbor SWAP operators $\hat{S}_{i\delta(i)}$

$$\hat{g}_m = \prod_{\sigma_m} \hat{S}_{i\delta(i)}, \quad (86)$$

because any permutation can be expressed as a product of transpositions (i.e., nearest-neighbor SWAP operations). Here, $\delta(i) (= i \pm 1)$ denotes a neighboring qubit of qubit i , and the product \prod_{σ_m} should contain sequences of the SWAP operators of the form $\hat{S}_{\delta(\dots\delta(\delta(k))),m(k)} \cdots \hat{S}_{\delta(k),\delta(\delta(k))} \hat{S}_{k,\delta(k)}$ for every k . Such a product in Eq. (86) can be constructed accordingly to the ‘‘Amida lottery’’ construction [43], as shown in Fig. 2(a) for the case of

$$\sigma_m = \begin{pmatrix} 6 & 5 & 4 & 3 & 2 & 1 \\ 4 & 3 & 2 & 1 & 6 & 5 \end{pmatrix} \quad (87)$$

with $|b_6 b_5 b_4 b_3 b_2 b_1\rangle = |b_6\rangle_6 |b_5\rangle_5 |b_4\rangle_4 |b_3\rangle_3 |b_2\rangle_2 |b_1\rangle_1$ being transferred to $|b_2 b_1 b_6 b_5 b_4 b_3\rangle = |b_2\rangle_6 |b_1\rangle_5 |b_6\rangle_4 |b_5\rangle_3 |b_4\rangle_2 |b_3\rangle_1$, where $|b\rangle_i$ is the local state b ($= 0$ or 1) at the i th qubit.

We note that SWAP operator \hat{S}_{ij} acts on qubits i and j as

$$\hat{S}_{ij}|0\rangle_i|0\rangle_j = |0\rangle_i|0\rangle_j, \quad (88)$$

$$\hat{S}_{ij}|0\rangle_i|1\rangle_j = |1\rangle_i|0\rangle_j, \quad (89)$$

$$\hat{S}_{ij}|1\rangle_i|0\rangle_j = |0\rangle_i|1\rangle_j, \quad (90)$$

$$\hat{S}_{ij}|1\rangle_i|1\rangle_j = |1\rangle_i|1\rangle_j. \quad (91)$$

The matrix representation of \hat{S}_{ij} in these four basis states $|0\rangle_i|0\rangle_j$, $|0\rangle_i|1\rangle_j$, $|1\rangle_i|0\rangle_j$, and $|1\rangle_i|1\rangle_j$ is thus given by

$$\hat{S}_{ij} \doteq \begin{bmatrix} 1 & 0 & 0 & 0 \\ 0 & 0 & 1 & 0 \\ 0 & 1 & 0 & 0 \\ 0 & 0 & 0 & 1 \end{bmatrix}, \quad (92)$$

where \doteq implies that the operator on the left-hand side can be represented in the matrix form on the right-hand side with the basis states given above.

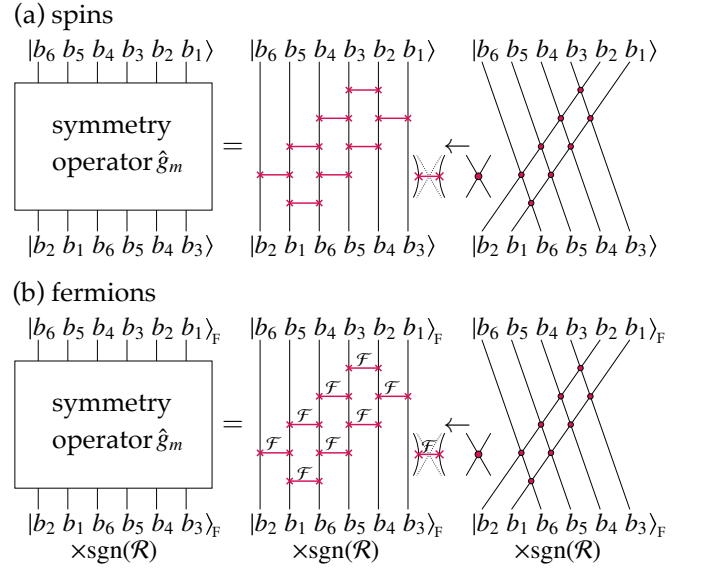


FIG. 2. Amida-lottery construction of a symmetry operator \hat{g}_m on a quantum circuit for (a) spin models in the computational basis [43] and (b) fermion models in an occupation basis [see Eq. (94)]. The figure refers to the case of $N = 6$ qubits. The vertical lines represent qubits and $\text{sgn}(\mathcal{R})$ in (b) denotes an appropriate sign factor for fermions [see Eq. (95) and also Eq. (B7)]. In the middle panel of (a), swap gates $\hat{S}_{i\delta(i)}$ are highlighted with thick red lines. In (b), a fermionic-swap gate $\hat{\mathcal{F}}_{i\delta(i)}$ is represented by a two-qubit gate with symbol \mathcal{F} . Assuming that the circuit evolves from top to bottom, the middle panels in (a) and (b) show that the symmetry operation \hat{g}_m in this example can be expressed as $\hat{g}_m = \hat{S}_{45}\hat{S}_{56}\hat{S}_{34}\hat{S}_{45}\hat{S}_{23}\hat{S}_{34}\hat{S}_{12}\hat{S}_{23}$ for spin models and $\hat{g}_m = \hat{\mathcal{F}}_{45}\hat{\mathcal{F}}_{56}\hat{\mathcal{F}}_{34}\hat{\mathcal{F}}_{45}\hat{\mathcal{F}}_{23}\hat{\mathcal{F}}_{34}\hat{\mathcal{F}}_{12}\hat{\mathcal{F}}_{23}$ for fermion models, respectively.

2. Spatial symmetry operations for fermions

For a system composed of fermions, \hat{g}_m has to take into account the anticommutation relations of fermion operators, in addition to the permutation of local states. This implies that symmetry operators can no longer be given as a product of the SWAP operators for fermions in general. As it is explained in Appendix B, the symmetry operation for fermions can be implemented simply by replacing the SWAP operators $\hat{S}_{i\delta(i)}$ in Eq. (86) with the fermionic-SWAP operators $\hat{\mathcal{F}}_{i\delta(i)}$:

$$\hat{g}_m = \prod_{\sigma_m} \hat{\mathcal{F}}_{i\delta(i)}. \quad (93)$$

Here, $\hat{\mathcal{F}}_{i\delta(i)}$ transforms a fermion creation operator \hat{c}_i^\dagger in such a way that $\hat{\mathcal{F}}_{i\delta(i)}\hat{c}_i^\dagger\hat{\mathcal{F}}_{i\delta(i)}^{-1} = \hat{c}_{\delta(i)}^\dagger$, implying that $\hat{g}_m\hat{c}_i^\dagger\hat{g}_m^{-1} = \hat{c}_{m(i)}^\dagger$. Note that the subscript i ($= 1, 2, \dots, N$) here labels all the single-particle local states including sites and spins.

Before discussing quantum circuits for fermionic symmetry operations, let us first explain how a state of the form

$$\begin{aligned} |b_N b_{N-1} \cdots b_1\rangle_F &\equiv \prod_{i=N}^1 (\hat{c}_i^\dagger)^{b_i} |0\rangle_F \\ &= (\hat{c}_N^\dagger)^{b_N} (\hat{c}_{N-1}^\dagger)^{b_{N-1}} \cdots (\hat{c}_1^\dagger)^{b_1} |0\rangle_F \end{aligned} \quad (94)$$

is transformed by \hat{g}_m , where $b_i = 0$ or 1 with $(\hat{c}_i^\dagger)^0 \equiv \hat{1}$ and $|0\rangle_F$ denotes the fermion vacuum such that $\hat{c}_i|0\rangle_F = 0$ for any i . We call a state of the form in Eq. (94) an occupation-basis state. Notice that here we have adopted the convention for the order of the single-particle local states i ($= 1, 2, \dots, N$) such that the smaller i resides on the further right, indicating the product $\prod_{i=N}^1$, although any convention for the order can be used. Then, the occupation-basis state is transformed by \hat{g}_m as

$$\begin{aligned} & \hat{g}_m |b_N b_{N-1} \dots b_1\rangle_F \\ &= \hat{g}_m \prod_{i=N}^1 (\hat{c}_i^\dagger)^{b_i} |0\rangle_F \\ &= \prod_{i=N}^1 (\hat{c}_{m(i)}^\dagger)^{b_i} |0\rangle_F \\ &= \prod_{m=N}^1 (\hat{c}_{m(i)}^\dagger)^{b_i} |0\rangle_F \times \text{sgn}(\mathcal{R}) \\ &= \prod_{i=N}^1 (\hat{c}_i^\dagger)^{b_{m^{-1}(i)}} |0\rangle_F \times \text{sgn}(\mathcal{R}) \\ &= |b_{m^{-1}(N)} b_{m^{-1}(N-1)} \dots b_{m^{-1}(1)}\rangle_F \times \text{sgn}(\mathcal{R}), \end{aligned} \quad (95)$$

where $\text{sgn}(\mathcal{R})$ denotes an appropriate sign factor due to the reordering of the fermion operators, and $m^{-1}(i)$ denotes the number obtained by applying the inverse permutation σ_m^{-1} to i . More details on fermionic symmetry operations are briefly reviewed in Appendix B. An example shown in Fig. 2(b) corresponds to a symmetry operation

$$\begin{aligned} & \hat{g}_m |b_6 b_5 b_4 b_3 b_2 b_1\rangle_F \\ &= \hat{g}_m (\hat{c}_6^\dagger)^{b_6} (\hat{c}_5^\dagger)^{b_5} (\hat{c}_4^\dagger)^{b_4} (\hat{c}_3^\dagger)^{b_3} (\hat{c}_2^\dagger)^{b_2} (\hat{c}_1^\dagger)^{b_1} |0\rangle_F \\ &= (\hat{c}_4^\dagger)^{b_6} (\hat{c}_3^\dagger)^{b_5} (\hat{c}_2^\dagger)^{b_4} (\hat{c}_1^\dagger)^{b_3} (\hat{c}_6^\dagger)^{b_2} (\hat{c}_5^\dagger)^{b_1} |0\rangle_F \\ &= (\hat{c}_6^\dagger)^{b_2} (\hat{c}_5^\dagger)^{b_1} (\hat{c}_4^\dagger)^{b_6} (\hat{c}_3^\dagger)^{b_5} (\hat{c}_2^\dagger)^{b_4} (\hat{c}_1^\dagger)^{b_3} |0\rangle_F \times \text{sgn}(\mathcal{R}) \\ &= |b_2 b_1 b_6 b_5 b_4 b_3\rangle_F \times \text{sgn}(\mathcal{R}) \end{aligned} \quad (96)$$

with the permutation σ_m given in Eq. (87). We should note that the $\text{sgn}(\mathcal{R})$ is not the parity of the permutation σ_m but depends on how fermions occupy the single-particle local states.

Let us now discuss quantum circuits for fermionic symmetry operations. Following the convention of the Jordan-Wigner transformation in Eqs. (53) and (54), here we assume the correspondence that the i th fermionic single-particle state is occupied (unoccupied) if the state of the i th qubit is $|1\rangle_i$ ($|0\rangle_i$). The fermion vacuum in the occupation basis can then be represented in the computational basis as

$$|0\rangle_F \stackrel{\text{JWT}}{=} |0\rangle_N |0\rangle_{N-1} \dots |0\rangle_1. \quad (97)$$

Note however that, in general, the occupation-basis state $|b_N b_{N-1} \dots b_1\rangle_F$ under the Jordan-Wigner transformation is not identical to the computational basis state $|b_N b_{N-1} \dots b_1\rangle = |b_N\rangle_N |b_{N-1}\rangle_{N-1} \dots |b_1\rangle_1$, i.e.,

$$|b_N b_{N-1} \dots b_1\rangle_F \stackrel{\text{JWT}}{\neq} |b_N b_{N-1} \dots b_1\rangle \quad (98)$$

because of the sign factor due to the anticommutation relation of fermions, e.g., $|11\rangle_F = \hat{c}_2^\dagger \hat{c}_1^\dagger |0\rangle_F \stackrel{\text{JWT}}{=} -|1\rangle_2 |1\rangle_1 = -|11\rangle$. The sign factor due to the anticommutation relations of fermions on a quantum state can be tracked by using the fermionic-SWAP operator [90–95] on a quantum circuit, which does not depend on the convention adopted for the occupation-basis state. The explicit form of the fermionic-SWAP operator in terms of the fermion operators is given in Appendix B.

The nearest-neighbor fermionic-SWAP operator $\hat{\mathcal{F}}_{i\delta(i)}$ acting on neighboring qubits i and $\delta(i)$ in the computational basis is defined as

$$\hat{\mathcal{F}}_{i\delta(i)} |0\rangle_i |0\rangle_{\delta(i)} = |0\rangle_i |0\rangle_{\delta(i)}, \quad (99)$$

$$\hat{\mathcal{F}}_{i\delta(i)} |0\rangle_i |1\rangle_{\delta(i)} = |1\rangle_i |0\rangle_{\delta(i)}, \quad (100)$$

$$\hat{\mathcal{F}}_{i\delta(i)} |1\rangle_i |0\rangle_{\delta(i)} = |0\rangle_i |1\rangle_{\delta(i)}, \quad (101)$$

$$\hat{\mathcal{F}}_{i\delta(i)} |1\rangle_i |1\rangle_{\delta(i)} = -|1\rangle_i |1\rangle_{\delta(i)}. \quad (102)$$

The matrix representation of $\hat{\mathcal{F}}_{i\delta(i)}$ in the above four basis states is thus given by

$$\hat{\mathcal{F}}_{i\delta(i)} \doteq \begin{bmatrix} 1 & 0 & 0 & 0 \\ 0 & 0 & 1 & 0 \\ 0 & 1 & 0 & 0 \\ 0 & 0 & 0 & -1 \end{bmatrix}. \quad (103)$$

Since the controlled-Z (CZ) operator acting on qubits i and j is represented as

$$\widehat{\text{CZ}}_{ij} \doteq \begin{bmatrix} 1 & 0 & 0 & 0 \\ 0 & 1 & 0 & 0 \\ 0 & 0 & 1 & 0 \\ 0 & 0 & 0 & -1 \end{bmatrix}, \quad (104)$$

the nearest-neighbor fermionic-SWAP operator can be written as [also see Fig. 3(a)]

$$\hat{\mathcal{F}}_{i\delta(i)} \stackrel{\text{JWT}}{=} \hat{S}_{i\delta(i)} \widehat{\text{CZ}}_{i\delta(i)} = \widehat{\text{CZ}}_{i\delta(i)} \hat{S}_{i\delta(i)}. \quad (105)$$

The decomposition of the fermionic-SWAP operator as in Eq. (105) is valid only when the qubits are nearest neighbors, i.e., $\delta(i) = i \pm 1$. As shown in Fig. 3(b), the long-range fermionic-SWAP operator $\hat{\mathcal{F}}_{ij}$ for $j \neq \delta(i)$ is inherently nonlocal and can be implemented as a product of nearest-neighbor fermionic-SWAP operators [also see Fig. 2(b)]. Furthermore, using the identities shown in Fig. 3(b), $\hat{\mathcal{F}}_{ij}$ can be expressed by $\hat{S}_{ij} \widehat{\text{CZ}}_{ij}$ sandwiched between two sequences of $|i-j|-1$ CZ gates. The example shown in Fig. 3(b) can be written as

$$\hat{\mathcal{F}}_{ij} \stackrel{\text{JWT}}{=} \left[\prod_{i \leq k \leq j} \widehat{\text{CZ}}_{jk} \right] \hat{f}_{ij} \left[\prod_{i \leq k \leq j} \widehat{\text{CZ}}_{jk} \right], \quad (106)$$

where

$$\hat{f}_{ij} \equiv \hat{S}_{ij} \widehat{\text{CZ}}_{ij} = \widehat{\text{CZ}}_{ij} \hat{S}_{ij} \doteq \begin{bmatrix} 1 & 0 & 0 & 0 \\ 0 & 0 & 1 & 0 \\ 0 & 1 & 0 & 0 \\ 0 & 0 & 0 & -1 \end{bmatrix}. \quad (107)$$

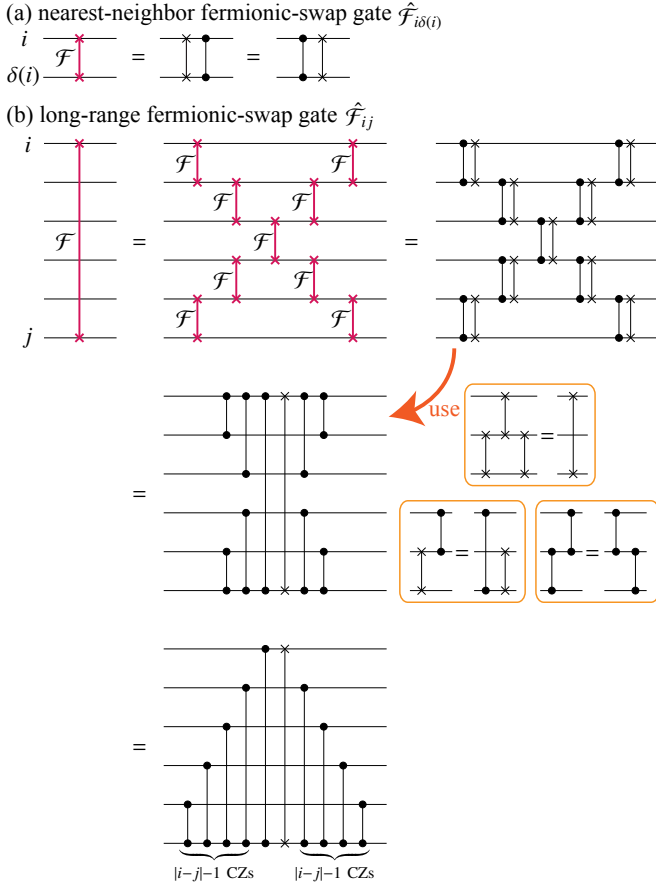


FIG. 3. Fermionic-swap gate acting on a pair of (a) nearest-neighbor qubits i and $\delta(i) = i \pm 1$ and (b) distant qubits i and j (the figure refers to the case of $|i - j| = 5$) is decomposed into a product of the swap and CZ gates. In (b), the third and fourth equalities follow from the gate identities shown in the boxes.

Note that this matrix is exactly the same as that in Eq. (103), but now qubits i and j are not necessarily nearest neighbors.

Let us now consider how one can implement a unitary operator of the form $\exp[-i\hat{q}_{ij}]^{\text{JWT}} \exp[-i\hat{h}_{ij}\hat{Z}_{\text{JW},ij}]$ in a quantum circuit, where $\hat{q}_{ij} \stackrel{\text{JWT}}{\equiv} \hat{h}_{ij}\hat{Z}_{\text{JW},ij}$ is Hermitian and quadratic in terms of fermion operators, satisfying that $\hat{\mathcal{F}}_{kj}\hat{q}_{ij}\hat{\mathcal{F}}_{kj} = \hat{q}_{ik}$, and \hat{h}_{ij} is a Hermitian operator in the qubit representation acting on qubits i and j , i.e., $[\hat{h}_{ij}, \hat{Z}_{\text{JW},ij}] = 0$. Examples of \hat{q}_{ij} include $\hat{q}_{ij} = \theta(\hat{c}_i^\dagger \hat{c}_j + \text{H.c.})$ and $\hat{q}_{ij} = i\theta(\hat{c}_i^\dagger \hat{c}_j^\dagger - \text{H.c.})$ with real θ . First, the equalities $\hat{\mathcal{F}}_{kj} \exp[-i\hat{q}_{ij}] \hat{\mathcal{F}}_{kj} = \exp[-i\hat{q}_{ik}] \stackrel{\text{JWT}}{=} \exp[-i\hat{h}_{ik}\hat{Z}_{\text{JW},ik}]$ and $\hat{Z}_{\text{JW},i\delta(i)} = \hat{I}$ imply that, by using two long-range fermionic-swap gates $\hat{\mathcal{F}}_{\delta(i)j}$, where qubit $\delta(i)$ is located between qubits i and j , we can remove the Jordan-Wigner string $\hat{Z}_{\text{JW},ij}$ from the exponent (first equality in Fig. 4):

$$\exp[-i\hat{h}_{ij}\hat{Z}_{\text{JW},ij}] = \hat{\mathcal{F}}_{\delta(i)j} \exp[-i\hat{h}_{i\delta(i)}] \hat{\mathcal{F}}_{\delta(i)j}. \quad (108)$$

Then, by representing the long-range fermionic-swap gates $\hat{\mathcal{F}}_{\delta(i)j}$ as a product of the CZ and the swap gates (second equal-

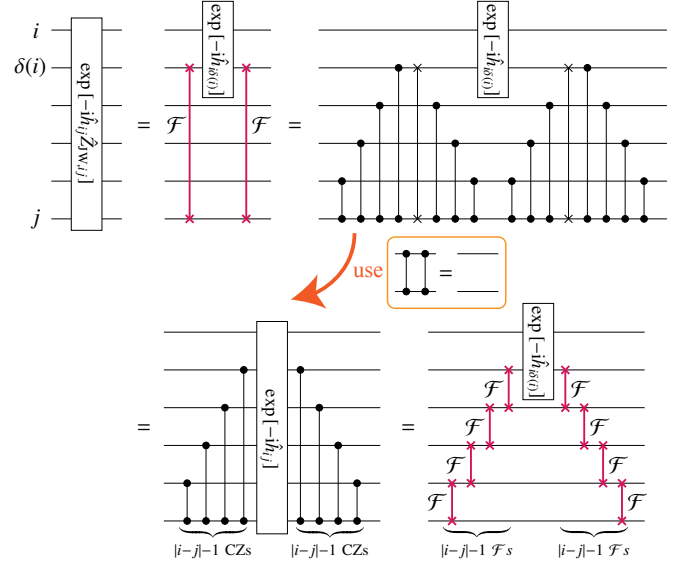


FIG. 4. Implementation of the $(|i - j| + 1)$ -qubit unitary gate $\exp[-i\hat{h}_{ij}\hat{Z}_{\text{JW},ij}]$ (top left) by a product of two-qubit unitary gates (bottom). The figure refers to the case of $|i - j| = 5$. The second equality follows from the decomposition of the long-range fermionic-swap gate shown in Fig. 3(b), and the third equality follows from the identity $\widehat{\text{CZ}}_{kl}^2 = \hat{I}$. The last equality makes use of the decomposition of the long-range fermionic-swap gate into a product of the nearest-neighbor fermionic-swap gates [for a variant of this decomposition, see the first equality in Fig. 3(b)].

ity in Fig. 4) and using the identity $\widehat{\text{CZ}}_{kl}^2 = \hat{I}$, we can cancel the redundant $\widehat{\text{CZ}}_{kl}$ gates and obtain (third equality in Fig. 4)

$$\exp[-i\hat{h}_{ij}\hat{Z}_{\text{JW},ij}] = \left[\prod_{i \leq k \leq j} \widehat{\text{CZ}}_{jk} \right] \exp[-i\hat{h}_{ij}] \left[\prod_{i \leq k \leq j} \widehat{\text{CZ}}_{jk} \right]. \quad (109)$$

A similar strategy for eliminating the redundancy in consecutive Jordan-Wigner strings has been reported in Ref. [96].

Two remarks are in order. First, by substituting $\hat{h}_{ij} \propto \hat{X}_i \hat{X}_j + \hat{Y}_i \hat{Y}_j$ in Eq. (109), we can reproduce the quantum circuit for the exponentiated hopping term of fermions reported previously in Ref. [97], i.e., an exchange-type gate [98] sandwiched between two sequences of $|i - j| - 1$ CNOT gates. Second, the $(|i - j| + 1)$ -qubit unitary gate $\exp[-i\hat{h}_{ij}\hat{Z}_{\text{JW},ij}]$ can also be implemented by a product of neighboring two-qubit gates at a cost of additional $2(|i - j| - 1)$ fermionic-swap gates (last equality in Fig. 4). For example, assuming that $i < \delta(i) = i + 1 < j$, $\exp[-i\hat{h}_{ij}\hat{Z}_{\text{JW},ij}]$ can also be implemented as

$$\exp[-i\hat{h}_{ij}\hat{Z}_{\text{JW},ij}] = \left[\prod_{k=\delta(i)+1}^j \hat{\mathcal{F}}_{k,k-1} \right] \exp[-i\hat{h}_{i\delta(i)}] \left[\prod_{k=j}^{\delta(i)+1} \hat{\mathcal{F}}_{k,k-1} \right]. \quad (110)$$

The resulting quantum circuit first moves the local state at the j th qubit to the qubit next to qubit i by applying the nearest-neighbor fermionic-SWAP gates successively, thus keeping track of the antisymmetric nature of fermion exchange, then it applies the gate $\exp[-i\hat{h}_{i\delta(i)}]$ on qubits i and $\delta(i)$, and finally it moves the local state at the $\delta(i)$ th qubit to the original location, i.e., the j th qubit, by undoing the fermionic-SWAP operations successively [99]. We should note here that such a way of exploiting the nearest-neighbor fermionic-SWAP gates has been discussed extensively for simulating fermions under the Jordan-Wigner transformation in Refs. [95, 100, 101]. While Eq. (110) might be preferable for a real quantum device, depending on the connectivity of qubits and its native gate set, we employ Eq. (109) for our numerical simulations with classical computers because of the smaller number of operations.

B. Quantum circuit for spin rotation

With the Jordan-Wigner transformation, the local spin operators are represented as

$$\hat{S}_i^x \stackrel{\text{JWT}}{=} \frac{1}{4} (\hat{X}_i \hat{X}_{i_1} + \hat{Y}_i \hat{Y}_{i_1}) \hat{Z}_{\text{JW},i_1 i_i}, \quad (111)$$

$$\hat{S}_i^y \stackrel{\text{JWT}}{=} \frac{1}{4} (\hat{X}_i \hat{Y}_{i_1} - \hat{Y}_i \hat{X}_{i_1}) \hat{Z}_{\text{JW},i_1 i_i}, \quad (112)$$

$$\hat{S}_i^z \stackrel{\text{JWT}}{=} \frac{1}{4} (\hat{Z}_{i_1} - \hat{Z}_{i_1}). \quad (113)$$

Therefore, the rotation operator $e^{-i\beta \hat{S}_i^y} = \prod_{i=1}^L e^{-i\beta \hat{S}_i^y}$ can be given by a product of

$$e^{-i\beta \hat{S}_i^y} \stackrel{\text{JWT}}{=} \exp \left[-i \frac{\beta}{4} (\hat{X}_i \hat{Y}_{i_1} - \hat{Y}_i \hat{X}_{i_1}) \hat{Z}_{\text{JW},i_1 i_i} \right] \quad (114)$$

$$= \left[\prod_{i_1 < k < i_i} \widehat{\text{CZ}}_{i_1 k} \right] \hat{\mathcal{G}}_{i_1 i_i}(\beta) \left[\prod_{i_1 < k < i_i} \widehat{\text{CZ}}_{i_1 k} \right] \quad (115)$$

$$\equiv \widehat{f\mathcal{G}}_{i_1 i_i}(\beta), \quad (116)$$

where the CZ gates in Eq. (115) account for the Jordan-Wigner string in Eq. (114), as shown for the more general case in Eq. (109), and

$$\hat{\mathcal{G}}_{ij}(\theta) = \exp \left[-i \frac{\theta}{4} (\hat{X}_i \hat{Y}_j - \hat{Y}_i \hat{X}_j) \right] \quad (117)$$

is the Givens-rotation gate for $i \neq j$ [94] whose matrix representation in the computational basis is given by

$$\hat{\mathcal{G}}_{ij}(\theta) = \begin{bmatrix} 1 & 0 & 0 & 0 \\ 0 & \cos \frac{\theta}{2} & \sin \frac{\theta}{2} & 0 \\ 0 & -\sin \frac{\theta}{2} & \cos \frac{\theta}{2} & 0 \\ 0 & 0 & 0 & 1 \end{bmatrix}. \quad (118)$$

For deriving this matrix representation, it is useful to notice that $(\hat{X}_i \hat{Y}_j - \hat{Y}_i \hat{X}_j)^2 = 2(1 - \hat{Z}_i \hat{Z}_j)$ and $(1 - \hat{Z}_i \hat{Z}_j)(\hat{X}_i \hat{Y}_j - \hat{Y}_i \hat{X}_j) = 2(\hat{X}_i \hat{Y}_j - \hat{Y}_i \hat{X}_j)$ when $i \neq j$. A more detailed description for

a general single-particle fermion operator is found in Appendix C2. In Eq. (116), we have defined the fermionic Givens-rotation gate $\widehat{f\mathcal{G}}_{i_1 i_i}(\beta)$, which is an extension of the Givens-rotation gate for fermions.

Similarly, the rotation around the z direction by α can be given by

$$e^{-i\alpha \hat{S}_i^z} \stackrel{\text{JWT}}{=} \hat{R}_{Z,i_1} \left(-\frac{\alpha}{2} \right) \hat{R}_{Z,i_i} \left(\frac{\alpha}{2} \right), \quad (119)$$

where

$$\hat{R}_{Z,i}(\theta) = e^{-i\theta \hat{Z}_i / 2}. \quad (120)$$

Figure 5 shows a quantum circuit corresponding to the product of rotations $e^{-i\alpha \hat{S}_i^z} e^{-i\beta \hat{S}_i^y} = \prod_i e^{-i\alpha \hat{S}_i^z} \prod_i e^{-i\beta \hat{S}_i^y}$. For the Givens rotation, we adopt the gate decomposition given in Ref. [102]. One can also find another way of implementing the rotation $e^{-i\beta \hat{S}_i^y}$ in Refs. [45, 94]

C. Quantum circuit for η rotation

With the Jordan-Wigner transformation, the local η operators are represented as

$$\hat{\eta}_i^x \stackrel{\text{JWT}}{=} \frac{e^{i\phi_i}}{4} (\hat{X}_i \hat{X}_{i_1} - \hat{Y}_i \hat{Y}_{i_1}) \hat{Z}_{\text{JW},i_1 i_i}, \quad (121)$$

$$\hat{\eta}_i^y \stackrel{\text{JWT}}{=} -\frac{e^{i\phi_i}}{4} (\hat{X}_i \hat{Y}_{i_1} + \hat{Y}_i \hat{X}_{i_1}) \hat{Z}_{\text{JW},i_1 i_i}, \quad (122)$$

$$\hat{\eta}_i^z \stackrel{\text{JWT}}{=} -\frac{1}{4} (\hat{Z}_{i_1} + \hat{Z}_{i_i}). \quad (123)$$

Therefore, the rotation operator $e^{-i\beta \hat{\eta}_i^y} = \prod_{i=1}^N e^{-i\beta \hat{\eta}_i^y}$ can be given by a product of

$$e^{-i\beta \hat{\eta}_i^y} \stackrel{\text{JWT}}{=} \exp \left[i \frac{e^{i\phi_i} \beta}{4} (\hat{X}_i \hat{Y}_j + \hat{Y}_i \hat{X}_j) \hat{Z}_{\text{JW},i_1 i_i} \right] \quad (124)$$

$$= \left[\prod_{i_1 < k < i_i} \widehat{\text{CZ}}_{i_1 k} \right] \hat{\mathcal{B}}_{i_1 i_i}(-e^{i\phi_i} \beta) \left[\prod_{i_1 < k < i_i} \widehat{\text{CZ}}_{i_1 k} \right] \quad (125)$$

$$\equiv \widehat{f\mathcal{B}}_{i_1 i_i}(-e^{i\phi_i} \beta), \quad (126)$$

where the CZ gates in Eq. (125) account for the Jordan-Wigner string in Eq. (124), as shown for the more general case in Eq. (109), and

$$\hat{\mathcal{B}}_{ij}(\theta) = \exp \left[-i \frac{\theta}{4} (\hat{X}_i \hat{Y}_j + \hat{Y}_i \hat{X}_j) \right]. \quad (127)$$

is the Bogoliubov-transformation gate [94, 102] whose matrix representation in the computational basis is given by

$$\hat{\mathcal{B}}_{ij}(\theta) = \begin{bmatrix} \cos \frac{\theta}{2} & 0 & 0 & -\sin \frac{\theta}{2} \\ 0 & 1 & 0 & 0 \\ 0 & 0 & 1 & 0 \\ \sin \frac{\theta}{2} & 0 & 0 & \cos \frac{\theta}{2} \end{bmatrix}. \quad (128)$$

For deriving this matrix representation, it is useful to notice that $(\hat{X}_i \hat{Y}_j + \hat{Y}_i \hat{X}_j)^2 = 2(1 + \hat{Z}_i \hat{Z}_j)$ and $(1 + \hat{Z}_i \hat{Z}_j)(\hat{X}_i \hat{Y}_j + \hat{Y}_i \hat{X}_j) =$

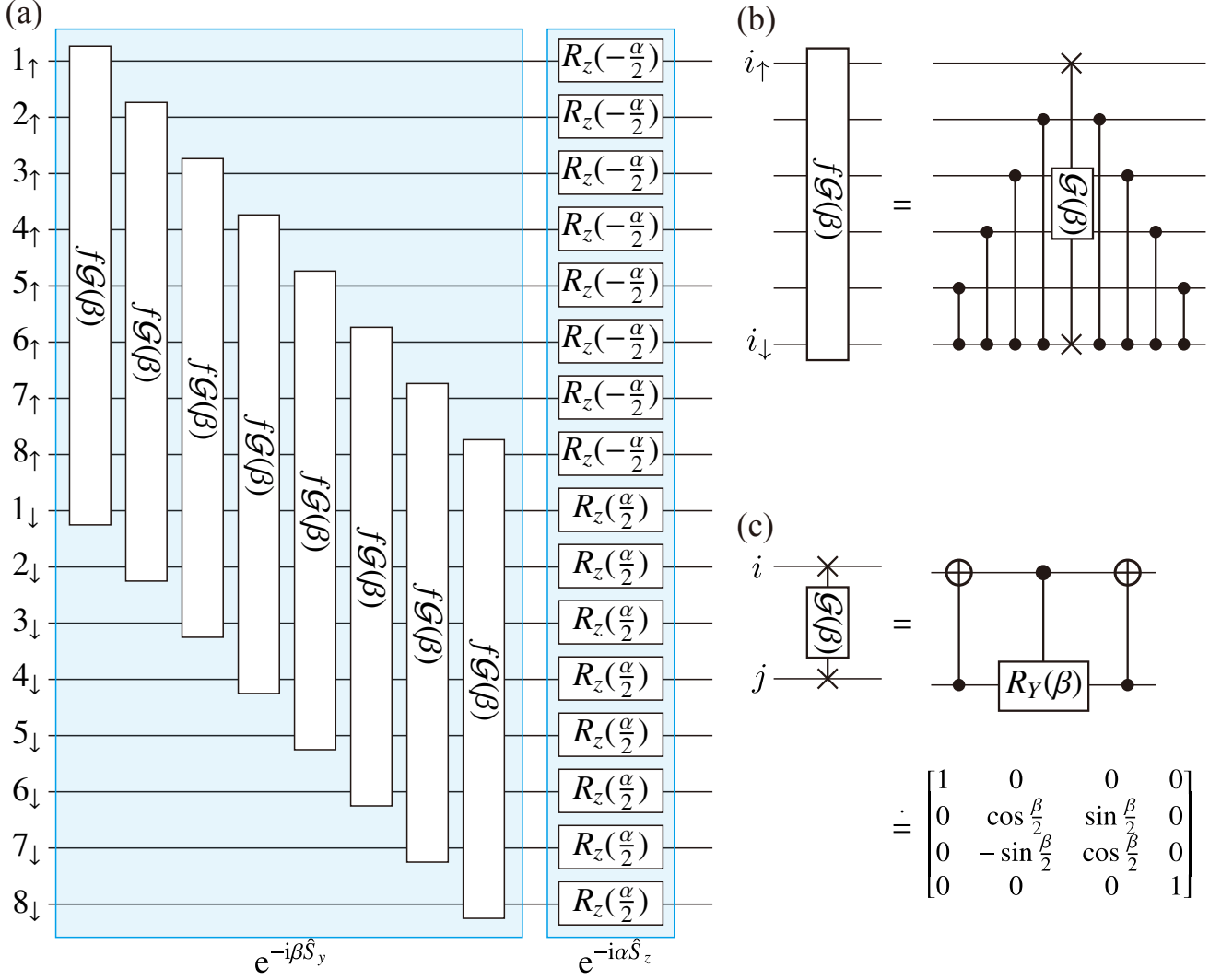


FIG. 5. (a) A quantum circuit to implement spin rotation $e^{-i\alpha\hat{S}_z}e^{-i\beta\hat{S}_y}$ for the 4×2 site Fermi-Hubbard model. $f\mathcal{G}(\beta)$ denotes a fermionic Givens-rotation gate for distant qubits i_\uparrow and i_\downarrow defined in Eq. (116). For evaluation of Eq. (84), $e^{-i\alpha\hat{S}_z}$ is not required and hence the single-qubit rotation $R_z(\theta)$ should be replaced with identity. (b) A decomposition of a fermionic Givens-rotation gate $f\mathcal{G}(\beta)$ into a Givens-rotation gate $\mathcal{G}(\beta)$ sandwiched with CZ gates, as in Eq. (115). (c) A decomposition of the Givens-rotation gate $\mathcal{G}(\beta)$ defined in Eq. (117). Here, $\hat{R}_Y(\theta) = e^{-i\theta\hat{Y}_i/2}$ acting on qubit i . The matrix representation of $\mathcal{G}(\beta)$ with the basis states $\{|0\rangle_i|0\rangle_j, |0\rangle_i|1\rangle_j, |1\rangle_i|0\rangle_j, |1\rangle_i|1\rangle_j\}$ is also shown.

$2(\hat{X}_i\hat{Y}_j + \hat{Y}_i\hat{X}_j)$ when $i \neq j$. A more detailed description for a general anomalous single-particle fermion operator is found in Appendix C 3. In Eq. (126), we have defined the fermionic Bogoliubov-transformation gate $\widehat{f\mathcal{B}}_{i_\uparrow i_\downarrow}(\beta)$, which is an extension of the Bogoliubov-transformation gate for fermions.

Similarly, the rotation around the z direction by α can be given as

$$e^{-i\alpha\hat{\eta}_i^z} \stackrel{\text{JWT}}{=} \hat{R}_{Z,i_\uparrow}\left(-\frac{\alpha}{2}\right)\hat{R}_{Z,i_\downarrow}\left(-\frac{\alpha}{2}\right). \quad (129)$$

Figure 6 shows a quantum circuit corresponding to the product of rotations $e^{-i\alpha\hat{\eta}_i^z}e^{-i\beta\hat{\eta}_i^y} = \prod_i e^{-i\alpha\hat{\eta}_i^z} \prod_i e^{-i\beta\hat{\eta}_i^y}$. For the Bogoli-

ubov transformation, we adopt the gate decomposition given in Ref. [102]. One can also find another way of implementing the rotation $e^{-i\beta\hat{\eta}_i^y}$ in Ref. [94].

VII. NUMERICAL SIMULATIONS

In this section, we demonstrate the Krylov-extended SAVQE method by numerically simulating the two-component Fermi-Hubbard model on the 4×2 cluster under open boundary conditions at half filling, i.e., one fermion per site. To speed up the calculations, a simple strategy of parallelizing numerical simulations is employed (see Appendix D).

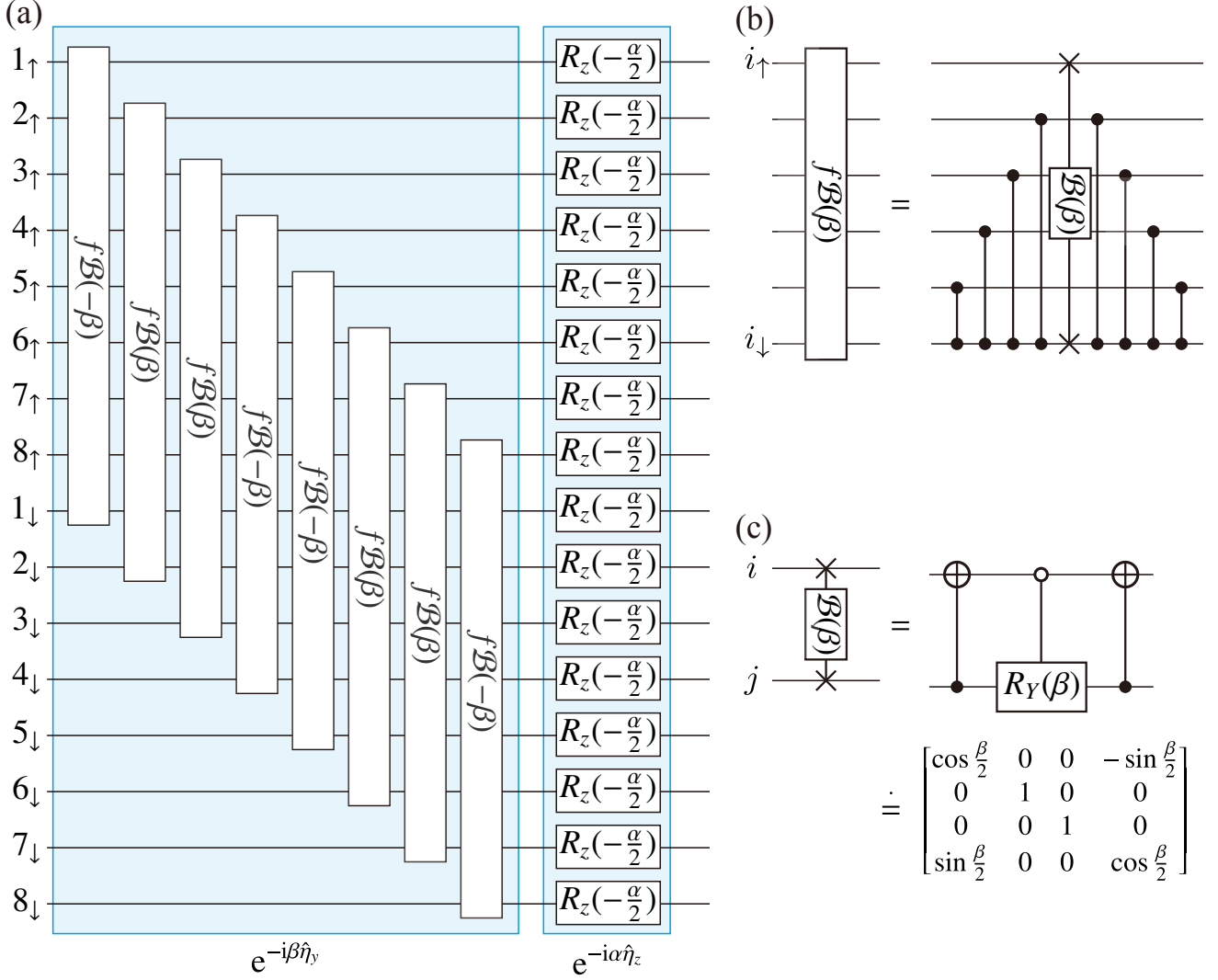


FIG. 6. (a) A quantum circuit to implement η rotation $e^{-i\beta\hat{\eta}_y}e^{-i\alpha\hat{\eta}_z}$ for the 4×2 site Fermi-Hubbard model. $f\mathcal{B}(\beta)$ denotes a fermionic Bogoliubov-transformation gate for distant qubits i_\uparrow and i_\downarrow defined in Eq. (126). For evaluation of Eq. (84), $e^{-i\alpha\hat{\eta}_z}$ is not required and hence the single-qubit rotation $R_z(\theta)$ should be replaced with identity. (b) A decomposition of a fermionic Bogoliubov-transformation gate $f\mathcal{B}(\beta)$ into a Bogoliubov-transformation gate $\mathcal{B}(\beta)$ sandwiched with CZ gates, as in Eq. (125), assuming that site i represented by qubits i_\uparrow and i_\downarrow belongs to B sublattice. When site i represented by qubits i_\uparrow and i_\downarrow belongs to A sublattice, $f\mathcal{B}(\beta)$ and $\mathcal{B}(\beta)$ should be replaced with $f\mathcal{B}(-\beta)$ and $\mathcal{B}(-\beta)$, respectively. (c) A decomposition of the Bogoliubov-transformation gate $f\mathcal{B}(\beta)$ defined in Eq. (127). Here, $R_Y(\theta) = e^{-i\theta\hat{Y}_i/2}$ acting on qubit i . The matrix representation of $\mathcal{B}(\beta)$ with the basis states $\{|0\rangle_i|0\rangle_j, |0\rangle_i|1\rangle_j, |1\rangle_i|0\rangle_j, |1\rangle_i|1\rangle_j\}$ is also shown.

A. Variational state

As a variational state $|\psi(\theta)\rangle$ in Eq. (30) for the ground state of the Fermi-Hubbard model, we first construct a product state of two-site bonding orbitals for each spin of fermions by applying Hadamard, Pauli X , and CNOT gates to $|0\rangle^{\otimes N}$ in an appropriate manner [see Fig. 7(a)]. Note that the bonding state is equivalent to one of the Bell states, $\frac{1}{\sqrt{2}}(|0\rangle|1\rangle + |1\rangle|0\rangle)$ (for its preparation, see Ref. [103]). The preparation of the product state of bonding orbitals is independent of the variational parameters and hence corresponds to $\hat{W}|0\rangle^{\otimes N}$ in Eq. (30), also

indicated in Fig. 7(a). Note that the total number of fermions for the state represented by this first part of the quantum circuit is $N/2 = L$ (i.e., half filling) with the same number of up and down fermions, assuming that L is even. This implies that the expectation values of \hat{S}_z and $\hat{\eta}_z$ are both zero. As described below, we will construct a parametrized part of the quantum circuit for the variational state $|\psi(\theta)\rangle$ that preserves these features, i.e., $\langle\psi(\theta)|\hat{S}_z|\psi(\theta)\rangle = \langle\psi(\theta)|\hat{\eta}_z|\psi(\theta)\rangle = 0$ for an arbitrary set of variational parameters θ . However, this does not necessarily imply that the expectation values of \hat{S}^2 and $\hat{\eta}^2$ are zero. Instead, these expectation values are generally nonzero, as shown later in Figs. 12(c) and 12(d), for example.

In order to construct a parametrized part of the quantum circuit for the variational state $|\psi(\theta)\rangle$ in Eq. (30), let N_{hop} (N_{int}) be the number of hopping (interaction) terms in the Hamiltonian $\hat{\mathcal{H}}$ in Eq. (52). For $1 \leq k \leq N_{\text{hop}}$ in Eq. (30), we apply

$$\begin{aligned} \hat{U}_k(\theta_k) &= \exp(-i\hat{\mathcal{F}}_{i_k j_k} \theta_k / 2) \\ &= \hat{I} \cos \frac{\theta_k}{2} - i\hat{\mathcal{F}}_{i_k j_k} \sin \frac{\theta_k}{2} \\ &\stackrel{\text{JWT}}{=} \left[\prod_{i_k \lesssim m \lesssim j_k} \widehat{\text{CZ}}_{i_k m} \right] \hat{f}_{i_k j_k}(\theta_k) \left[\prod_{i_k \lesssim m \lesssim j_k} \widehat{\text{CZ}}_{i_k m} \right] \end{aligned} \quad (130)$$

to every pair of qubits i_k and j_k between which the hopping (t) term is present in the Hamiltonian $\hat{\mathcal{H}}$. Since the long-range fermionic-SWAP operator $\hat{\mathcal{F}}_{i_k j_k}$ is nonlocal, the operator $\hat{U}_k(\theta_k)$ above operates also onto all qubits between qubits i_k and j_k [see Fig. 7(b)]. We refer to this gate as an $e\mathcal{F}$ SWAP gate. In Eq. (130), the parametrized two-qubit gate $\hat{f}_{ij}(\theta)$ is defined as

$$\hat{f}_{ij}(\theta) \equiv \exp(-i\hat{f}_{ij}\theta/2) \quad (131)$$

and \hat{f}_{ij} is given in Eq. (107). Note that the last equality in Eq. (130) can be proved simply from Eq. (106) and $\hat{f}_{ij}^2 = \hat{I}$. Since $\hat{f}_{ij} = \hat{S}_{ij} \widehat{\text{CZ}}_{ij} = \hat{S}_{ij} + (\widehat{\text{CZ}}_{ij} - \hat{I})$ and \hat{S}_{ij} commutes with $\widehat{\text{CZ}}_{ij}$, the parametrized two-qubit gate $\hat{f}_{ij}(\theta)$ in Eq. (131) can be given by a product of the exponential-SWAP gate $\exp(-i\hat{S}_{ij}\theta/2)$ and the controlled-phase gate $\text{CPHASE}_{ij}(\theta) \equiv \exp[-i(\widehat{\text{CZ}}_{ij} - \hat{I})\theta/2]$, i.e.,

$$\begin{aligned} \hat{f}_{ij}(\theta) &= \exp(-i\hat{S}_{ij}\theta/2) \text{CPHASE}_{ij}(\theta) \\ &= \begin{bmatrix} e^{-i\theta/2} & 0 & 0 & 0 \\ 0 & \cos \frac{\theta}{2} & -i \sin \frac{\theta}{2} & 0 \\ 0 & -i \sin \frac{\theta}{2} & \cos \frac{\theta}{2} & 0 \\ 0 & 0 & 0 & e^{-i\theta/2} \end{bmatrix} \begin{bmatrix} 1 & 0 & 0 & 0 \\ 0 & 1 & 0 & 0 \\ 0 & 0 & 1 & 0 \\ 0 & 0 & 0 & e^{i\theta} \end{bmatrix} \\ &= \begin{bmatrix} e^{-i\theta/2} & 0 & 0 & 0 \\ 0 & \cos \frac{\theta}{2} & -i \sin \frac{\theta}{2} & 0 \\ 0 & -i \sin \frac{\theta}{2} & \cos \frac{\theta}{2} & 0 \\ 0 & 0 & 0 & e^{+i\theta/2} \end{bmatrix} \end{aligned} \quad (132)$$

in the computational basis [also see Fig. 7(b)]. From this matrix representation, we can indeed confirm directly that $\hat{f}_{ij}(\theta) = \hat{I} \cos \frac{\theta}{2} - i\hat{f}_{ij} \sin \frac{\theta}{2}$.

For $N_{\text{hop}} + 1 \leq k \leq N_{\text{hop}} + N_{\text{int}}$, we apply

$$\hat{U}_k(\theta_k) = \exp(-i\hat{Z}_{i_k} \hat{Z}_{j_k} \theta_k / 2) \quad (133)$$

to every pair of qubits i_k and j_k between which the interaction (U_{H}) term is present in the Hamiltonian $\hat{\mathcal{H}}$. As shown in Fig. 7(c), this gate ($e\mathcal{Z}\mathcal{Z}$ gate) is easily implemented in the circuit.

We define the depth D of the entire quantum circuit for the variational state $|\psi(\theta)\rangle$ in such a way that a single layer of gates contains the sequences of $N_{\text{hop}} + N_{\text{int}}$ gates, $\prod_{k=1}^{N_{\text{hop}}+N_{\text{int}}} \hat{U}_k(\theta_k)$, and hence the total number N_v of the variational parameters is $N_v = D(N_{\text{hop}} + N_{\text{int}})$ [see Fig. 7(a)]. Because $\hat{\mathcal{F}}_{ij}^2 = \hat{I}$ and $(\hat{Z}_i \hat{Z}_j)^2 = \hat{I}$ are satisfied, this parametrized variational state allows us to use the parameter-shift rules for derivatives described in Sec. III B.

B. Suzuki-Trotter decomposition

As described in Sec. IV, we employ the QPM to generate the Hamiltonian power $\hat{\mathcal{H}}^n$ for the Krylov subspace \mathcal{U} in Eq. (37). In the QPM, the Hamiltonian power $\hat{\mathcal{H}}^n$ is approximated with controlled accuracy by a linear combination of ST decomposed time-evolution operators. In particular, as shown in Eqs. (39) and (40), we employ the second-order symmetric ST decomposition of the time-evolution operator $e^{-i\hat{\mathcal{H}}\Delta}$:

$$e^{-i\hat{\mathcal{H}}\Delta} = \hat{S}_2(\Delta) + O(\Delta^3) \quad (134)$$

with

$$\begin{aligned} \hat{S}_2(\Delta) &= e^{-i\hat{\mathcal{H}}^A \Delta/2} e^{-i\hat{\mathcal{H}}^B \Delta/2} e^{-i\hat{\mathcal{H}}^C \Delta/2} \\ &\quad \times e^{-i\hat{\mathcal{H}}^U \Delta} e^{-i\hat{\mathcal{H}}^C \Delta/2} e^{-i\hat{\mathcal{H}}^B \Delta/2} e^{-i\hat{\mathcal{H}}^A \Delta/2}, \end{aligned} \quad (135)$$

where $\hat{\mathcal{H}}^A$, $\hat{\mathcal{H}}^B$, and $\hat{\mathcal{H}}^C$ are the hopping (t) terms between sites connected by different types of bonds and $\hat{\mathcal{H}}^U$ is the interaction (U_{H}) term in the Fermi-Hubbard Hamiltonian $\hat{\mathcal{H}}$, i.e., $\hat{\mathcal{H}} = \hat{\mathcal{H}}^A + \hat{\mathcal{H}}^B + \hat{\mathcal{H}}^C + \hat{\mathcal{H}}^U$ (see Fig. 8). This decomposition scheme is used for $\hat{H}_{\text{ST}}^n(\Delta)$ in Eq. (40) and thus also for $\hat{H}_{\text{ST}(1)}^n(\Delta)$ in Eq. (41).

C. Numerical results

In order to assess the accuracy of the Krylov-extended SAVQE, we evaluate the variational energy

$$E_0(\theta^{(x)}) = \langle \Psi_{\mathcal{U}}(\theta^{(x)}) | \hat{\mathcal{H}} | \Psi_{\mathcal{U}}(\theta^{(x)}) \rangle, \quad (136)$$

the fidelity of the ground state

$$F(\theta^{(x)}) = |\langle \Psi_0 | \Psi_{\mathcal{U}}(\theta^{(x)}) \rangle|^2, \quad (137)$$

the expectation value of the total spin squared

$$\langle \hat{S}^2 \rangle_{\theta^{(x)}} = \langle \Psi_{\mathcal{U}}(\theta^{(x)}) | \hat{S}^2 | \Psi_{\mathcal{U}}(\theta^{(x)}) \rangle, \quad (138)$$

and the expectation value of the total η squared

$$\langle \hat{\eta}^2 \rangle_{\theta^{(x)}} = \langle \Psi_{\mathcal{U}}(\theta^{(x)}) | \hat{\eta}^2 | \Psi_{\mathcal{U}}(\theta^{(x)}) \rangle, \quad (139)$$

as a function of the number of the optimization iteration x in Eq. (14). Here, $|\Psi_0\rangle$ is the exact ground state obtained by the Lanczos exact diagonalization method,

$$|\Psi_{\mathcal{U}}(\theta^{(x)})\rangle = \frac{|\Psi_{\mathcal{U}}^{(0)}(\theta^{(x)})\rangle}{\sqrt{\langle \Psi_{\mathcal{U}}^{(0)}(\theta^{(x)}) | \Psi_{\mathcal{U}}^{(0)}(\theta^{(x)}) \rangle}} \quad (140)$$

is the approximated ground state with the variational parameters $\theta^{(x)}$ at the x th optimization iteration, and $|\Psi_{\mathcal{U}}^{(0)}(\theta^{(x)})\rangle$ is given in Eq. (9). All these quantities except for the fidelity $F(\theta^{(x)})$ can be calculated as in Eq. (50) along with Eq. (84). For the fidelity calculation, a careful treatment for the normalization factor of the projection operator is required (see

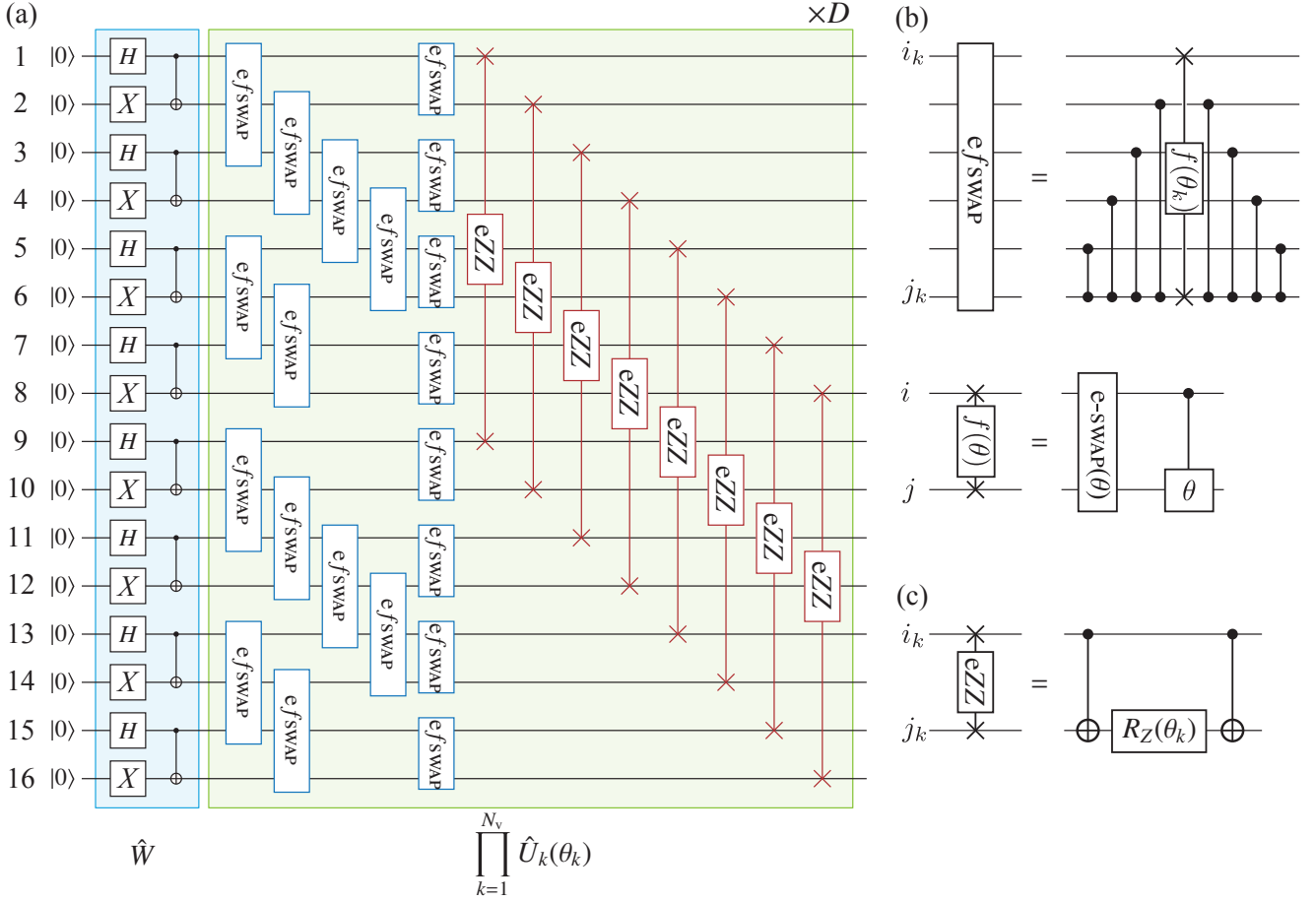


FIG. 7. (a) A quantum circuit for preparing the variational state $|\psi(\theta)\rangle = \prod_{k=1}^{N_v} \hat{U}_k(\theta_k) \hat{W}|0\rangle^{\otimes N}$. The parametrized gates corresponding to $\hat{U}_k(\theta_k) = \exp(-i\hat{\mathcal{F}}_{i_k j_k} \theta_k/2)$ and $\hat{U}_k(\theta_k) = \exp(-i\hat{Z}_{i_k} \hat{Z}_{j_k} \theta_k/2)$ are denoted as $e f_{\text{SWAP}}$ and eZZ , respectively. The qubit numbers indicated in the left most side correspond to the numbering of qubits in Fig. 8 for the two-component Fermi-Hubbard model on the 4×2 cluster. (b) A decomposition of the $e f_{\text{SWAP}}$ gate $\hat{U}_k(\theta_k) = \exp(-i\hat{\mathcal{F}}_{i_k j_k} \theta_k/2)$, as given in Eq. (130). The lower part of the panel shows that the parametrized gate $\hat{f}_{ij}(\theta) = \exp(-i\hat{f}_{ij} \theta/2)$ can be expressed as a product of the exponential-SWAP gate $\exp(-i\hat{S}_{ij} \theta/2)$ and the controlled-phase gate $\text{CPHASE}_{ij}(\theta)$ [also see Eq. (132)]. (c) A decomposition of the eZZ gate $\hat{U}_k(\theta_k) = \exp(-i\hat{Z}_{i_k} \hat{Z}_{j_k} \theta_k/2)$.

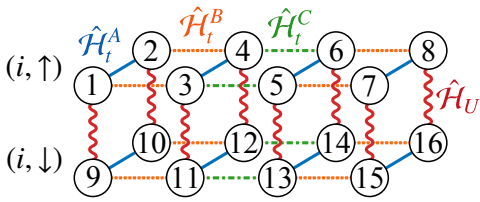


FIG. 8. In the ST decomposition, the Fermi-Hubbard Hamiltonian $\hat{\mathcal{H}}$ on the 4×2 cluster is divided into four parts $\hat{\mathcal{H}}_t^A$, $\hat{\mathcal{H}}_t^B$, $\hat{\mathcal{H}}_t^C$, and $\hat{\mathcal{H}}_U$, where $\hat{\mathcal{H}}_t^A$, $\hat{\mathcal{H}}_t^B$, and $\hat{\mathcal{H}}_t^C$ are the hopping (t) terms between sites connected by different types of bonds (indicated by blue, orange, and green lines, respectively), and $\hat{\mathcal{H}}_U$ is the interaction (U_H) term (indicated by red curly lines). Circles represent qubits that are numbered from 1 to 8 for single-particle states at site $i (= 1, 2, \dots, 8)$ with spin up and from 9 to 16 for single-particle states at site $i (= 1, 2, \dots, 8)$ with spin down. This numbering of qubits follows the spin-uniform labeling (see Fig. 11).

Appendix E). Note also that the expectation values of \hat{S}_z and \hat{n}_z are both zero by construction, i.e., $\langle \Psi_{\mathcal{U}}(\theta^{(x)}) | \hat{S}_z | \Psi_{\mathcal{U}}(\theta^{(x)}) \rangle = \langle \Psi_{\mathcal{U}}(\theta^{(x)}) | \hat{n}_z | \Psi_{\mathcal{U}}(\theta^{(x)}) \rangle = 0$, independently of $\theta^{(x)}$.

The numerical results shown in this section are all for the Hubbard interaction $U_H/t = 4$. Although the learning rate τ of the parameter optimization in Eq. (14) can be varied during the optimization iteration in general, here we fix $\tau = 0.025/t$ throughout the optimization iteration. The parameter Δ appearing in Eq. (40) for the QPM is set to be $\Delta = 0.05/t$. When the first-order Richardson extrapolation is employed, the expected systematic error for approximating the Hamiltonian power $\hat{\mathcal{H}}^n$ is $O(\Delta^4)$ [see Eq. (42)]. Indeed, we find that the errors in \mathbf{H} and \mathbf{S} are negligible for this Δ value.

Let us first examine the vanishing-gradient or the barren-plateau problem [104] for our particular study. While the barren-plateau problem in the context of variational quantum algorithms has been discussed often with its dependence on the number of qubits, our focus here is on the comparison

between the natural gradient and the gradient of the cost function, i.e., the expectation value of energy $E_0(\theta)$, for a fixed number of qubits. Figure 9 shows the variance of the natural gradient defined as

$$\sigma_{\text{NG}}^2 \equiv \frac{1}{R} \sum_{r=1}^R \left[\frac{1}{N_v} \sum_{k=1}^{N_v} [\tilde{\nabla} E_0(\theta_r)]_k^2 \right], \quad (141)$$

where $\theta_r = \{\theta_{r,k}\}_{k=1}^{N_v}$ is a set of the randomly generated variational parameters, R is the number of the random instances, and

$$\tilde{\nabla} E_0(\theta_r) \equiv [\mathbf{G}(\theta_r)]^{-1} \nabla E_0(\theta_r) \quad (142)$$

is the natural gradient [54] of the expectation value of energy $E_0(\theta_r)$ [see Eq. (14)]. In the calculations, we set $d_{\mathcal{U}} = 1$ and the projection operator of the form $\hat{\mathcal{P}} = \hat{I}$ (i.e., without any symmetry-projection operators), and we estimate σ_{NG}^2 from $R = 64$ random instances. The error bar in Fig. 9 indicates the standard error of the mean. For comparison, we also calculate the variance of the gradient

$$\sigma_{\text{G}}^2 \equiv \frac{1}{R} \sum_{r=1}^R \left[\frac{1}{N_v} \sum_{k=1}^{N_v} [\nabla E_0(\theta_r)]_k^2 \right], \quad (143)$$

in the same manner with the same sets of the randomly generated variational parameters. In Eqs. (141) and (143), it is assumed that the averages of the natural gradient and the gradient over the random instances vanish.

In Euclidean space, the natural gradient should coincide with the gradient. However, as shown in Fig. 9, this is not the case here. Namely, the variational-parameter space is certainly non Euclidean. Indeed, the steepest-descent direction of $E_0(\theta)$ in the variational-parameter space, which can be seen as a Riemannian manifold where the Fubini-Study metric tensor $\mathbf{G}(\theta)$ is attributed at each point θ , is in general not along $-\nabla E_0(\theta)$ but along $-\tilde{\nabla} E_0(\theta) = -[\mathbf{G}(\theta)]^{-1} \nabla E_0(\theta)$ (see Appendix A). Even when the natural gradient is used, the variance decreases exponentially in D until it is saturated for large D , which is similar to the results reported in Ref. [104]. This indicates that the natural gradient cannot solve the barren-plateau problem. However, it is remarkable to notice in Fig. 9 that the variance of the natural gradient is more than one order of magnitude larger than that of the gradient. The larger variance of the natural gradient than that of the gradient suggests that the natural gradient can alleviate the barren-plateau problem by capturing the correct steepest-descent direction at each point θ in the variational-parameter space, at the expense of computing the Fubini-Study metric tensor $\mathbf{G}(\theta)$.

Figure 10 shows the ground-state energy and the ground-state fidelity as a function of the number D of the layers of the parametrized gates (see Fig. 7) calculated for the variational states with the full projection operator $\hat{\mathcal{P}} = \hat{\mathcal{P}}^{(\eta)} \hat{\mathcal{P}}^{(S)} \hat{\mathcal{P}}^{(\alpha)}$. We perform 64 independent calculations with different sets of random initial parameters $\theta^{(1)}$, and we evaluate these quantities

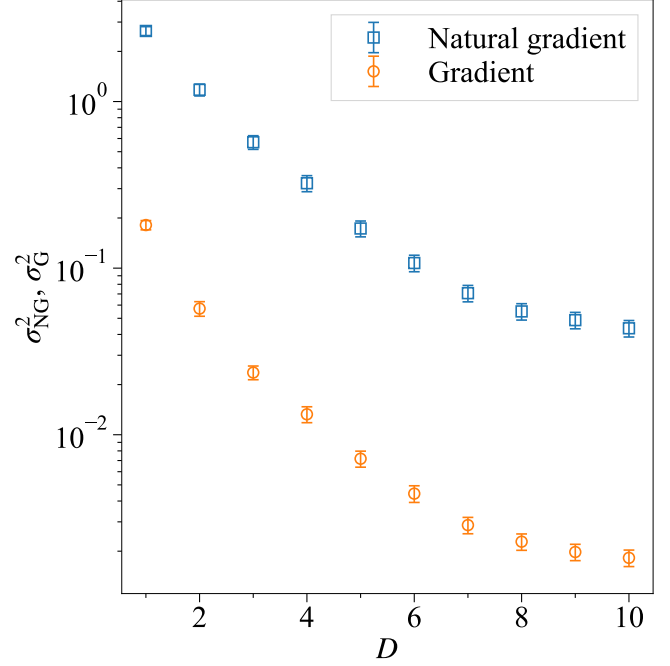


FIG. 9. Variance of the natural gradient σ_{NG}^2 (squares) and that of the gradient σ_{G}^2 (circles) as a function of the number D of layers in a quantum circuit shown in Fig. 7 for the parametrized variational state $|\psi(\theta)\rangle$ without any symmetry projections. The Fermi-Hubbard model on the 4×2 cluster is considered and hence there are $N = 16$ qubits. The number N_v of variational parameters increase linearly in D , i.e., $N_v = 28D$ in this case.

for the well optimized variational parameters $\theta^{(1000)}$. Figure 10 shows the results averaged over the 64 independent calculations and also the best results in terms of the fidelity among the 64 independent calculations. For comparison, we also show the results obtained for a Hamiltonian variational ansatz (HVA) [105, 106], starting also with the initial state $\hat{W}|0\rangle^{\otimes N}$, which also preserves the spatial, S , and η symmetry without using the projection operators. Each layer of the HVA consists of $O(L^2)$ two qubit gates due to the Jordan-Wigner string, as in $|\psi(\theta)\rangle$. Further details of the HVA are found in Appendix F.

As shown in Fig. 10(b), the fidelity of $F \approx 0.949$ is achieved at $D = 2$ and $d_{\mathcal{U}} = 1$ on average, and $F \approx 0.991$ is achieved at best. By increasing the dimension of the subspace to $d_{\mathcal{U}} = 2$, $F \approx 0.922$ on average and $F \approx 0.980$ at best at $D = 1$, and $F \approx 0.994$ on average and $F \approx 0.999$ at best at $D = 2$ are achieved. Accordingly, as shown in Fig. 10(a), the ground-state energy E_0 is also systematically improved with increasing the number D of layers or the Krylov subspace dimension $d_{\mathcal{U}}$ to attain almost the exact energy already at $D = 1$ and $d_{\mathcal{U}} = 2$ at best and the exact energy at $D = 2$ on average. On the other hand, the HVA, which also respects all the Hamiltonian symmetry, requires six layers on average and four layers at best to achieve high fidelity of 0.9. These results are consistent with the empirical observation that the more symmetry

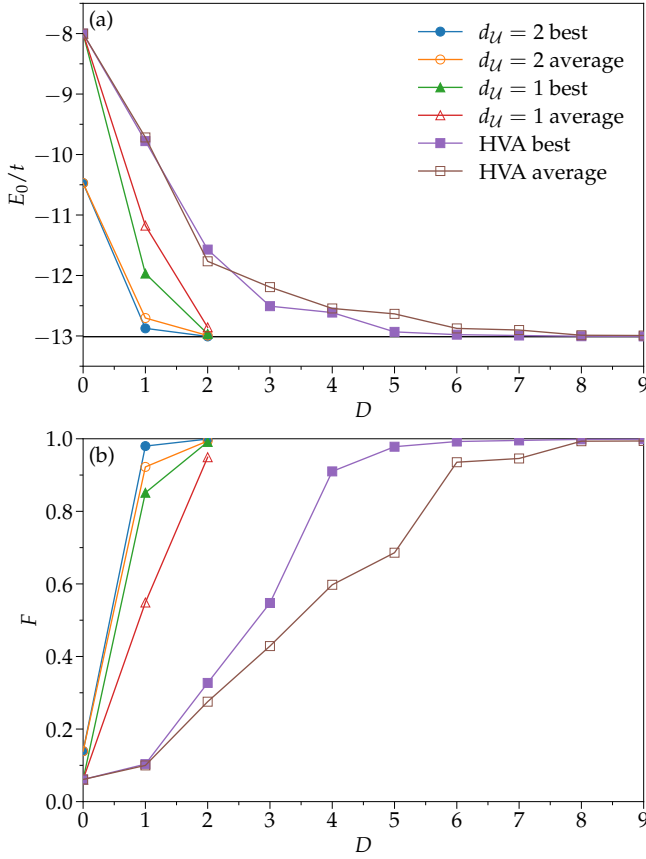


FIG. 10. (a) The ground-state energy E_0 and (b) the ground-state fidelity F as a function of the number D of layers for various variational states with the Krylov subspace dimension $d_U = 1$ and 2. The horizontal line in (a) indicates the exact ground-state energy $E_{\text{exact}} (= -13.01250315t)$ obtained by the Lanczos exact-diagonalization method. For comparison, the results obtained for a HVA are also shown. Here, we perform 64 different independent calculations with different sets of random initial parameters $\theta^{(1)}$ and show the results averaged over these 64 independent calculations (open symbols) and the best results in terms of the fidelity among these 64 independent calculations (solid symbols).

is broken to restore it by projection, the better quality a variational wave function acquires [107].

It should be noted that applying the projection operators and the Hamiltonian powers in the Krylov-extended SAVQE requires more gates than the HVA, as summarized in Table I. Moreover, the number of CZ gates required for the Jordan-Wigner string depends on the way of mapping fermion indexes (i.e., local single-particle states) to qubits. Figure 11 shows two particular labeling schemes, which we refer to as spin-uniform and spin-alternating labelings. Generally, the full projection operator requires $O(L^2)$ more two-qubit gates, and the Hamiltonian power requires $O(L)$ two-qubit gates (assuming the Fermi-Hubbard model on the ladder lattice as in Fig. 8), which are comparable to one to two more layers in the HVA (see Appendix F). As shown in Table I, CZ gates for the spin and η rotations can be eliminated by using the spin-alternating labeling, while the number of CZ gates for

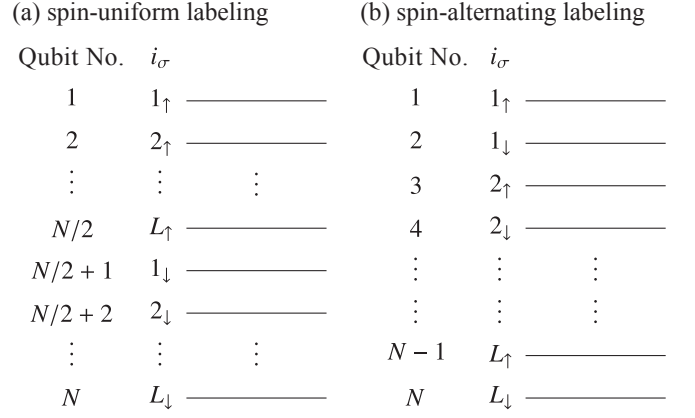


FIG. 11. Labeling schemes for qubits. (a) spin-uniform labeling and (b) spin-alternating labeling. Here, $L = N/2$ is the number of sites.

the spatial-symmetry operation is double. Furthermore, the number of CZ gates for the time-evolution operator by the hopping term scales similarly but with different prefactors in the two different labelings for the Fermi-Hubbard model on the ladder lattice. Overall, the two labeling schemes are comparable in terms of the number of CZ gates required for the Fermi-Hubbard model on the ladder lattice. However, the spin-alternating labeling would be preferred for the Fermi-Hubbard model on a two-dimensional square lattice.

Now we show the results not only for the variational states with the full projection operator $\hat{\mathcal{P}} = \hat{\mathcal{P}}^{(\eta)}\hat{\mathcal{P}}^{(S)}\hat{\mathcal{P}}^{(\alpha)}$, but also with various combinations of the projection operators, $\hat{\mathcal{P}}^{(\alpha)}$, $\hat{\mathcal{P}}^{(S)}$, and $\hat{\mathcal{P}}^{(\eta)}$, to resolve the efficiency of each projection operator. Figure 12 shows the results for the quantum circuit of depth $D = 1$ and the Krylov-subspace dimension $d_U = 1$. Each of the results is average over 64 independent calculations with different sets of random initial parameters $\theta^{(1)}$ distributed in $[-0.05, 0.05]$. As shown in Fig. 12(b), the fidelity at $x = 1$ is essentially zero for all cases with these 64 different sets of initial parameters $\theta^{(1)}$. As compared to the results for the bare variational state $|\psi(\theta)\rangle$ without any projection operators, a slight improvement in the ground-state energy and a substantial improvement in the ground-state fidelity are found for $\hat{\mathcal{P}}^{(S)}|\psi(\theta)\rangle$ and also for $\hat{\mathcal{P}}^{(\alpha)}|\psi(\theta)\rangle$. On the other hand, a slight improvement in the energy and no improvement in the fidelity are found for $\hat{\mathcal{P}}^{(\eta)}|\psi(\theta)\rangle$. Among the variational states with double projection operators, those with the spatial-symmetry projection, $\hat{\mathcal{P}}^{(S)}\hat{\mathcal{P}}^{(\alpha)}|\psi(\theta)\rangle$ and $\hat{\mathcal{P}}^{(\eta)}\hat{\mathcal{P}}^{(\alpha)}|\psi(\theta)\rangle$, give the better energy than that without the spatial-symmetry projection, $\hat{\mathcal{P}}^{(\eta)}\hat{\mathcal{P}}^{(S)}|\psi(\theta)\rangle$. However, the fidelity for $\hat{\mathcal{P}}^{(S)}\hat{\mathcal{P}}^{(\alpha)}|\psi(\theta)\rangle$ is substantially larger than that for $\hat{\mathcal{P}}^{(\eta)}\hat{\mathcal{P}}^{(\alpha)}|\psi(\theta)\rangle$. It is not surprising that the variational state with the full projection operator, i.e., $\hat{\mathcal{P}}^{(\eta)}\hat{\mathcal{P}}^{(S)}\hat{\mathcal{P}}^{(\alpha)}|\psi(\theta)\rangle$, achieves the best ground-state energy and fidelity.

As expected, $\langle \hat{S}^2 \rangle_{\theta^{(x)}}$ and $\langle \hat{\eta}^2 \rangle_{\theta^{(x)}}$ are exactly zero, regardless of the values of variational parameters $\theta^{(x)}$, for the variational

TABLE I. Order estimation and counting of the number of two-qubit gates required for the symmetry and the time-evolution operations of the two-component Fermi-Hubbard model in a ladder lattice structure under open-boundary conditions such as the one shown in Fig. 1. Two labeling schemes for qubits, spin-uniform and spin-alternating labelings, are considered (see Fig. 11). “ $\times 2$ ” (“ $\times 4$ ”) in the right-most column indicates that the number of the CZ gates required for the Jordan-Wigner (JW) string in the spin-alternating labeling is approximately doubled (quadrupled) as compared with that in the spin-uniform labeling. “Givens”, “Bogoliubov”, and “Exchange” are three different types of two-qubit gates defined in Eqs. (117), (127), and (F7), respectively. L is the number of sites and $\hat{\mathcal{H}}_t \equiv \hat{\mathcal{H}} - \hat{\mathcal{H}}_U$ is the hopping term of the Hamiltonian.

unitary operators	two-qubit gates			
	spin-uniform labeling		spin-alternating labeling	
	CZ and SWAP	CZ for JW string	CZ and SWAP	CZ for JW string
spatial symmetry \hat{g}	$O(L)$	$O(L^2)$	$O(L)$	$O(L^2) \times 2$
spin rotation $e^{-i\delta_y \beta}$	Givens L	CZ for JW string $2L(L-1)$	Givens L	CZ for JW string 0
η rotation $e^{-i\hat{\eta}_y \beta}$	Bogoliubov L	CZ for JW string $2L(L-1)$	Bogoliubov L	CZ for JW string 0
time evolution by hopping $e^{-i\hat{\mathcal{H}}_t \Delta}$ ^a	Exchange $O(L)$	CZ for JW string $O(L)$ ^b	Exchange $O(L)$	CZ for JW string $O(L) \times 4$ ^c
time evolution by interaction $e^{-i\hat{\mathcal{H}}_U \Delta}$	CNOT $2L$	CZ for JW string 0	CNOT $2L$	CZ for JW string 0

^a The same counting of the number of the CZ gates is applied for the product of exponentiated fermionic-SWAP operators [defined in Eq. (130)] in the variational state $|\psi(\theta)\rangle$ in Eq. (30).

^b For the Fermi-Hubbard model on a one-dimensional (two-dimensional square) lattice under open-boundary conditions, the number of the CZ gates required is 0 [$O(L^{3/2})$].

^c For the Fermi-Hubbard model on a one-dimensional (two-dimensional square) lattice under open boundary conditions, the number of the CZ gates required is $O(L)$ [$O(L^{3/2})$].

states containing the spin-symmetry projection $\hat{\mathcal{P}}^{(S)}$ and the η -symmetry projection $\hat{\mathcal{P}}^{(\eta)}$, respectively, shown in Figs. 12(c) and 12(d). It is also found that while $\langle \hat{\eta}^2 \rangle_{\theta^{(x)}}$ for the variational states without $\hat{\mathcal{P}}^{(\eta)}$ tends to decrease toward zero with increasing the optimization iteration x , $\langle \hat{S}^2 \rangle_{\theta^{(x)}}$ for the variational states without $\hat{\mathcal{P}}^{(S)}$ remains finite. Moreover, $\langle \hat{S}^2 \rangle_{\theta^{(x)}}$ for the variational state $\hat{\mathcal{P}}^{(\eta)}|\psi(\theta)\rangle$ converges to a larger value than that for the bare variational state $|\psi(\theta)\rangle$. This can explain the less improved fidelity for $\hat{\mathcal{P}}^{(\eta)}|\psi(\theta)\rangle$ in Fig. 12(b), although the energy is improved better than that for the bare variational state $|\psi(\theta)\rangle$ [see Fig. 12(a)], in accordance with the variational principle.

Figure 13 shows the same results as in Fig. 12 but with the subspace dimension $d_{\mathcal{U}} = 2$. Here, the initial variational parameters are set to be the optimal values obtained with $d_{\mathcal{U}} = 1$ in Fig. 12. As shown in Figs. 13(a) and 13(b), by expanding the Krylov subspace, both the ground-state energy and the ground-state fidelity are significantly improved from $d_{\mathcal{U}} = 1$, without increasing the number of the variational parameters. Note that the most noticeable improvement of the energy and the fidelity is achieved already at the moment when the Krylov subspace is expanded without further optimizing the variational parameters. The further improvement of these quantities is also observed with increasing the optimization iteration x . The relative accuracy among the eight different variational states follows essentially the same trend as in the case with $d_{\mathcal{U}} = 1$ shown in Fig. 12. However, we should note that the great improvement of $\langle \hat{S}^2 \rangle_{\theta^{(x)}}$ and $\langle \hat{\eta}^2 \rangle_{\theta^{(x)}}$ is not found even

when the Krylov subspace is expanded to $d_{\mathcal{U}} = 2$, as shown in Figs. 13(c) and 13(d).

Figure 14 shows the same results as in Fig. 12 but with the circuit of depth $D = 2$. As shown in Fig. 14(a), the relative error of the ground-state energy is decreased by an order of magnitude for all the variational states as compared with that for the variational states with $D = 1$ in Fig. 12(a). Similarly, the ground-state fidelity in Fig. 14(b) is increased almost two times larger than that for the variational states with $D = 1$ in Fig. 12(b). We can also notice in Fig. 14(c) that no improvement of $\langle \hat{S}^2 \rangle_{\theta^{(x)}}$ is made for the variational state $\hat{\mathcal{P}}^{(\eta)}|\psi(\theta)\rangle$ against the bare variational state $|\psi(\theta)\rangle$, as in the case of $D = 1$ in Fig. 12(c), even though the ground-state energy is indeed improved. This is consistent with the moderate improvement of the ground-state fidelity for $\hat{\mathcal{P}}^{(\eta)}|\psi(\theta)\rangle$. As shown in Fig. 14(d), $\langle \hat{\eta}^2 \rangle_{\theta^{(x)}}$ converges essentially to zero for all the variational states even without containing the η -symmetry projection $\hat{\mathcal{P}}^{(\eta)}$. The spatial-symmetry-projected state $\hat{\mathcal{P}}^{(\alpha)}|\psi(\theta)\rangle$ is the best among the variational states with a single projection operator, while the variational state with the spatial-symmetry and the spin-symmetry projections, $\hat{\mathcal{P}}^{(S)}\hat{\mathcal{P}}^{(\alpha)}|\psi(\theta)\rangle$, is the best among those with double projection operators.

Figure 15 shows the same results as in Fig. 14 but with the subspace dimension $d_{\mathcal{U}} = 2$. Here, the initial variational parameters are set to be the optimal values obtained

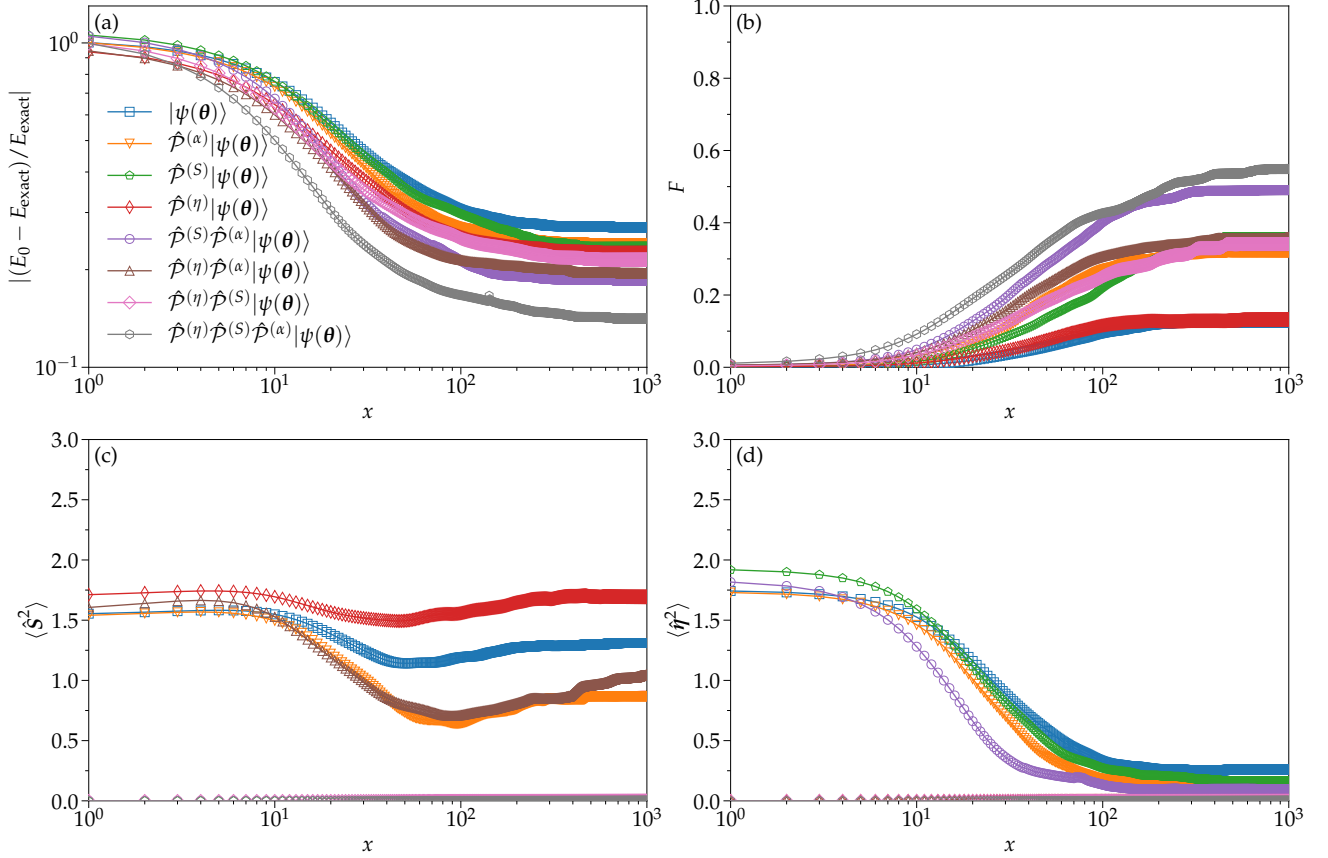


FIG. 12. (a) The ground-state energy $E_0(\theta^{(x)})$, (b) the ground-state fidelity $F(\theta^{(x)})$, (c) the expectation value of total spin squared $\langle \hat{S}^2 \rangle_{\theta^{(x)}}$, and (d) the expectation value of total η squared $\langle \hat{\eta}^2 \rangle_{\theta^{(x)}}$ as a function of optimization iteration x with various combinations of projection operators in $|\Psi_{\mathcal{U}}(\theta)\rangle$ for the Fermi-Hubbard model on a 4×2 cluster with open boundary conditions at $U_{\text{H}}/J = 4$. E_{exact} in (a) is the exact ground-state energy. The quantum circuit of depth $D = 1$ is used for $|\psi(\theta)\rangle$ and hence the number N_v of variational parameters is 28. The dimension of the Krylov subspace is $d_{\mathcal{U}} = 1$. Each result for various combinations of projection operators in $|\Psi_{\mathcal{U}}(\theta)\rangle$ is averaged over 64 independent calculations started with 64 different sets of random initial parameters $\theta^{(1)}$, which are common to all calculations.

with $d_{\mathcal{U}} = 1$ and $D = 2$ in Fig. 14. As in the case with $D = 1$, the ground-state energy and the ground-state fidelity are substantially improved over the results for $d_{\mathcal{U}} = 1$ and $D = 2$ shown in Fig. 14. The most remarkable improvement is indeed achieved when the Krylov subspace is expanded without further optimizing the variational parameters. These quantities are systematically improved by further optimizing the variational parameters. As expected, the best variational state is the one with full projected operators, i.e., $\hat{\mathcal{P}}^{(\eta)}\hat{\mathcal{P}}^{(S)}\hat{\mathcal{P}}^{(\alpha)}|\psi(\theta)\rangle$, which exhibits, for example, the ground-state fidelity as large as 0.9962. The competitive second best is the variational state with the spatial-symmetry and spin-symmetry projections, i.e., $\hat{\mathcal{P}}^{(S)}\hat{\mathcal{P}}^{(\alpha)}|\psi(\theta)\rangle$. We should also emphasize that the bare variational state $|\psi(\theta)\rangle$ without any projection operators and the variational state with containing only the η symmetry projection, $\hat{\mathcal{P}}^{(\eta)}|\psi(\theta)\rangle$, are particularly not satisfactory in terms of the ground-state energy and fidelity as well as $\langle \hat{S}^2 \rangle_{\theta^{(x)}}$. Our numerical results thus clearly demonstrate that the variational states can be improved by imposing the Hamiltonian symmetry on the states without increasing the number of variational parameters.

VIII. CONCLUSION AND DISCUSSION

To conclude, we have proposed a QSE-based VQE scheme that allows us to restore the Hamiltonian symmetry of the variational ground state in a Krylov subspace generated by the Hamiltonian and a symmetry-projected state. We have described a systematic way to implement the spatial symmetry operations for fermions with the fermionic-SWAP gates, and we have also shown how to implement the spin and η rotations required for the spin- and η -symmetry projections, assuming a fermion-to-qubit mapping with the Jordan-Wigner transformation. Moreover, we have generalized the NGD method for the parameter optimization in a QSE-based VQE scheme. We have numerically demonstrated the proposed method for the two-component Fermi-Hubbard model on the 4×2 cluster, and we have found that the symmetry projections onto the appropriate symmetry sector improve substantially the accuracy of the ground state, which is further improved by extending the

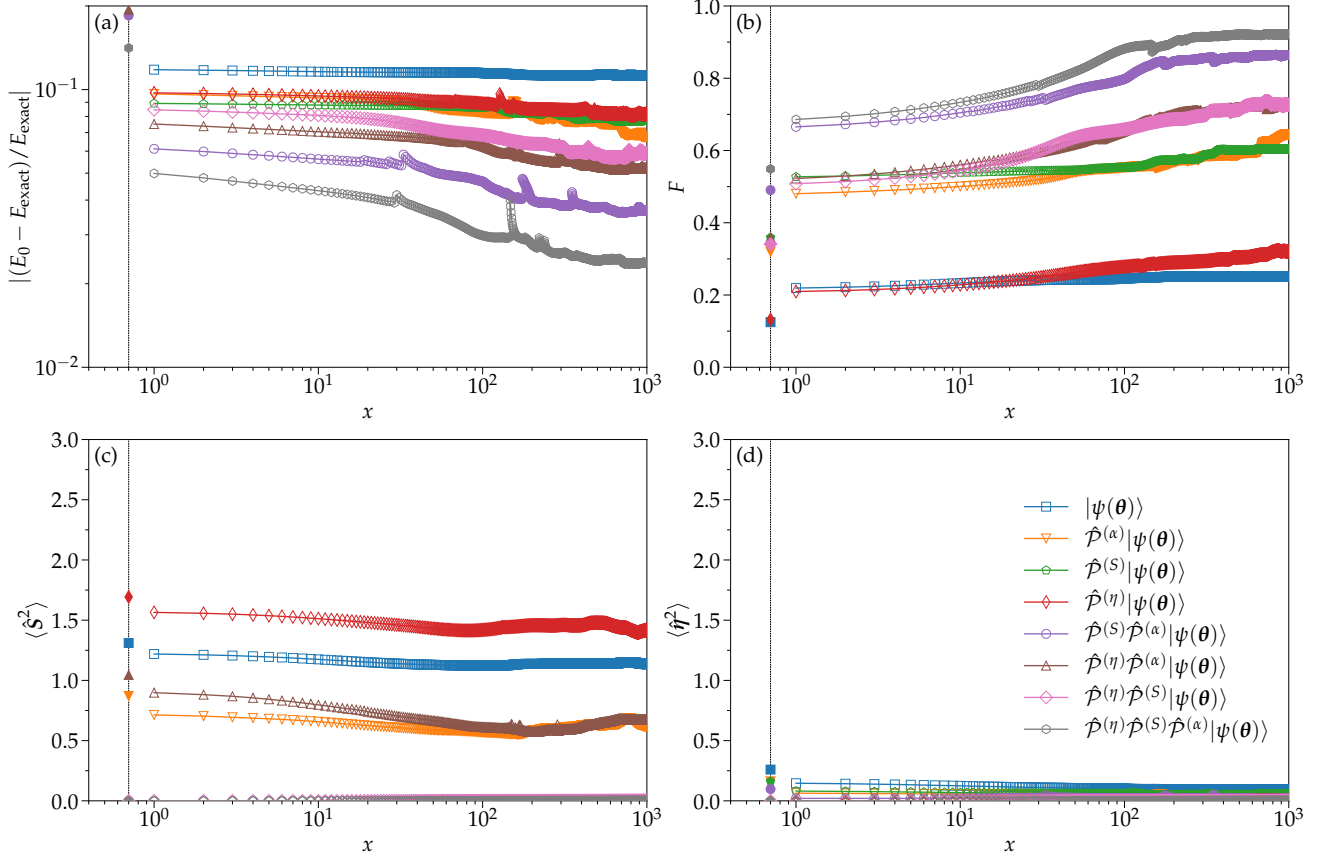


FIG. 13. Same as Fig. 12 but with the Krylov-subspace dimension $d_{\mathcal{U}} = 2$. The 64 different sets of optimized variational parameters $\theta^{(x)}$ at the last optimization iteration $x = 10^3$ obtained for each variational state with $d_{\mathcal{U}} = 1$ in Fig. 12 are used as the initial sets of variational parameters $\theta^{(1)}$ for the corresponding variational states here. For comparison, the results obtained at the last optimization iteration $x = 10^3$ in Fig. 12 are also plotted by solid symbols at $x = 0.7$. The spiky behavior is occasionally observed in the ground state energy $E_0(\theta^{(x)})$ during the parameter optimization iteration. This occurs for particular sets of calculations when the learning rate λ in Eq. (14) is too large to guarantee the monotonic decrease of $E_0(\theta^{(x)})$ with the optimization iteration x (for more details, see Appendix A 2).

Krylov-subspace dimension without increasing the number of variational parameters in the parametrized quantum circuit.

The proposed method is variational and can be regarded as an extension of the SAVQE scheme and the Krylov-subspace diagonalization method. This is because the proposed method is improved (i) from the SAVQE scheme by increasing the subspace dimension $d_{\mathcal{U}}$ without increasing the number of variational parameters, and (ii) from the Krylov-subspace diagonalization method by optimizing the variational parameters θ , but without increasing the subspace dimension $d_{\mathcal{U}}$. The improvement (i) requires more quantum resources than the VQE method, while the improvement (ii) requires more classical resources than the Krylov-subspace diagonalization method with the QPM [42]. Therefore, the proposed method allows us to flexibly choose how to use quantum and classical resources to improve the results, depending on the performance of available quantum and classical computers.

Finally, we make a few remarks on the η symmetry, which might not be as familiar as the spatial and spin symmetry. Recently, the η symmetry or the η -pairing state, which was originally introduced Yang [73] and was subsequently

used to solve the one-dimensional Fermi-Hubbard model analytically [108], attracted renewed interest in the context of photo excitations [78, 109–111], scar states [112, 113], and a nonequilibrium steady state [114] in quantum many-body systems. The η symmetry also exists in other systems such as Kondo-lattice systems [115, 116] and spin-orbit-coupled systems [79, 113] under certain constraints of the Hamiltonian. Moreover, N -particle generalizations of the η -pairing states as eigenstates of an extended $SU(N)$ Fermi-Hubbard model have been reported [117]. Therefore, the η symmetry and in particular its symmetry projection can also help to prepare the ground states of these quantum many-body systems on a quantum computer.

ACKNOWLEDGMENTS

The authors would like to thank Tomonori Shirakawa for helpful comments. A part of the numerical simulations has been done using the HOKUSAI supercomputer at RIKEN (Project ID: Q21532) and also supercomputer Fugaku in-

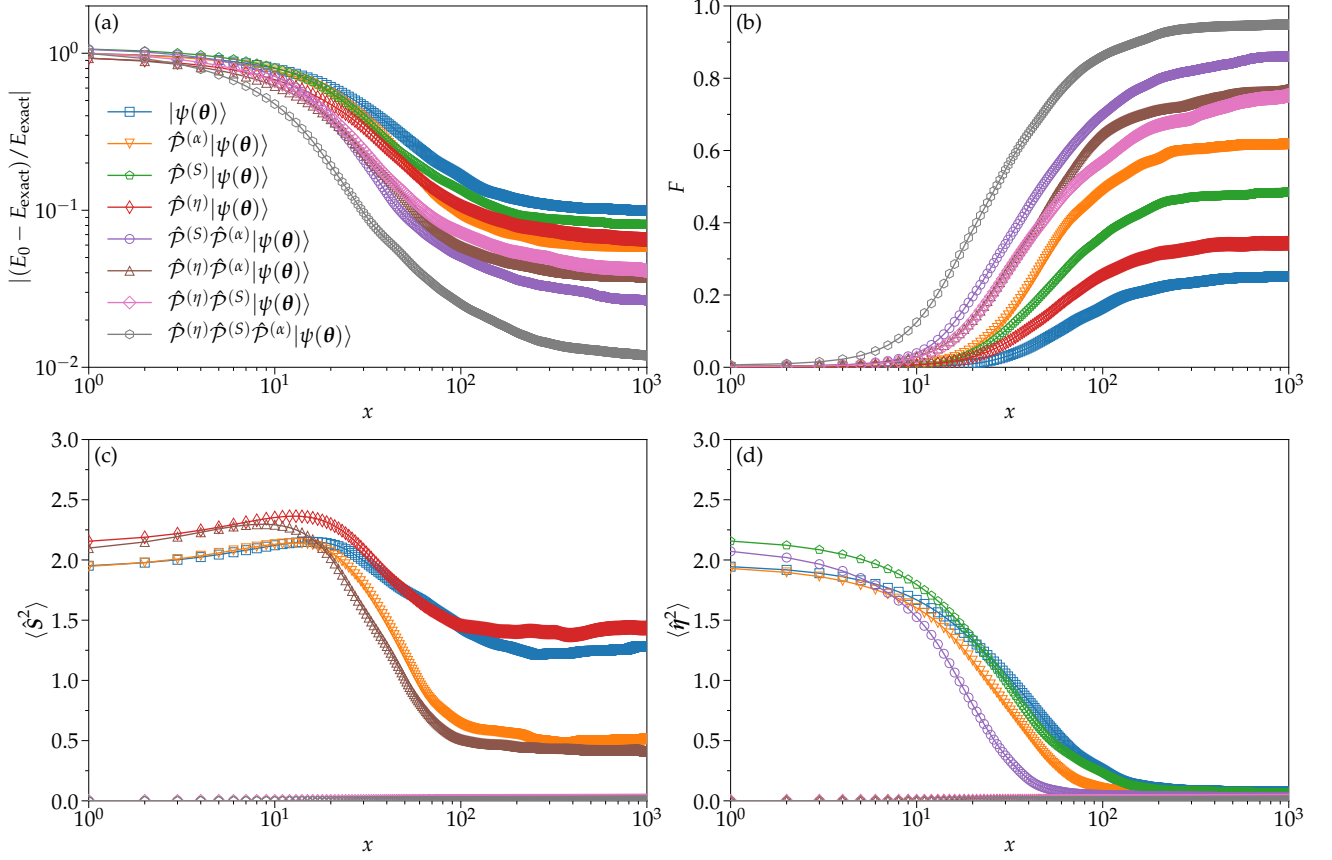


FIG. 14. Same as Fig. 12 but with the quantum circuit of depth $D = 2$ and hence the number N_v of variational parameters is 56.

stalled in RIKEN R-CCS. This work is supported by Grant-in-Aid for Research Activity start-up (No. JP19K23433), Grant-in-Aid for Scientific Research (B) (No. JP18H01183), and Grant-in-Aid for Scientific Research (A) (No. JP21H04446) from MEXT, Japan. This work is also supported in part by the COE research grant in computational science from Hyogo Prefecture and Kobe City through the Foundation for Computational Science.

Appendix A: Details on the natural-gradient-descent method

We provide additional details on the NGD method. We first review how the Fubini-Study metric tensor $\mathbf{G}(\theta)$ in Eq. (16) arises. Then we derive the NGD iteration for the energy optimization in Eq. (14). Finally, we show the positive semidefiniteness of the matrices related to $\mathbf{G}(\theta)$.

1. Fubini-Study metric

Consider a state $|\Psi\rangle$ and its differentiation $|d\Psi\rangle$. The projection of $|d\Psi\rangle$ orthogonal to $|\Psi\rangle$ is given by

$$|d\Psi_{\perp}\rangle \equiv |d\Psi\rangle - |\Psi\rangle\langle\Psi|d\Psi\rangle, \quad (\text{A1})$$

assuming that $\langle\Psi|\Psi\rangle = 1$. In terms of $|d\Psi_{\perp}\rangle$, the Fubini-Study metric [118], denoted as ds^2 , can be written as [119]

$$ds^2 \equiv \langle d\Psi_{\perp}|d\Psi_{\perp}\rangle = \langle d\Psi|d\Psi\rangle - \langle d\Psi|\Psi\rangle\langle\Psi|d\Psi\rangle. \quad (\text{A2})$$

Assume that $|\Psi\rangle$ is parametrized with real variational parameters $\theta = \{\theta_k\}_{k=1}^{N_v}$. By expanding $|d\Psi\rangle$ with respect to $d\theta$, we obtain that

$$ds^2 = \sum_{k=1}^{N_v} \sum_{l=1}^{N_v} G_{kl}(\theta) d\theta_k d\theta_l = d\theta^T \mathbf{G}(\theta) d\theta, \quad (\text{A3})$$

where $d\theta^T = [d\theta_1 \ d\theta_2 \ \dots \ d\theta_{N_v}]$ and

$$G_{kl}(\theta) = \text{Re}\langle\partial_k\Psi(\theta)|\partial_l\Psi(\theta)\rangle - \langle\partial_k\Psi(\theta)|\Psi(\theta)\rangle\langle\Psi(\theta)|\partial_l\Psi(\theta)\rangle, \quad (\text{A4})$$

indicating that $\mathbf{G}(\theta)$ defines the Fubini-Study metric in the variational-parameter space.

2. Natural-gradient-descent iteration

To minimize the variational energy $E_0(\theta)$, one may wish to find a direction $\delta\theta$ in the variational-parameter space along which the energy $E_0(\theta + \delta\theta)$ is most decreased, when the parameters are displaced by a given constant distance, e.g.,

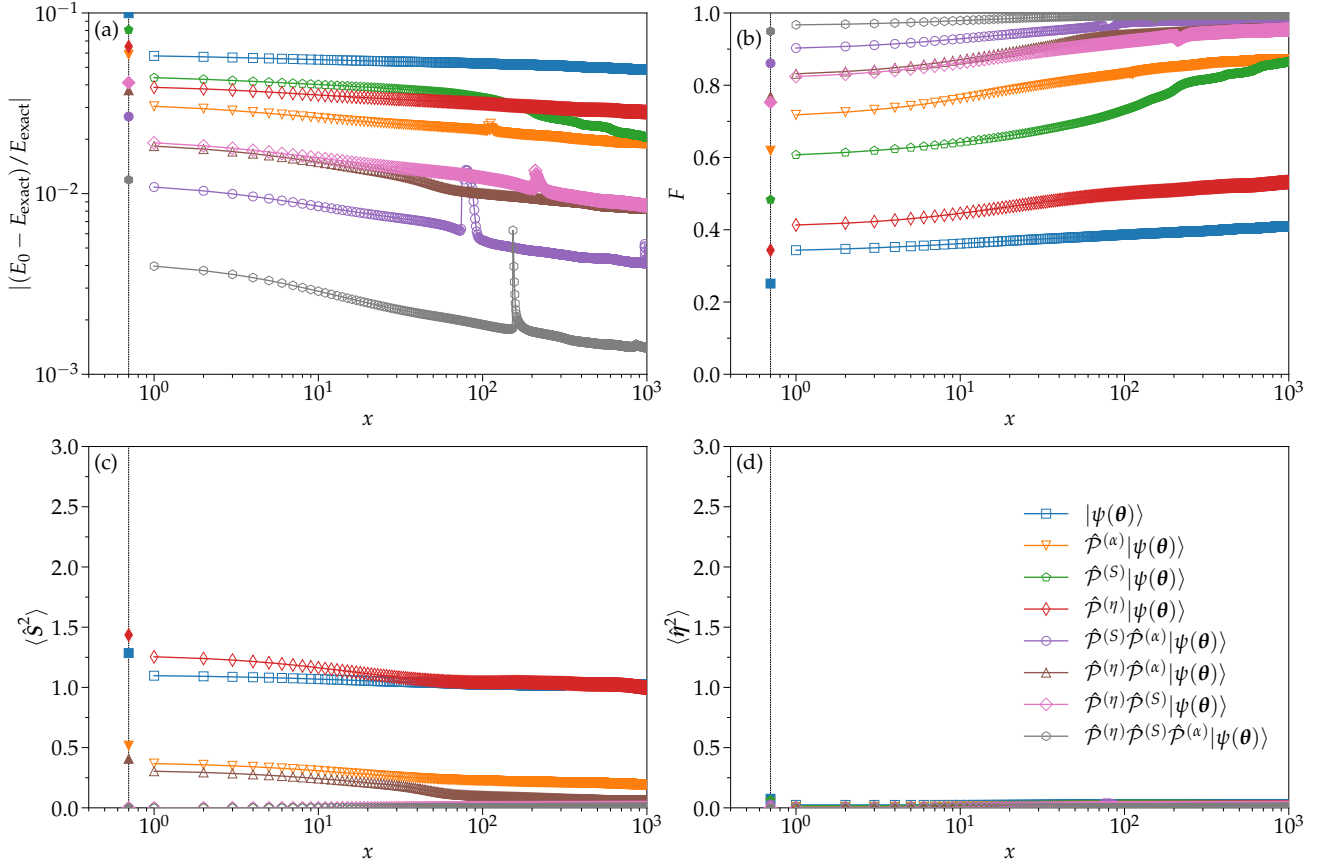


FIG. 15. Same as Fig. 14 but with the Krylov-subspace dimension $d_u = 2$. The 64 different sets of optimized variational parameters $\theta^{(x)}$ at the last optimization iteration $x = 10^3$ obtained for each variational state with $d_u = 1$ in Fig. 14 are used as the initial sets of variational parameters $\theta^{(1)}$ for the corresponding variational states here. For comparison, the results obtained at the last optimization iteration $x = 10^3$ in Fig. 14 are also plotted by solid symbols at $x = 0.7$. The spiky behavior is occasionally observed in the ground state energy $E_0(\theta^{(x)})$ during the parameter optimization iteration. This is due to the same reason described in the caption of Fig. 13.

$\|\delta\theta\| = d$. Here, $\|\delta\theta\|$ is the distance in the neighborhood of θ defined by $\|\delta\theta\|^2 = \delta\theta^T \mathbf{G}(\theta) \delta\theta$. Such a direction $\delta\theta$ can be found by minimizing the function

$$f(\theta, \delta\theta) = E_0(\theta + \delta\theta) + \frac{\lambda}{2} (\delta\theta^T \mathbf{G}(\theta) \delta\theta - d^2) \quad (\text{A5})$$

with respect to $\delta\theta$, where λ is a Lagrange multiplier for the equidistant constraint [54, 120]. By substituting the linear approximation of the energy $E_0(\theta + \delta\theta) \approx E_0(\theta) + \nabla E_0(\theta)^T \delta\theta$ to Eq. (A5), the steepest direction $\delta\theta^*$ such that $\nabla_{\delta\theta} f(\theta, \delta\theta)|_{\delta\theta=\delta\theta^*} = 0$ is obtained as

$$\delta\theta^* = -\frac{1}{\lambda} [\mathbf{G}(\theta)]^{-1} \nabla E_0(\theta). \quad (\text{A6})$$

By discretizing Eq. (A6) as $\delta\theta^* \rightarrow \theta^{(x+1)} - \theta^{(x)}$ and $\theta \rightarrow \theta^{(x)}$ and denoting $\tau = 1/\lambda$, we obtain Eq. (14). Although τ can be chosen adaptively depending on x , the value of τ is fixed throughout the variational-parameter optimization in the numerical simulations shown in Sec. VII C and Appendix F.

From Eq. (14), the change in energy per iteration,

$\delta E_0(\theta^{(x)}) = E_0(\theta^{(x+1)}) - E_0(\theta^{(x)})$, can be approximated as

$$\delta E_0(\theta^{(x)}) \approx \nabla E_0(\theta^{(x)})^T \delta\theta^{(x)} = -\tau \nabla E_0(\theta^{(x)})^T [\mathbf{G}(\theta^{(x)})]^{-1} \nabla E_0(\theta^{(x)}), \quad (\text{A7})$$

$$= -\frac{1}{\tau} \delta\theta^{(x)T} \mathbf{G}(\theta^{(x)}) \delta\theta^{(x)}, \quad (\text{A8})$$

where $\delta\theta^{(x)} = \theta^{(x+1)} - \theta^{(x)}$. Since $\mathbf{G}(\theta^{(x)})$ is positive semidefinite, the quadratic forms in the last lines are greater than or equal to zero. Therefore, if τ is chosen positive and not too large so that the above approximation holds, the energy is guaranteed to decrease after every iteration, i.e., $E_0(\theta^{(x+1)}) \leq E_0(\theta^{(x)})$. In our numerical simulations in Figs. 13(a), 15(a), and 19(a), an abrupt increase of $E_0(\theta^{(x)})$ occasionally occurs. This is because for particular sets of calculations, the value of λ set during the optimization iteration is too large to satisfy the condition assumed above.

We note that if the energy in Eq. (A5) is expanded up to the second order in $\delta\theta$ as $E_0(\theta + \delta\theta) \approx E_0(\theta) + \nabla E_0(\theta)^T \delta\theta + \frac{1}{2} \delta\theta^T \mathbf{h}(\theta) \delta\theta$, where $\mathbf{h}(\theta)$ is the Hessian, Eq. (A6) is replaced with

$$\delta\theta^* = -[\lambda \mathbf{G}(\theta) + \mathbf{h}(\theta)]^{-1} \nabla E_0(\theta). \quad (\text{A9})$$

Equation (A9) leads to a Levenberg-Marquardt-type method, and reduces to the Newton method if $\lambda = 0$. Note that the Hessian $\mathbf{h}(\boldsymbol{\theta})$ is not positive semidefinite in general.

3. Positive semidefinite matrices

Although we already know that the Fubini-Study metric tensor $\mathbf{G}(\boldsymbol{\theta})$ is positive semidefinite by definition [see Eq. (A3)], it is instructive to explore some inequalities for $\mathbf{G}(\boldsymbol{\theta})$. First, it is convenient to define a $\mathcal{D} \times N_v$ Jacobian matrix $\mathcal{J}(\boldsymbol{\theta})$ with its component

$$\mathcal{J}_{mk}(\boldsymbol{\theta}) \equiv \frac{\partial \Psi_m(\boldsymbol{\theta})}{\partial \theta_k}, \quad (\text{A10})$$

where $\langle e_m | \Psi(\boldsymbol{\theta}) \rangle = \Psi_m(\boldsymbol{\theta})$ with $\{|e_m\rangle\}_{m=1}^{\mathcal{D}}$ being an arbitrary complete orthonormal set, and hence $\langle \Psi(\boldsymbol{\theta}) | \Psi(\boldsymbol{\theta}) \rangle = \sum_{m=1}^{\mathcal{D}} |\Psi_m(\boldsymbol{\theta})|^2 = 1$. Inserting the resolution of the identity $1 = \sum_{m=1}^{\mathcal{D}} |e_m\rangle \langle e_m|$ into Eqs. (17) and (18) yields

$$\gamma_{kl}(\boldsymbol{\theta}) = \sum_{m=1}^{\mathcal{D}} \mathcal{J}_{mk}^*(\boldsymbol{\theta}) \mathcal{J}_{ml}(\boldsymbol{\theta}) \quad (\text{A11})$$

and

$$\beta_k^*(\boldsymbol{\theta}) = \sum_{m=1}^{\mathcal{D}} \mathcal{J}_{mk}^*(\boldsymbol{\theta}) \Psi_m(\boldsymbol{\theta}). \quad (\text{A12})$$

Equation (A11) implies that $\boldsymbol{\gamma}(\boldsymbol{\theta}) = \mathcal{J}^\dagger(\boldsymbol{\theta}) \mathcal{J}(\boldsymbol{\theta})$ is a Gram matrix and hence positive semidefinite, i.e., $\boldsymbol{\gamma}(\boldsymbol{\theta}) \geq 0$.

We then consider a real matrix $[\mathbf{B}(\boldsymbol{\theta})]_{kl} \equiv \beta_k^*(\boldsymbol{\theta}) \beta_l(\boldsymbol{\theta})$, which is also a Gram matrix and positive semidefinite, i.e., $\mathbf{B}(\boldsymbol{\theta}) \geq 0$. For any vector \mathbf{x} , it follows that

$$\begin{aligned} \mathbf{x}^\dagger \mathbf{B}(\boldsymbol{\theta}) \mathbf{x} &= \sum_{k=1}^{N_v} \sum_{l=1}^{N_v} x_k^* \beta_k^*(\boldsymbol{\theta}) \beta_l(\boldsymbol{\theta}) x_l \\ &= \left[\sum_{m=1}^{\mathcal{D}} \left(\sum_{k=1}^{N_v} \mathcal{J}_{mk}(\boldsymbol{\theta}) x_k \right)^* \Psi_m(\boldsymbol{\theta}) \right] \left[\sum_{n=1}^{\mathcal{D}} \left(\sum_{l=1}^{N_v} \mathcal{J}_{nl}(\boldsymbol{\theta}) x_l \right) \Psi_n^*(\boldsymbol{\theta}) \right] \\ &\leq \sum_{m=1}^{\mathcal{D}} \left| \sum_{k=1}^{N_v} \mathcal{J}_{mk}(\boldsymbol{\theta}) x_k \right|^2 \sum_{n=1}^{\mathcal{D}} |\Psi_n(\boldsymbol{\theta})|^2 = \mathbf{x}^\dagger \boldsymbol{\gamma}(\boldsymbol{\theta}) \mathbf{x}, \end{aligned} \quad (\text{A13})$$

where the Cauchy-Schwarz inequality is used to obtain the third line and $\sum_{n=1}^{\mathcal{D}} |\Psi_n(\boldsymbol{\theta})|^2 = 1$ is used for the last equality. We thus have shown that $\boldsymbol{\gamma}(\boldsymbol{\theta}) \geq \mathbf{B}(\boldsymbol{\theta})$, implying that for any nonzero real vector \mathbf{y} , $\mathbf{y}^T \mathbf{G}(\boldsymbol{\theta}) \mathbf{y} = \mathbf{y}^T \text{Re}[\boldsymbol{\gamma}(\boldsymbol{\theta}) - \mathbf{B}(\boldsymbol{\theta})] \mathbf{y} = \mathbf{y}^T (\boldsymbol{\gamma}(\boldsymbol{\theta}) - \mathbf{B}(\boldsymbol{\theta})) \mathbf{y} \geq 0$, which thus confirms the positive semidefiniteness of $\mathbf{G}(\boldsymbol{\theta})$. In summary, we have $\text{Re} \boldsymbol{\gamma}(\boldsymbol{\theta}) \geq \mathbf{G}(\boldsymbol{\theta}) \geq 0$ and hence $0 \leq [\text{Re} \boldsymbol{\gamma}(\boldsymbol{\theta})]^{-1} \leq \mathbf{G}^{-1}(\boldsymbol{\theta})$ [121]. Note that $\mathbf{G}(\boldsymbol{\theta})$ is induced by $\langle d\Psi_\perp | d\Psi_\perp \rangle$ as in Eqs. (A2)-(A4) and similarly $\text{Re} \boldsymbol{\gamma}(\boldsymbol{\theta})$ can be induced by $\langle d\Psi | d\Psi \rangle$.

Appendix B: Fermionic symmetry operations

1. Symmetry operation onto a fermionic state

We briefly review how the symmetry operator \hat{g}_m acts on a fermion occupation basis state. Let \hat{c}_i (\hat{c}_i^\dagger) be a fermion

annihilation (creation) operator of a single-particle state labeled as i ($= 1, 2, 3, \dots$). The fermion operators satisfy the anticommutation relations $\{\hat{c}_i, \hat{c}_j^\dagger\} \equiv \hat{c}_i \hat{c}_j^\dagger + \hat{c}_j^\dagger \hat{c}_i = \delta_{ij}$ and $\{\hat{c}_i, \hat{c}_j\} = \{\hat{c}_i^\dagger, \hat{c}_j^\dagger\} = 0$. Let $|0\rangle_F$ be the fermion vacuum that is annihilated by any fermionic annihilation operator

$$\hat{c}_i |0\rangle_F = 0 \quad (\text{for any } i), \quad (\text{B1})$$

and is invariant under any symmetry operation

$$\hat{g}_m |0\rangle_F = |0\rangle_F \quad (\text{for any } m). \quad (\text{B2})$$

Then, an occupation-basis state $|b\rangle_F$ with N_F number of fermions in an occupation basis can be written as

$$|b\rangle_F \equiv \underbrace{\hat{c}_k^\dagger \cdots \hat{c}_j^\dagger \cdots \hat{c}_i^\dagger}_{N_F \text{ operators}} |0\rangle_F, \quad (\text{B3})$$

where b in $|b\rangle_F$ denotes a bit string of length N , explicitly defined in Eq. (94). As a convention for the basis states, one may choose that the indexes are, e.g., in the descending order $k > \dots > j > \dots > i$ from left to right in Eq. (B3). Note that N_F corresponds to the number of nonzero b_i 's in Eq. (94), i.e., $N_F = \sum_{i=1}^N b_i$.

Suppose that \hat{g}_m transforms the creation operator \hat{c}_i^\dagger as

$$\hat{g}_m \hat{c}_i^\dagger \hat{g}_m^{-1} = \hat{c}_{m(i)}^\dagger \quad (\text{for any } i), \quad (\text{B4})$$

or equivalently $\hat{g}_m \hat{c}_i^\dagger = \hat{c}_{m(i)}^\dagger \hat{g}_m$. Then, applying the symmetry operation \hat{g}_m on the state $|b\rangle_F$ in Eq. (B3) yields

$$\begin{aligned} \hat{g}_m |b\rangle_F &= \hat{g}_m (\hat{c}_k^\dagger \cdots \hat{c}_j^\dagger \cdots \hat{c}_i^\dagger |0\rangle_F) \\ &= (\hat{g}_m \hat{c}_k^\dagger \hat{g}_m^{-1}) \cdots (\hat{g}_m \hat{c}_j^\dagger \hat{g}_m^{-1}) \cdots (\hat{g}_m \hat{c}_i^\dagger \hat{g}_m^{-1}) \hat{g}_m |0\rangle_F \\ &= \hat{c}_{m(k)}^\dagger \cdots \hat{c}_{m(j)}^\dagger \cdots \hat{c}_{m(i)}^\dagger |0\rangle_F, \end{aligned} \quad (\text{B5})$$

where Eqs. (B2) and (B4) are used in the third equality. In general, the indexes $m(k), \dots, m(j), \dots, m(i)$ in Eq. (B5) do not match the convention for the basis states (i.e., they are not in the descending order). To associate $\hat{g}_m |b\rangle_F$ with a basis state $|b'\rangle_F$, one has to reorder the fermion creation operators $\hat{c}_{m(k)}^\dagger \cdots \hat{c}_{m(j)}^\dagger \cdots \hat{c}_{m(i)}^\dagger$ to match the convention for the occupation-basis states:

$$\begin{aligned} \hat{g}_m |b\rangle_F &= \hat{c}_{m(k)}^\dagger \cdots \hat{c}_{m(j)}^\dagger \cdots \hat{c}_{m(i)}^\dagger |0\rangle_F \\ &= \text{sgn}(\mathcal{R}) \hat{c}_{k'}^\dagger \cdots \hat{c}_{j'}^\dagger \cdots \hat{c}_{i'}^\dagger |0\rangle_F \\ &\equiv \text{sgn}(\mathcal{R}) |b'\rangle_F \end{aligned} \quad (\text{B6})$$

where \mathcal{R} denotes the permutation

$$\mathcal{R} \equiv \underbrace{\begin{pmatrix} m(k) & \cdots & m(j) & \cdots & m(i) \\ k' & \cdots & j' & \cdots & i' \end{pmatrix}}_{N_F \text{ columns}} \quad (\text{B7})$$

with $k' > \dots > j' > \dots > i'$, and $\text{sgn}(\mathcal{R}) = +1$ (-1) if \mathcal{R} is an even (odd) permutation. The sign factor $\text{sgn}(\mathcal{R})$ arises because of the anticommutation relation for fermion creation operators.

2. Symmetry operator as a product of fermionic-SWAP gates

To implement \hat{g}_m on a quantum circuit, a concrete expression of \hat{g}_m is required. To this end, we use the fermionic-SWAP operator [90–95]

$$\hat{\mathcal{F}}_{ij} \equiv \hat{1} + (\hat{c}_i^\dagger \hat{c}_j + \text{H.c.}) - \hat{c}_i^\dagger \hat{c}_i - \hat{c}_j^\dagger \hat{c}_j. \quad (\text{B8})$$

It readily follows from Eq. (B8) that $\hat{\mathcal{F}}_{ji} = \hat{\mathcal{F}}_{ij} = \hat{\mathcal{F}}_{ij}^\dagger = \hat{\mathcal{F}}_{ij}^{-1}$ and $\hat{\mathcal{F}}_{ii} = \hat{1}$. $\hat{\mathcal{F}}_{ij}$ also satisfies the following relations:

$$\hat{\mathcal{F}}_{ij}|0\rangle_{\text{F}} = |0\rangle_{\text{F}} \quad (\text{B9})$$

and

$$\hat{\mathcal{F}}_{ij} \hat{c}_i^\dagger \hat{\mathcal{F}}_{ij}^{-1} = \hat{c}_j^\dagger, \quad (\text{B10})$$

or equivalently $\hat{\mathcal{F}}_{ij} \hat{c}_i^\dagger = \hat{c}_j^\dagger \hat{\mathcal{F}}_{ij}$, which are analogous to Eqs. (B2) and (B4). Moreover, it can be easily shown that $[\hat{\mathcal{F}}_{ij}, \hat{c}_k^\dagger] = 0$ for $i \neq k$ and $j \neq k$, and $[\hat{\mathcal{F}}_{ij}, \hat{\mathcal{F}}_{kl}] = 0$ for $\{i, j\} \neq \{k, l\}$. Now one can confirm that $\hat{\mathcal{F}}_{i\delta(i)}$ satisfies Eqs. (99)-(102). For example, Eq. (102) can be confirmed as follows:

$$\begin{aligned} & \hat{\mathcal{F}}_{j\delta(j)} (\hat{c}_k^\dagger \cdots \hat{c}_j^\dagger \hat{c}_{\delta(j)}^\dagger \cdots \hat{c}_i^\dagger |0\rangle_{\text{F}}) \\ &= \hat{c}_k^\dagger \cdots (\hat{\mathcal{F}}_{j\delta(j)} \hat{c}_j^\dagger \hat{\mathcal{F}}_{j\delta(j)}^{-1}) (\hat{\mathcal{F}}_{j\delta(j)} \hat{c}_{\delta(j)}^\dagger \hat{\mathcal{F}}_{j\delta(j)}^{-1}) \cdots \hat{c}_i^\dagger \hat{\mathcal{F}}_{j\delta(j)} |0\rangle_{\text{F}} \\ &= \hat{c}_k^\dagger \cdots \hat{c}_{\delta(j)}^\dagger \hat{c}_j^\dagger \cdots \hat{c}_i^\dagger |0\rangle_{\text{F}} \\ &= -\hat{c}_k^\dagger \cdots \hat{c}_j^\dagger \hat{c}_{\delta(j)}^\dagger \cdots \hat{c}_i^\dagger |0\rangle_{\text{F}}, \end{aligned} \quad (\text{B11})$$

From the above properties of $\hat{\mathcal{F}}_{ij}$, it is now obvious that \hat{g}_m for fermions can be obtained by replacing the SWAP operators $\hat{S}_{i\delta(i)}$ in Eq. (86) with the fermionic-SWAP operators $\hat{\mathcal{F}}_{i\delta(i)}$ as in Eq. (93).

Appendix C: Two-qubit unitary circuits

In this appendix, we discuss quantum circuits and their matrix representations for typical two-qubit two-level unitaries that appear in quantum computations of quantum many-body systems.

1. Two-qubit two-level unitaries

Let \hat{u} be a one-qubit unitary operator such that

$$\hat{u} \doteq \begin{bmatrix} u_{11} & u_{12} \\ u_{21} & u_{22} \end{bmatrix}, \quad (\text{C1})$$

where the matrix representation is for the basis states $|0\rangle$ and $|1\rangle$ in the computational basis. Assuming the basis states $|0\rangle_i |0\rangle_j$, $|0\rangle_i |1\rangle_j$, $|1\rangle_i |0\rangle_j$, and $|1\rangle_i |1\rangle_j$ for the i th and j th qubits (hereafter we assume $i \neq j$), the matrix representation of

the controlled- u gate is then given by a block-diagonal matrix with nontrivial 2×2 entries in the lower-right part [122], as shown in Fig. 16(a). By permuting the basis states with CNOT, SWAP, and X gates, one can complete the quantum circuits for the two-qubit two-level unitaries [103], as shown in Figs. 16(b)-16(f).

2. Normal quadratic terms of fermion operators

Consider the following general quadratic form of fermion operators that conserves the number of fermions (i.e., normal term):

$$\begin{aligned} \hat{h}_{ij}^{(n)} &= \begin{bmatrix} \hat{c}_i^\dagger & \hat{c}_j^\dagger \\ b^* & -a \end{bmatrix} \begin{bmatrix} \hat{c}_i \\ \hat{c}_j \end{bmatrix} \\ &= \text{Re}b (\hat{c}_i^\dagger \hat{c}_j + \hat{c}_j^\dagger \hat{c}_i) + i \text{Im}b (\hat{c}_i^\dagger \hat{c}_j - \hat{c}_j^\dagger \hat{c}_i) + a (\hat{n}_i - \hat{n}_j) \quad (\text{C2}) \\ &= \hat{h}_{ij}^{(n,1)} + \hat{h}_{ij}^{(n,2)} + \hat{h}_{ij}^{(n,3)}, \\ &\stackrel{\text{JWT}}{=} \frac{\text{Re}b}{2} (\hat{X}_i \hat{X}_j + \hat{Y}_i \hat{Y}_j) \hat{Z}_{\text{JW},ij} - \frac{\text{Im}b}{2} (\hat{X}_i \hat{Y}_j - \hat{Y}_i \hat{X}_j) \hat{Z}_{\text{JW},ij} \\ &\quad + \frac{a}{2} (\hat{Z}_j - \hat{Z}_i), \end{aligned} \quad (\text{C3})$$

where a and b are real and complex numbers, respectively, such that $a^2 + |b|^2 = 1$, and hence the 2×2 matrix is traceless, unitary, and Hermitian. The 2×2 matrix reduces to Pauli X , Y , and Z matrices when $(a, b) = (0, 1)$, $(0, -i)$, and $(1, 0)$, respectively. $\hat{h}_{ij}^{(n,1)}$, $\hat{h}_{ij}^{(n,2)}$, and $\hat{h}_{ij}^{(n,3)}$ correspond to each term in Eq. (C2) and do not commute with each other. We shall now consider the exponentiated $\hat{h}_{ij}^{(n,1)}$, $\hat{h}_{ij}^{(n,2)}$, and $\hat{h}_{ij}^{(n,3)}$, i.e., $e^{-i\theta \hat{h}_{ij}^{(n,1)}/2}$, $e^{-i\theta \hat{h}_{ij}^{(n,2)}/2}$, and $e^{-i\theta \hat{h}_{ij}^{(n,3)}/2}$, and express these two-qubit unitary operators in quantum circuits.

For this purpose, it is useful to notice that

$$(\hat{c}_i^\dagger \hat{c}_j + \hat{c}_j^\dagger \hat{c}_i)^l = \begin{cases} \hat{c}_i^\dagger \hat{c}_j + \hat{c}_j^\dagger \hat{c}_i & \text{for } l \text{ odd,} \\ \hat{n}_i + \hat{n}_j - 2\hat{n}_i \hat{n}_j & \text{for } l \text{ even,} \end{cases} \quad (\text{C4})$$

$$\{-i(\hat{c}_i^\dagger \hat{c}_j - \hat{c}_j^\dagger \hat{c}_i)\}^l = \begin{cases} -i(\hat{c}_i^\dagger \hat{c}_j - \hat{c}_j^\dagger \hat{c}_i) & \text{for } l \text{ odd,} \\ \hat{n}_i + \hat{n}_j - 2\hat{n}_i \hat{n}_j & \text{for } l \text{ even,} \end{cases} \quad (\text{C5})$$

and

$$(\hat{n}_i - \hat{n}_j)^l = \begin{cases} \hat{n}_i - \hat{n}_j & \text{for } l \text{ odd,} \\ \hat{n}_i + \hat{n}_j - 2\hat{n}_i \hat{n}_j & \text{for } l \text{ even,} \end{cases} \quad (\text{C6})$$

where l is positive integer, or equivalently in the qubit representation that

$$\left\{ \frac{1}{2} (\hat{X}_i \hat{X}_j + \hat{Y}_i \hat{Y}_j) \hat{Z}_{\text{JW},ij} \right\}^l = \begin{cases} \frac{1}{2} (\hat{X}_i \hat{X}_j + \hat{Y}_i \hat{Y}_j) \hat{Z}_{\text{JW},ij} & \text{for } l \text{ odd,} \\ \frac{1}{2} (1 - \hat{Z}_i \hat{Z}_j) & \text{for } l \text{ even,} \end{cases} \quad (\text{C7})$$

$$\left\{ \frac{1}{2} (\hat{X}_i \hat{Y}_j - \hat{Y}_i \hat{X}_j) \hat{Z}_{\text{JW},ij} \right\}^l = \begin{cases} \frac{1}{2} (\hat{X}_i \hat{Y}_j - \hat{Y}_i \hat{X}_j) \hat{Z}_{\text{JW},ij} & \text{for } l \text{ odd,} \\ \frac{1}{2} (1 - \hat{Z}_i \hat{Z}_j) & \text{for } l \text{ even,} \end{cases} \quad (\text{C8})$$

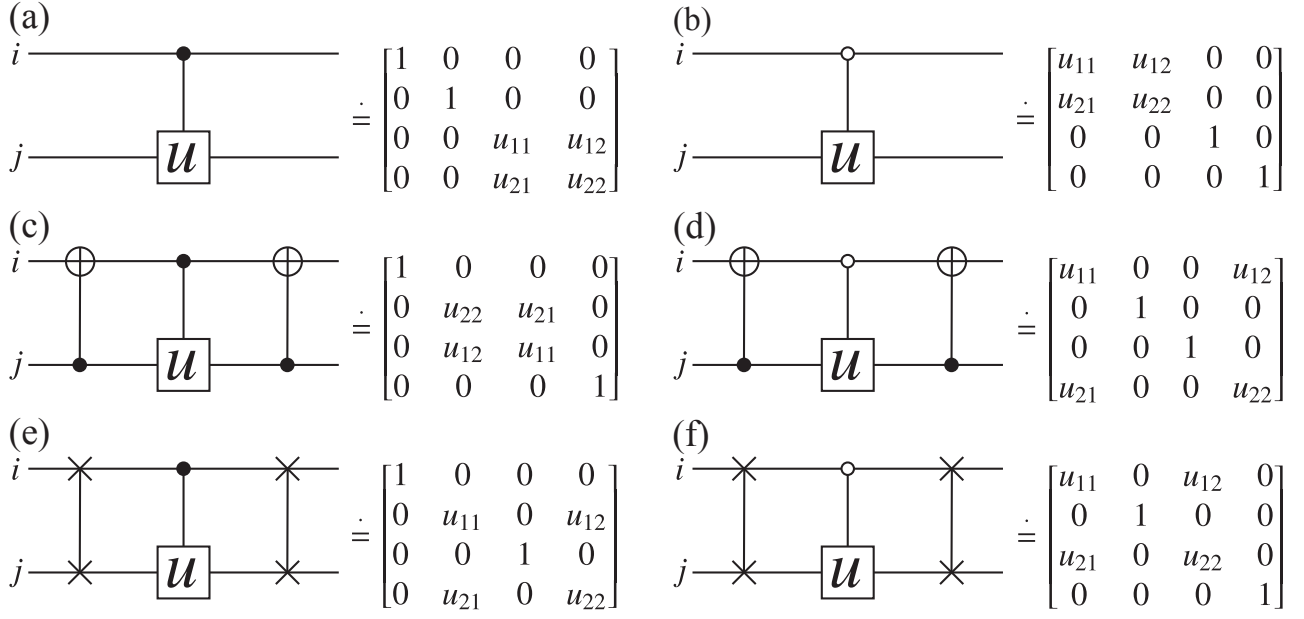


FIG. 16. List of the two-qubit two-level unitaries. The corresponding matrix representations are also shown with the basis states $|0\rangle_i|0\rangle_j$, $|0\rangle_i|1\rangle_j$, $|1\rangle_i|0\rangle_j$, and $|1\rangle_i|1\rangle_j$ for qubits i and j .

and

$$\left\{ \frac{1}{2} (\hat{Z}_j - \hat{Z}_i) \right\}^l = \begin{cases} \frac{1}{2} (\hat{Z}_j - \hat{Z}_i) & \text{for } l \text{ odd,} \\ \frac{1}{2} (1 - \hat{Z}_i \hat{Z}_j) & \text{for } l \text{ even.} \end{cases} \quad (\text{C9})$$

Note that Eqs. (C7) and (C8) also hold when the Jordan-Wigner string $\hat{Z}_{jw,ij}$ is absent in these equations. Let us now consider an operator $\hat{\mathcal{A}}$ that satisfies $\hat{\mathcal{A}}^l = \hat{\mathcal{A}}$ for l odd and $\hat{\mathcal{A}}^l = \hat{\mathcal{B}}$ for l even, as in Eqs. (C4)-(C9). Then, it is easily shown that

$$e^{-i\frac{\theta}{2}\hat{\mathcal{A}}} = 1 + \left(\cos \frac{\theta}{2} - 1 \right) \hat{\mathcal{B}} - i \sin \frac{\theta}{2} \hat{\mathcal{A}}. \quad (\text{C10})$$

Given that the Jordan-Wigner string $\hat{Z}_{jw,ij}$ commutes with the other operators in Eqs. (C7) and (C8), and $\hat{Z}_{jw,ij}^2 = 1$, the matrix representations

$$\frac{1}{2} (\hat{X}_i \hat{X}_j + \hat{Y}_i \hat{Y}_j) \doteq \begin{bmatrix} 0 & 0 & 0 & 0 \\ 0 & 0 & 1 & 0 \\ 0 & 1 & 0 & 0 \\ 0 & 0 & 0 & 0 \end{bmatrix}, \quad (\text{C11})$$

$$\frac{1}{2} (\hat{X}_i \hat{Y}_j - \hat{Y}_i \hat{X}_j) \doteq \begin{bmatrix} 0 & 0 & 0 & 0 \\ 0 & 0 & i & 0 \\ 0 & -i & 0 & 0 \\ 0 & 0 & 0 & 0 \end{bmatrix}, \quad (\text{C12})$$

$$\frac{1}{2} (\hat{Z}_j - \hat{Z}_i) \doteq \begin{bmatrix} 0 & 0 & 0 & 0 \\ 0 & -1 & 0 & 0 \\ 0 & 0 & 1 & 0 \\ 0 & 0 & 0 & 0 \end{bmatrix}, \quad (\text{C13})$$

and

$$\frac{1}{2} (1 - \hat{Z}_i \hat{Z}_j) \doteq \begin{bmatrix} 0 & 0 & 0 & 0 \\ 0 & 1 & 0 & 0 \\ 0 & 0 & 1 & 0 \\ 0 & 0 & 0 & 0 \end{bmatrix} \quad (\text{C14})$$

also confirm Eqs. (C7), (C8), and (C9). Here, the basis states $|0\rangle_i|0\rangle_j$, $|0\rangle_i|1\rangle_j$, $|1\rangle_i|0\rangle_j$, and $|1\rangle_i|1\rangle_j$ for the i th and j th qubits are assumed. Now it is obvious from the matrix representations that the operators in Eqs. (C11)-(C14) act as Pauli X , Y , Z , and identity I operators on the basis states $|1\rangle_i|0\rangle_j$ and $|0\rangle_i|1\rangle_j$ [note the order of these basis states, see also Fig. 16(c)], and as zero on the basis states $|0\rangle_i|0\rangle_j$ and $|1\rangle_i|1\rangle_j$. Therefore, the exponentials of the matrices in Eqs. (C11)-(C13) are given by

$$\exp \left[-i\frac{\theta}{4} (\hat{X}_i \hat{X}_j + \hat{Y}_i \hat{Y}_j) \right] \doteq \begin{bmatrix} 1 & 0 & 0 & 0 \\ 0 & \cos \frac{\theta}{2} & -i \sin \frac{\theta}{2} & 0 \\ 0 & -i \sin \frac{\theta}{2} & \cos \frac{\theta}{2} & 0 \\ 0 & 0 & 0 & 1 \end{bmatrix}, \quad (\text{C15})$$

$$\exp \left[-i\frac{\theta}{4} (\hat{X}_i \hat{Y}_j - \hat{Y}_i \hat{X}_j) \right] \doteq \begin{bmatrix} 1 & 0 & 0 & 0 \\ 0 & \cos \frac{\theta}{2} & \sin \frac{\theta}{2} & 0 \\ 0 & -\sin \frac{\theta}{2} & \cos \frac{\theta}{2} & 0 \\ 0 & 0 & 0 & 1 \end{bmatrix}, \quad (\text{C16})$$

and

$$\exp \left[-i\frac{\theta}{4} (\hat{Z}_j - \hat{Z}_i) \right] \doteq \begin{bmatrix} 1 & 0 & 0 & 0 \\ 0 & e^{i\theta/2} & 0 & 0 \\ 0 & 0 & e^{-i\theta/2} & 0 \\ 0 & 0 & 0 & 1 \end{bmatrix} \quad (\text{C17})$$

in the basis states $|0\rangle_i|0\rangle_j$, $|0\rangle_i|1\rangle_j$, $|1\rangle_i|0\rangle_j$, and $|1\rangle_i|1\rangle_j$. These are also derived directly from Eq. (C10).

The two-qubit unitaries in Eqs. (C15), (C16), and (C17) can be implemented with the quantum circuit of the form in Fig. 16(c) with $\hat{u} = \hat{R}_X(\theta) = e^{-i\theta\hat{X}/2}$, $\hat{u} = \hat{R}_Y(\theta) = e^{-i\theta\hat{Y}/2}$, and $\hat{u} = \hat{R}_Z(\theta) = e^{-i\theta\hat{Z}/2}$, respectively. Notice that Eq. (C15) is identical with the exchange-type gate in Eq. (F7), and Eq. (C16) is identical with the Givens-rotation gate in Eqs. (117) and (118). Since the Jordan-Wigner string $\hat{Z}_{JW,ij}$ can be implemented as the sequences of CZ or fermionic SWAP gates, as shown in Fig. 4, the two-qubit unitary operators $e^{-i\theta\hat{h}_{ij}^{(a,1)}/2}$, $e^{-i\theta\hat{h}_{ij}^{(a,2)}/2}$, and $e^{-i\theta\hat{h}_{ij}^{(a,3)}/2}$ can also be implemented in quantum circuits.

3. Anomalous quadratic terms of fermion operators

A similar analysis can be made for a quadratic form of fermion operators that does not conserve the number of fermions (i.e., anomalous term):

$$\begin{aligned} \hat{h}_{ij}^{(a)} &= \begin{bmatrix} \hat{c}_i^\dagger & \hat{c}_j \end{bmatrix} \begin{bmatrix} a & b \\ b^* & -a \end{bmatrix} \begin{bmatrix} \hat{c}_i \\ \hat{c}_j^\dagger \end{bmatrix} \\ &= \text{Re}b (\hat{c}_i^\dagger \hat{c}_j^\dagger + \hat{c}_j \hat{c}_i) + i \text{Im}b (\hat{c}_i^\dagger \hat{c}_j^\dagger - \hat{c}_j \hat{c}_i) + a(\hat{n}_i + \hat{n}_j - 1) \\ &= \hat{h}_{ij}^{(a,1)} + \hat{h}_{ij}^{(a,2)} + \hat{h}_{ij}^{(a,3)}, \\ &\stackrel{\text{JWT}}{=} \frac{\text{Re}b}{2} (\hat{X}_i \hat{X}_j - \hat{Y}_i \hat{Y}_j) \hat{Z}_{JW,ij} + \frac{\text{Im}b}{2} (\hat{X}_i \hat{Y}_j + \hat{Y}_i \hat{X}_j) \hat{Z}_{JW,ij} \\ &\quad - \frac{a}{2} (\hat{Z}_i + \hat{Z}_j), \end{aligned} \quad (\text{C18})$$

where a and b are real and complex numbers, respectively, such that $a^2 + |b|^2 = 1$. $\hat{h}_{ij}^{(a,1)}$, $\hat{h}_{ij}^{(a,2)}$, and $\hat{h}_{ij}^{(a,3)}$ correspond to each term in Eq. (C18) and do not commute with each other. We shall now consider the exponentiated $\hat{h}_{ij}^{(a,1)}$, $\hat{h}_{ij}^{(a,2)}$, and $\hat{h}_{ij}^{(a,3)}$, i.e., $e^{-i\theta\hat{h}_{ij}^{(a,1)}/2}$, $e^{-i\theta\hat{h}_{ij}^{(a,2)}/2}$, and $e^{-i\theta\hat{h}_{ij}^{(a,3)}/2}$, and express these two-qubit unitary operators in quantum circuits.

For this purpose, it is useful to notice that

$$(\hat{c}_i^\dagger \hat{c}_j^\dagger + \hat{c}_j \hat{c}_i)^l = \begin{cases} \hat{c}_i^\dagger \hat{c}_j^\dagger + \hat{c}_j \hat{c}_i & \text{for } l \text{ odd,} \\ 2\hat{n}_i \hat{n}_j - (\hat{n}_i + \hat{n}_j) + 1 & \text{for } l \text{ even,} \end{cases} \quad (\text{C20})$$

$$i(\hat{c}_i^\dagger \hat{c}_j^\dagger - \hat{c}_j \hat{c}_i)^l = \begin{cases} i(\hat{c}_i^\dagger \hat{c}_j^\dagger - \hat{c}_j \hat{c}_i) & \text{for } l \text{ odd,} \\ 2\hat{n}_i \hat{n}_j - (\hat{n}_i + \hat{n}_j) + 1 & \text{for } l \text{ even,} \end{cases} \quad (\text{C21})$$

and

$$(\hat{n}_i + \hat{n}_j - 1)^l = \begin{cases} \hat{n}_i + \hat{n}_j - 1 & \text{for } l \text{ odd,} \\ 2\hat{n}_i \hat{n}_j - (\hat{n}_i + \hat{n}_j) + 1 & \text{for } l \text{ even,} \end{cases} \quad (\text{C22})$$

where l is positive integer, or equivalently in the qubit representation that

$$\left\{ \frac{1}{2} (\hat{X}_i \hat{X}_j - \hat{Y}_i \hat{Y}_j) \hat{Z}_{JW,ij} \right\}^l = \begin{cases} \frac{1}{2} (\hat{X}_i \hat{X}_j - \hat{Y}_i \hat{Y}_j) \hat{Z}_{JW,ij} & \text{for } l \text{ odd,} \\ \frac{1}{2} (1 + \hat{Z}_i \hat{Z}_j) & \text{for } l \text{ even,} \end{cases} \quad (\text{C23})$$

$$\left\{ \frac{1}{2} (\hat{X}_i \hat{Y}_j + \hat{Y}_i \hat{X}_j) \hat{Z}_{JW,ij} \right\}^l = \begin{cases} \frac{1}{2} (\hat{X}_i \hat{Y}_j + \hat{Y}_i \hat{X}_j) \hat{Z}_{JW,ij} & \text{for } l \text{ odd,} \\ \frac{1}{2} (1 + \hat{Z}_i \hat{Z}_j) & \text{for } l \text{ even,} \end{cases} \quad (\text{C24})$$

and

$$\left\{ \frac{1}{2} (\hat{Z}_j + \hat{Z}_i) \right\}^l = \begin{cases} \frac{1}{2} (\hat{Z}_j + \hat{Z}_i) & \text{for } l \text{ odd,} \\ \frac{1}{2} (1 + \hat{Z}_i \hat{Z}_j) & \text{for } l \text{ even,} \end{cases} \quad (\text{C25})$$

Note that Eqs. (C23) and (C24) also hold when the Jordan-Wigner string $\hat{Z}_{JW,ij}$ is absent in these equations.

Given that the Jordan-Wigner string $\hat{Z}_{JW,ij}$ commutes with the other operators in Eqs. (C23) and (C24), and $\hat{Z}_{JW,ij}^2 = 1$, the matrix representations

$$\frac{1}{2} (\hat{X}_i \hat{X}_j - \hat{Y}_i \hat{Y}_j) \doteq \begin{bmatrix} 0 & 0 & 0 & 1 \\ 0 & 0 & 0 & 0 \\ 0 & 0 & 0 & 0 \\ 1 & 0 & 0 & 0 \end{bmatrix}, \quad (\text{C26})$$

$$\frac{1}{2} (\hat{X}_i \hat{Y}_j + \hat{Y}_i \hat{X}_j) \doteq \begin{bmatrix} 0 & 0 & 0 & -i \\ 0 & 0 & 0 & 0 \\ 0 & 0 & 0 & 0 \\ i & 0 & 0 & 0 \end{bmatrix}, \quad (\text{C27})$$

$$\frac{1}{2} (\hat{Z}_j + \hat{Z}_i) \doteq \begin{bmatrix} 1 & 0 & 0 & 0 \\ 0 & 0 & 0 & 0 \\ 0 & 0 & 0 & 0 \\ 0 & 0 & 0 & -1 \end{bmatrix}, \quad (\text{C28})$$

and

$$\frac{1}{2} (1 + \hat{Z}_i \hat{Z}_j) \doteq \begin{bmatrix} 1 & 0 & 0 & 0 \\ 0 & 0 & 0 & 0 \\ 0 & 0 & 0 & 0 \\ 0 & 0 & 0 & 1 \end{bmatrix} \quad (\text{C29})$$

also confirm Eqs. (C23), (C24), and (C25). Here, the basis states $|0\rangle_i |0\rangle_j$, $|0\rangle_i |1\rangle_j$, $|1\rangle_i |0\rangle_j$, and $|1\rangle_i |1\rangle_j$ for the i th and j th qubits are assumed. Now it is obvious from the matrix representation that, these operators act as Pauli X , Y , Z , and identity I operators on the basis states $|0\rangle_i |0\rangle_j$ and $|1\rangle_i |1\rangle_j$ [see also Fig. 16(d)], and as zero on the basis states $|0\rangle_i |1\rangle_j$ and $|1\rangle_i |0\rangle_j$. Therefore, the exponentials of the matrices in Eqs. (C26)-(C28) are given by

$$\exp \left[-i \frac{\theta}{4} (\hat{X}_i \hat{X}_j - \hat{Y}_i \hat{Y}_j) \right] \doteq \begin{bmatrix} \cos \frac{\theta}{2} & 0 & 0 & -i \sin \frac{\theta}{2} \\ 0 & 1 & 0 & 0 \\ 0 & 0 & 1 & 0 \\ -i \sin \frac{\theta}{2} & 0 & 0 & \cos \frac{\theta}{2} \end{bmatrix}, \quad (\text{C30})$$

$$\exp \left[-i \frac{\theta}{4} (\hat{X}_i \hat{Y}_j + \hat{Y}_i \hat{X}_j) \right] \doteq \begin{bmatrix} \cos \frac{\theta}{2} & 0 & 0 & -\sin \frac{\theta}{2} \\ 0 & 1 & 0 & 0 \\ 0 & 0 & 1 & 0 \\ \sin \frac{\theta}{2} & 0 & 0 & \cos \frac{\theta}{2} \end{bmatrix}, \quad (\text{C31})$$

and

$$\exp \left[-i \frac{\theta}{4} (\hat{Z}_j + \hat{Z}_i) \right] \doteq \begin{bmatrix} e^{-i\theta/2} & 0 & 0 & 0 \\ 0 & 1 & 0 & 0 \\ 0 & 0 & 1 & 0 \\ 0 & 0 & 0 & e^{i\theta/2} \end{bmatrix} \quad (\text{C32})$$

in the basis states $|0\rangle_i|0\rangle_j$, $|0\rangle_i|1\rangle_j$, $|1\rangle_i|0\rangle_j$, and $|1\rangle_i|1\rangle_j$. These are also derived directly from Eq. (C10).

The two-qubit unitaries in Eqs. (C30), (C31), and (C32) can be implemented with the quantum circuit of the form in Fig. 16(d) with $\hat{u} = \hat{R}_X(\theta) = e^{-i\theta\hat{X}/2}$, $\hat{u} = \hat{R}_Y(\theta) = e^{-i\theta\hat{Y}/2}$, and $\hat{u} = \hat{R}_Z(\theta) = e^{-i\theta\hat{Z}/2}$, respectively. Notice that Eq. (C31) is identical with the Bogoliubov-transformation gate in Eqs. (127) and (128). Since the Jordan-Wigner string $\hat{Z}_{JW,ij}$ can be implemented as the sequences of CZ or fermionic SWAP gates, as shown in Fig. 4, the two-qubit unitary operators $e^{-i\theta\hat{h}_{ij}^{(a,1)}/2}$, $e^{-i\theta\hat{h}_{ij}^{(a,2)}/2}$, and $e^{-i\theta\hat{h}_{ij}^{(a,3)}/2}$ can also be implemented in quantum circuits.

Appendix D: Parallelization of VQE simulations

Here we briefly describe a simple way of parallelizing numerical simulations for the VQE method by separately and simultaneously evaluating derivatives of a variational state $|\Psi(\theta)\rangle$ with respect to variational parameters $\theta = \{\theta_k\}_{k=1}^{N_v}$. Figure 17 shows a schematic diagram of the parallelization strategy. In this scheme, the variational state $|\Psi(\theta)\rangle$ and its derivatives $|\partial_{\theta_k}\Psi(\theta)\rangle$ are calculated independently in each process. All these derivatives are then sent to process 0 to compute the energy gradient $\nabla E_0(\theta)$ and the metric tensor $\mathbf{G}(\theta)$. Finally, the variational parameters $\theta = \{\theta_k\}_{k=1}^{N_v}$ are updated accordingly to the NGD scheme in process 0. Note that one can simply omit the computation of the metric tensor $\mathbf{G}(\theta)$ when the GD method is used. The updated variational parameters are distributed from process 0 to all other processes (i.e., process 1, process 2, \dots , process N_v) for the next iteration. Continue this procedure until the convergence is achieved. In the schematic diagram shown in Fig. 17, we assume for simplicity that $d_{\mathcal{U}} = 1$ without projection operators and the number N_{proc} of processes is equal to $N_v + 1$. However, generalization of the parallelization scheme is straightforward for the case of $d_{\mathcal{U}} > 1$ and $N_{\text{proc}} \neq N_v + 1$.

Figure 18 shows the speedup as a function of N_{proc} for the case of $N_v = 56$. The variational state used here is the full-projected state $\mathcal{P}|\psi(\theta)\rangle$ with $N_{S,\text{azimuth}} = N_{\eta,\text{azimuth}} = 6$, $N_{S,\text{polar}} = N_{\eta,\text{polar}} = 4$, $D = 2$, and $d_{\mathcal{U}} = 1$, and the numerical simulations are performed on supercomputer FUGAKU at RIKEN at R-CCS. We use 6-thread OpenMP parallelization in each process and MPI between different processes. As shown in Fig. 18, an efficient speedup is obtained with increasing N_{proc} . This simple parallelization strategy is practical for small- to medium-size (e.g., $N \leq 30$) problems where a state vector can be stored in the memory of a single node and hence communications between different processes do not occur during the computation of the derivatives of the state (see Fig. 17). For larger problems where a state vector must be distributed over the memories on a distributed-memory system, massively parallel quantum-computer simulators for distributed memory systems, such as that in Ref. [123], will be promising.

Appendix E: Normalization factor of a symmetry-projected state in the fidelity calculation

Here, we show that the normalization factor due to the projection operator in a symmetry-projected state has to be treated with care in the fidelity calculation. For simplicity, let us assume the Krylov-subspace dimension $d_{\mathcal{U}} = 1$. In this case, the normalized approximated ground state is given by

$$|\Psi_{\mathcal{U}}^{(0)}(\theta)\rangle = \frac{\hat{\mathcal{P}}|\psi(\theta)\rangle}{\sqrt{\langle\psi(\theta)|\hat{\mathcal{P}}|\psi(\theta)\rangle}}, \quad (\text{E1})$$

and hence the fidelity reads

$$F(\theta) = \frac{|\langle\Psi_0|\hat{\mathcal{P}}|\psi(\theta)\rangle|^2}{\langle\psi(\theta)|\hat{\mathcal{P}}|\psi(\theta)\rangle}, \quad (\text{E2})$$

where

$$\hat{\mathcal{P}}^2 = \hat{\mathcal{P}} \quad (\text{E3})$$

is used for the normalization of $|\Psi_{\mathcal{U}}^{(0)}(\theta)\rangle$ in Eq. (E1). By substituting Eq. (84) into Eq. (E2), we obtain

$$F(\theta) = \frac{2\eta + 1}{2} \frac{2S + 1}{2} \frac{d_{\alpha}}{|\mathcal{G}|} \times \frac{\left| \sum_{j,l,m} w_{j,\eta} w_{l,S} P_{\eta} P_S [\chi^{(\alpha)}]^* \langle\Psi_0|e^{-i\beta_{j,\eta}\hat{\eta}_j} e^{-i\beta_{l,S}\hat{S}_l} \hat{g}_m|\psi(\theta)\rangle \right|^2}{\sum_{j,l,m} w_{j,\eta} w_{l,S} P_{\eta} P_S [\chi^{(\alpha)}]^* \langle\psi(\theta)|e^{-i\beta_{j,\eta}\hat{\eta}_j} e^{-i\beta_{l,S}\hat{S}_l} \hat{g}_m|\psi(\theta)\rangle}. \quad (\text{E4})$$

Namely, because of the mismatch of the power exponents between the matrix elements of the projection operator $\hat{\mathcal{P}}$ in the numerator and the denominator on the right-hand side of Eq. (E2), the normalization factor $(2\eta + 1)(2S + 1)d_{\alpha}/4|\mathcal{G}|$ due to the projection operator remains in Eq. (E4).

On the other hand, the expectation value of an observable \hat{A} that commutes with the projection operator, $[\hat{A}, \hat{\mathcal{P}}] = 0$, can be evaluated as

$$\langle\Psi_{\mathcal{U}}^{(0)}(\theta)|\hat{A}|\Psi_{\mathcal{U}}^{(0)}(\theta)\rangle = \frac{\langle\psi(\theta)|\hat{A}\hat{\mathcal{P}}|\psi(\theta)\rangle}{\langle\psi(\theta)|\hat{\mathcal{P}}|\psi(\theta)\rangle}. \quad (\text{E5})$$

Examples of \hat{A} include $\hat{A} = \hat{\mathcal{H}}$, \hat{S}^2 , and $\hat{\eta}^2$. Since the power exponents of the matrix elements involving the projection operator $\hat{\mathcal{P}}$ in the numerator and the denominator on the right-hand side of Eq. (E5) are the same, the normalization factor due to the projection operator is irrelevant for the evaluation of Eq. (E5).

Appendix F: Hamiltonian variational ansatz

In this appendix, the HVA method [105, 106] is used to simulate the two-component Fermi-Hubbard model described by

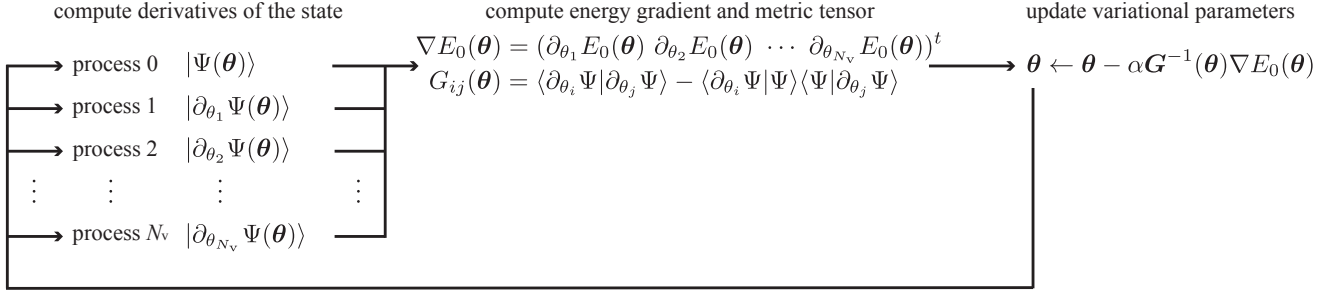


FIG. 17. Schematic diagram for a parallelization strategy of the VQE simulation with the NGD optimization. Here, in this diagram, we assume that $d_{ij} = 1$ without projection operators and the number N_{proc} of processes is $N_{\text{proc}} = N_v + 1$, for simplicity.

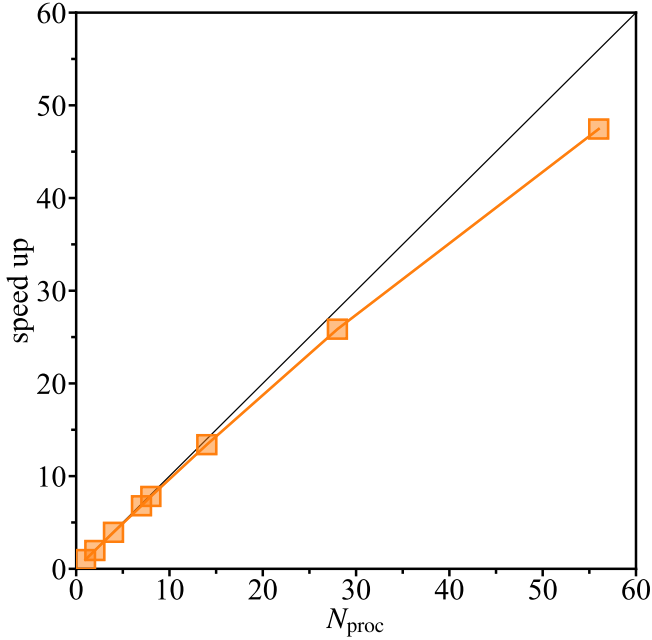


FIG. 18. Speedup as a function of the number N_{proc} of processes for the two-component Fermi-Hubbard model on the 4×2 cluster. The benchmark is taken on supercomputer FUGAKU at RIKEN R-CCS.

the Hamiltonian $\hat{\mathcal{H}}$ in Eq. (52) on the 4×2 cluster under open boundary conditions (see Fig. 1) at half filling. The HVA is a quantum circuit ansatz, based on a principle of the quantum approximate optimization algorithm (QAOA) [124], which is constructed by discretizing a quantum adiabatic process [125–131].

The HVA state $|\psi_{\text{HVA}}(\theta)\rangle$ adopted in this study is given by

$$|\psi_{\text{HVA}}(\theta)\rangle = \prod_{l=1}^D \hat{U}_{\text{HVA},l}(\theta_l) \hat{W}|0\rangle^{\otimes N}, \quad (\text{F1})$$

where $\theta = \{\theta_l\}_{l=1}^D$ with $\theta_l = \{\theta_{k,l}\}_{k=1}^6$ is a set of variational parameters and

$$\begin{aligned} \hat{U}_{\text{HVA},l}(\theta_l) &= \hat{U}_{t_4}(\theta_{6,l}) \hat{U}_{t_5}(\theta_{5,l}) \hat{U}_{t_2}(\theta_{4,l}) \hat{U}_{t_1}(\theta_{3,l}) \\ &\quad \times \hat{U}_{U_2}(\theta_{2,l}) \hat{U}_{U_1}(\theta_{1,l}) \end{aligned} \quad (\text{F2})$$

with $\hat{U}_{t_\alpha}(\theta) = e^{-i\theta \hat{t}_{t_\alpha}/2}$ and $\hat{U}_{U_\beta}(\theta) = e^{-i\theta \hat{U}_\beta/2}$ being unitary operators generated by hopping (t) and interaction (U_{H}) terms, respectively (see Fig. 19). For example, one of the former unitary operators is defined as

$$\hat{U}_{t_3}(\theta) = e^{-i\theta \hat{h}_{1,2}^\dagger/2} e^{-i\theta \hat{h}_{7,8}^\dagger/2} e^{-i\theta \hat{h}_{1,2}^\dagger/2} e^{-i\theta \hat{h}_{7,8}^\dagger/2} \quad (\text{F3})$$

with $\hat{h}_{i,j}^\sigma = -t(c_{i\sigma}^\dagger c_{j\sigma} + c_{j\sigma}^\dagger c_{i\sigma})$. With the Jordan-Wigner transformation,

$$e^{-i\theta \hat{h}_{i,j}^\sigma/2} \stackrel{\text{JWT}}{=} \exp \left[i \frac{t\theta}{4} (\hat{X}_{i\sigma} \hat{X}_{j\sigma} + \hat{Y}_{i\sigma} \hat{Y}_{j\sigma}) \hat{Z}_{\text{JW},i\sigma,i\sigma} \right] \quad (\text{F4})$$

$$= \left[\prod_{i\sigma \leq k \leq j\sigma} \widehat{\text{CZ}}_{j\sigma,k} \right] \hat{\mathcal{K}}_{i\sigma,j\sigma}(-t\theta) \left[\prod_{i\sigma \leq k \leq j\sigma} \widehat{\text{CZ}}_{j\sigma,k} \right] \quad (\text{F5})$$

$$\equiv \widehat{\mathcal{K}}_{i\sigma,j\sigma}(-t\theta), \quad (\text{F6})$$

where the CZ gates in Eq. (F5) account for the Jordan-Wigner string in Eq. (F4), as shown for the more general case in Eq. (109), and

$$\hat{\mathcal{K}}_{ij}(\theta) = \exp \left[-i \frac{\theta}{4} (\hat{X}_i \hat{X}_j + \hat{Y}_i \hat{Y}_j) \right] \quad (\text{F7})$$

is the exchange-type gate as in Eq. (C15) [also see Fig. 20(b)]. $\hat{U}_{U_\beta}(\theta)$ operators can be implemented in a quantum circuit by a product of the eZZ gates defined in Eq. (133) and Fig. 7(c).

Therefore, as shown in Fig. 20(a), there are six independent variational parameters $\{\theta_{i,l}\}_{i=1}^6$ for each layer l and hence $6D$ parameters in total for the HVA state $|\psi_{\text{HVA}}(\theta)\rangle$ composed of D layers. These variational parameters are optimized by the NGD method so as to minimize the expectation value of energy. Notice that the initial state $\hat{W}|0\rangle^{\otimes N}$ in $|\psi_{\text{HVA}}(\theta)\rangle$ is the ground state of $\hat{\mathcal{H}}_{t_3} + \hat{\mathcal{H}}_{t_4}$ and thus $|\psi_{\text{HVA}}(\theta)\rangle$ indeed follows a discretized version of a quantum adiabatic process in which an optimal unitary evolution path, i.e., $\theta = \{\theta_l\}_{l=1}^D$, is determined variationally. Notice also that as opposed to the parametrization adopted in Sec. VII A, here the same variational parameters are set for the parametrized gates that represent equivalent hopping bonds and on-site interaction sites. Apart from this difference, the quantum circuit considered here and that in Sec. VII A (also see Fig. 7) are essentially

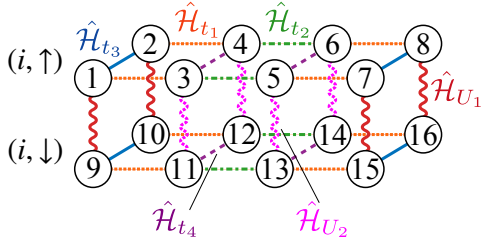


FIG. 19. In the HVA, the Fermi-Hubbard Hamiltonian \hat{H} on the 4×2 cluster is divided into six parts \hat{H}_{t_1} , \hat{H}_{t_2} , \hat{H}_{t_3} , \hat{H}_{t_4} , \hat{H}_{U_1} , and \hat{H}_{U_2} , where \hat{H}_{t_1} , \hat{H}_{t_2} , \hat{H}_{t_3} , and \hat{H}_{t_4} are the hopping (t) terms between sites connected by different types of bonds (indicated by orange dotted, green dash-dotted, blue solid, and purple dashed lines, respectively), and \hat{H}_{U_1} and \hat{H}_{U_2} are the interaction (U_H) terms on nonequivalent sites (indicated by red solid curly and magenta dashed curly lines, respectively). Circles represent qubits that are numbered from 1 to 8 for single-particle states at site $i (= 1, 2, \dots, 8)$ with spin up and from 9 to 16 for single-particle states at site $i (= 1, 2, \dots, 8)$ with spin down.

the same if $\hat{U}_{i_a}(\theta) = e^{-i\hat{f}_{i_a}\theta/2}$ in $|\psi_{\text{HVA}}(\theta)\rangle$ is replaced with the parametrized exponentiated fermionic-SWAP operator in

Eq. (130) and Fig. 7(b).

In the numerical simulations, we set the learning rate $\tau = 0.005/t$ in the NGD optimization because we have found that the optimization tends to be less stable if we use the same learning rate $\tau = 0.025/t$ as in the numerical simulations for the Krylov-extended SAVQE method shown in Sec. VII C. Figure 21 shows the ground-state energy, the ground-state fidelity, and the expectation values of total spin squared and total η squared as a function of the optimization iteration x . The results are averaged over 64 independent calculations with different sets of initial parameters, each of which is randomly distributed in $[-0.05, 0.05]$. It is found that the ground-state energy and fidelity are improved systematically with increasing D . As expected, the total spin squared $\langle \hat{S}^2 \rangle_{\theta^{(x)}}$ and the total eta squared $\langle \hat{\eta}^2 \rangle_{\theta^{(x)}}$ are always zero, independently of the optimization iteration x .

-
- [1] Y. Nakamura, Yu A. Pashkin, and J. S. Tsai, “Coherent control of macroscopic quantum states in a single-Cooper-pair box,” *Nature* **398**, 786–788 (1999).
- [2] Pieter Kok, W. J. Munro, Kae Nemoto, T. C. Ralph, Jonathan P. Dowling, and G. J. Milburn, “Linear optical quantum computing with photonic qubits,” *Rev. Mod. Phys.* **79**, 135–174 (2007).
- [3] T. D. Ladd, F. Jelezko, R. Laflamme, Y. Nakamura, C. Monroe, and J. L. O’Brien, “Quantum computers,” *Nature* **464**, 45–53 (2010).
- [4] Ze-Liang Xiang, Sahel Ashhab, J. Q. You, and Franco Nori, “Hybrid quantum circuits: Superconducting circuits interacting with other quantum systems,” *Rev. Mod. Phys.* **85**, 623–653 (2013).
- [5] Jerry M. Chow, Jay M. Gambetta, Easwar Magesan, David W. Abraham, Andrew W. Cross, B. R. Johnson, Nicholas A. Masluk, Colm A. Ryan, John A. Smolin, Srikanth J. Srinivasan, and M. Steffen, “Implementing a strand of a scalable fault-tolerant quantum computing fabric,” *Nature Communications* **5**, 4015 (2014).
- [6] R. Barends, J. Kelly, A. Megrant, A. Veitia, D. Sank, E. Jeffrey, T. C. White, J. Mutus, A. G. Fowler, B. Campbell, Y. Chen, Z. Chen, B. Chiaro, A. Dunsworth, C. Neill, P. O’Malley, P. Roushan, A. Vainsencher, J. Wenner, A. N. Korotkov, A. N. Cleland, and John M. Martinis, “Superconducting quantum circuits at the surface code threshold for fault tolerance,” *Nature* **508**, 500–503 (2014).
- [7] D. Ristè, S. Poletto, M.-Z. Huang, A. Bruno, V. Vesterinen, O.-P. Saira, and L. DiCarlo, “Detecting bit-flip errors in a logical qubit using stabilizer measurements,” *Nature Communications* **6**, 6983 (2015).
- [8] J. Kelly, R. Barends, A. G. Fowler, A. Megrant, E. Jeffrey, T. C. White, D. Sank, J. Y. Mutus, B. Campbell, Yu Chen, Z. Chen, B. Chiaro, A. Dunsworth, I.-C. Hoi, C. Neill, P. J. J. O’Malley, C. Quintana, P. Roushan, A. Vainsencher, J. Wenner, A. N. Cleland, and John M. Martinis, “State preservation by repetitive error detection in a superconducting quantum circuit,” *Nature* **519**, 66–69 (2015).
- [9] Frank Arute, Kunal Arya, Ryan Babbush, Dave Bacon, Joseph C. Bardin, Rami Barends, Rupak Biswas, Sergio Boixo, Fernando G. S. L. Brandao, David A. Buell, Brian Burkett, Yu Chen, Zijun Chen, Ben Chiaro, Roberto Collins, William Courtney, Andrew Dunsworth, Edward Farhi, Brooks Foxen, Austin Fowler, Craig Gidney, Marissa Giustina, Rob Graff, Keith Guerin, Steve Habegger, Matthew P. Harrigan, Michael J. Hartmann, Alan Ho, Markus Hoffmann, Trent Huang, Travis S. Humble, Sergei V. Isakov, Evan Jeffrey, Zhang Jiang, Dvir Kafri, Kostyantyn Kechedzhi, Julian Kelly, Paul V. Klimov, Sergey Knysh, Alexander Korotkov, Fedor Kostritsa, David Landhuis, Mike Lindmark, Erik Lucero, Dmitry Lyakh, Salvatore Mandrà, Jarrod R. McClean, Matthew McEwen, Anthony Megrant, Xiao Mi, Kristel Michielsen, Masoud Mohseni, Josh Mutus, Ofer Naaman, Matthew Neeley, Charles Neill, Murphy Yuezhen Niu, Eric Ostby, Andre Petukhov, John C. Platt, Chris Quintana, Eleanor G. Rieffel, Pedram Roushan, Nicholas C. Rubin, Daniel Sank, Kevin J. Satzinger, Vadim Smelyanskiy, Kevin J. Sung, Matthew D. Trevithick, Amit Vainsencher, Benjamin Vallalonga, Theodore White, Z. Jamie Yao, Ping Yeh, Adam Zalcman, Hartmut Neven, and John M. Martinis, “Quantum supremacy using a programmable superconducting processor,” *Nature* **574**, 505–510 (2019).
- [10] Han-Sen Zhong, Hui Wang, Yu-Hao Deng, Ming-Cheng Chen, Li-Chao Peng, Yi-Han Luo, Jian Qin, Dian Wu, Xing Ding, Yi Hu, Peng Hu, Xiao-Yan Yang, Wei-Jun Zhang, Hao Li, Yuxuan Li, Xiao Jiang, Lin Gan, Guangwen Yang, Lixing You, Zhen Wang, Li Li, Nai-Le Liu, Chao-Yang Lu, and Jian-Wei Pan, “Quantum computational advantage using photons,”

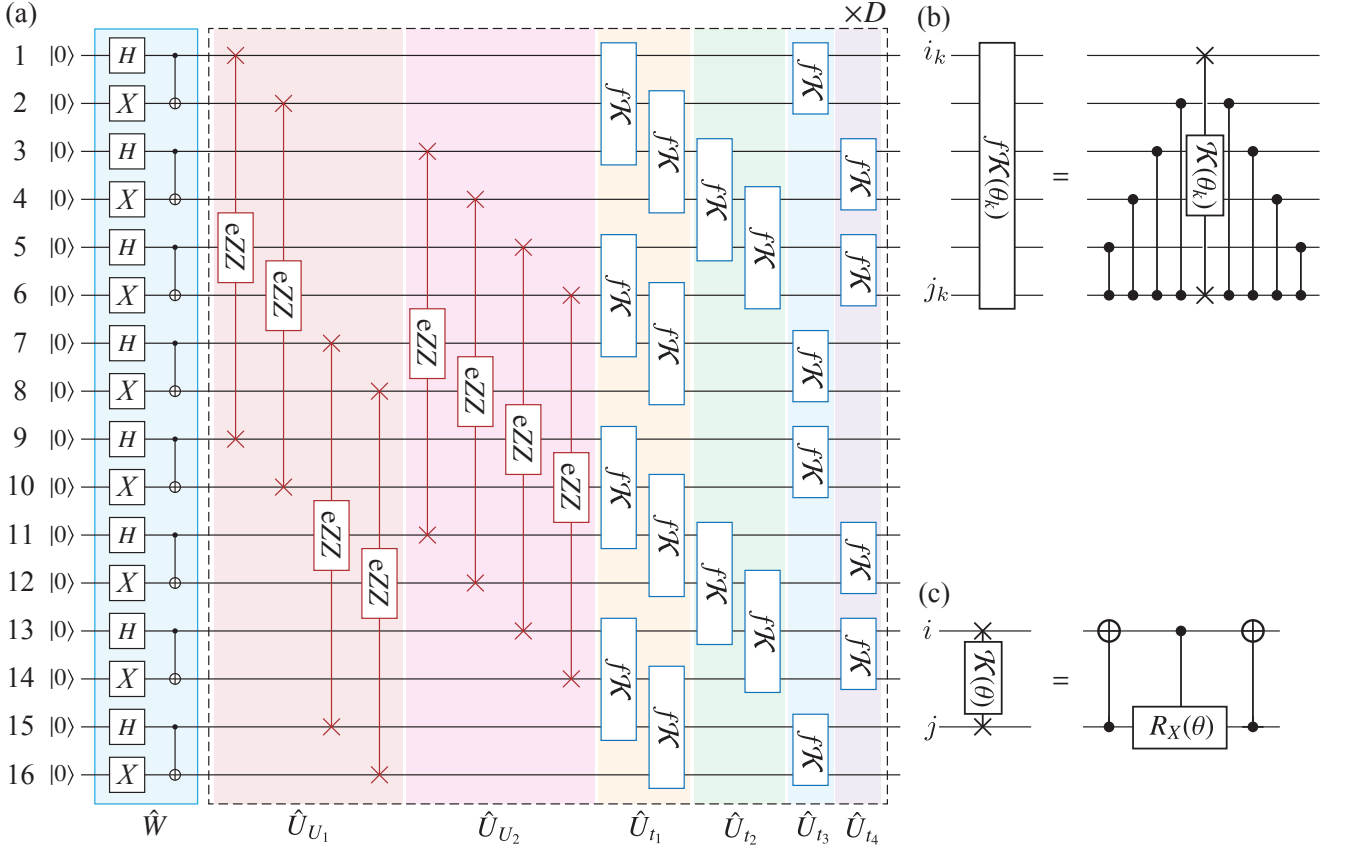


FIG. 20. (a) A quantum circuit for preparing the HVA state $|\psi_{\text{HVA}}(\theta)\rangle = \prod_{l=D}^1 \hat{U}_{\text{HVA},l}(\theta) \hat{W}|0\rangle^{\otimes N}$ with $\hat{U}_{\text{HVA},l}(\theta) = \hat{U}_{t_4}(\theta_{6,l}) \hat{U}_{t_3}(\theta_{5,l}) \hat{U}_{t_2}(\theta_{4,l}) \hat{U}_{t_1}(\theta_{3,l}) \hat{U}_{U_2}(\theta_{2,l}) \hat{U}_{U_1}(\theta_{1,l})$. $f\mathcal{K}$ denotes a fermionic exchange gate $f\mathcal{K}_{ij}(\theta)$ acting on qubits i and j with $\theta = -t\theta_{k,l}$ [132], defined in Eq. (F6). eZZ denotes a gate $\exp(-i\hat{Z}_i\hat{Z}_j\theta/2)$ acting on qubits i and j with $\theta = U_{\text{H}}\theta_{k,l}/4$ [132], defined in Eq. (I33) and Fig. 7(c). The qubit numbers indicated in the left most side correspond to the numbering of qubits in Fig. 19 for the two-component Fermi-Hubbard model on the 4×2 cluster. (b) A decomposition of a fermionic exchange gate $f\mathcal{K}(\theta)$ into an exchange gate $\mathcal{K}(\theta)$ sandwiched with CZ gates, as in Eq. (F5). (c) A decomposition of the exchange gate $\mathcal{K}(\theta)$ defined in Eq. (F7). Here, $\hat{R}_X(\theta) = e^{-i\theta\hat{X}_i/2}$ acting on qubit i .

Science **370**, 1460–1463 (2020).

- [11] Alexandre Blais, Arne L. Grimsmo, S. M. Girvin, and Andreas Wallraff, “Circuit quantum electrodynamics,” *Rev. Mod. Phys.* **93**, 025005 (2021).
- [12] Richard P. Feynman, “Simulating physics with computers,” *International Journal of Theoretical Physics* **21**, 467–488 (1982).
- [13] Frank Arute, Kunal Arya, Ryan Babbush, Dave Bacon, Joseph C. Bardin, Rami Barends, Andreas Bengtsson, Sergio Boixo, Michael Broughton, Bob B. Buckley, David A. Buell, Brian Burkett, Nicholas Bushnell, Yu Chen, Zijun Chen, Yu-An Chen, Ben Chiaro, Roberto Collins, Stephen J. Cotton, William Courtney, Sean Demura, Alan Derk, Andrew Dunsworth, Daniel Eppens, Thomas Eckl, Catherine Erickson, Edward Farhi, Austin Fowler, Brooks Foxen, Craig Gidney, Marissa Giustina, Rob Graff, Jonathan A. Gross, Steve Habegger, Matthew P. Harrigan, Alan Ho, Sabrina Hong, Trent Huang, William Huggins, Lev B. Ioffe, Sergei V. Isakov, Evan Jeffrey, Zhang Jiang, Cody Jones, Dvir Kafri, Kostyantyn Kechedzhi, Julian Kelly, Seon Kim, Paul V. Klimov, Alexander N. Korotkov, Fedor Kostritsa, David Landhuis, Pavel Laptev, Mike Lindmark, Erik Lucero, Michael Marthaler, Orion Martin, John M. Martinis, Anika Maruszczyk, Sam McArdle, Jarrod R. McClean, Trevor McCourt, Matt McEwen, Anthony Megrant, Carlos Mejuto-Zaera, Xiao Mi, Masoud Mohseni, Wojciech Mroczkiewicz, Josh Mutus, Ofer Naaman, Matthew Neeley, Charles Neill, Hartmut Neven, Michael Newman, Murphy Yuezhen Niu, Thomas E. O’Brien, Eric Ostby, Bálint Pató, Andre Petukhov, Harald Putterman, Chris Quintana, Jan-Michael Reiner, Pedram Roushan, Nicholas C. Rubin, Daniel Sank, Kevin J. Satzinger, Vadim Smelyanskiy, Doug Strain, Kevin J. Sung, Peter Schmitteckert, Marco Szalay, Norm M. Tubman, Amit Vainsencher, Theodore White, Nicolas Vogt, Z. Jamie Yao, Ping Yeh, Adam Zalcman, and Sebastian Zanker, “Observation of separated dynamics of charge and spin in the Fermi-Hubbard model,” (2020), [arXiv:2010.07965](https://arxiv.org/abs/2010.07965) [quant-ph].
- [14] Stasja Stanisic, Jan Lukas Bosse, Filippo Maria Gambetta, Raul A. Santos, Wojciech Mroczkiewicz, Thomas E. O’Brien, Eric Ostby, and Ashley Montanaro, “Observing ground-state properties of the Fermi-Hubbard model using a scalable algorithm on a quantum computer,” (2021), [arXiv:2112.02025](https://arxiv.org/abs/2112.02025) [quant-ph].
- [15] John Preskill, “Quantum Computing in the NISQ era and beyond,” *Quantum* **2**, 79 (2018).

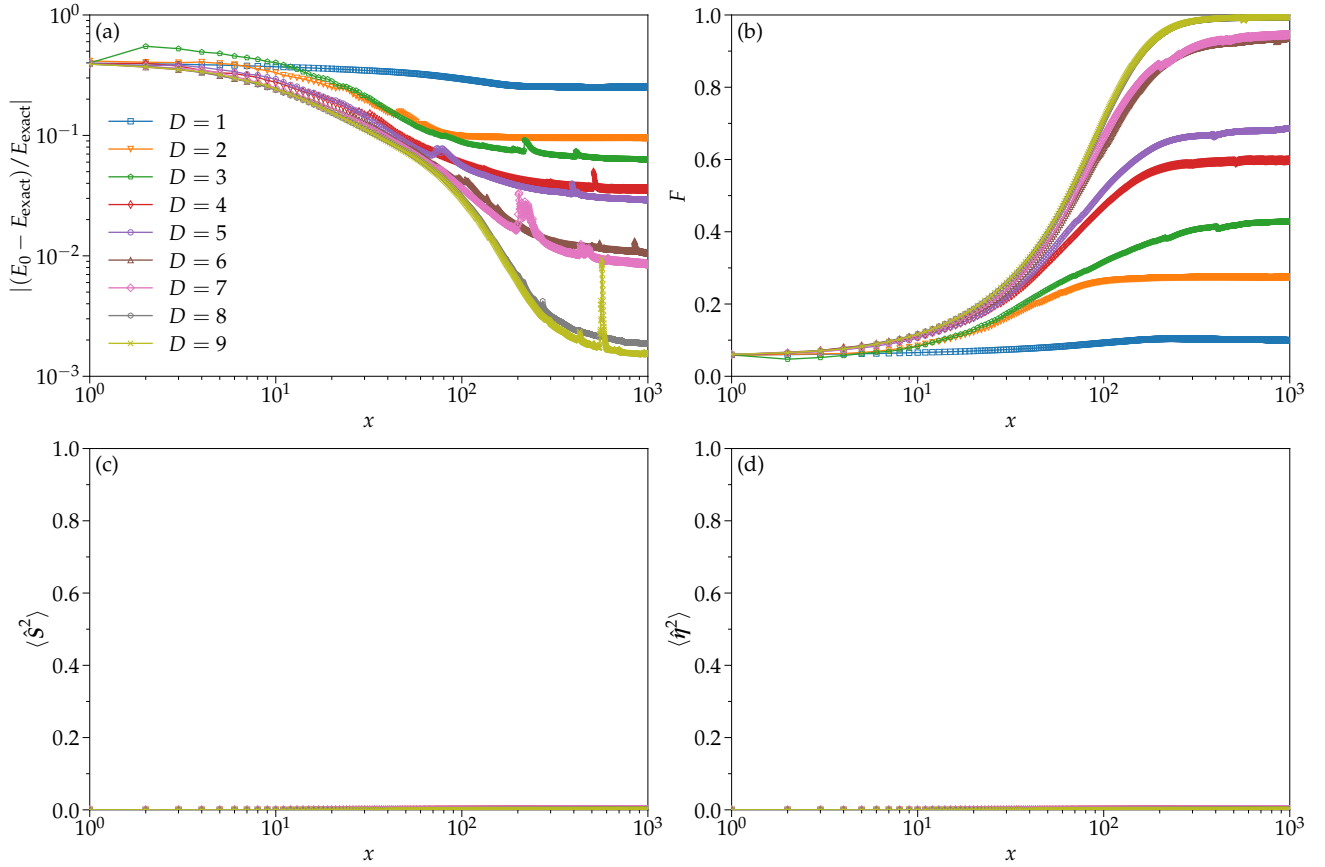


FIG. 21. (a) The ground-state energy $E_0(\theta^{(x)})$, (b) the ground-state fidelity $F(\theta^{(x)})$, (c) the expectation value of total spin squared $\langle \hat{S}^2 \rangle_{\theta^{(x)}}$, and (d) the expectation value of total η squared $\langle \hat{\eta}^2 \rangle_{\theta^{(x)}}$ as a function of the optimization iteration x obtained by the HVA for different D . Each result with a different value of D is obtained by averaging over 64 independent calculations started with 64 different sets of random initial parameters $\theta^{(1)}$. The spiky behavior is occasionally observed in the ground-state energy $E_0(\theta^{(x)})$ during the parameter optimization iteration. This is due to the same reason described in the caption of Fig. 13.

- [16] Cupjin Huang, Fang Zhang, Michael Newman, Junjie Cai, Xun Gao, Zhengxiong Tian, Junyin Wu, Haihong Xu, Huanjun Yu, Bo Yuan, Mario Szegedy, Yaoyun Shi, and Jianxin Chen, “Classical simulation of quantum supremacy circuits,” (2020), [arXiv:2005.06787 \[quant-ph\]](https://arxiv.org/abs/2005.06787).
- [17] D. Nigg, M. Müller, E. A. Martinez, P. Schindler, M. Hennrich, T. Monz, M. A. Martin-Delgado, and R. Blatt, “Quantum computations on a topologically encoded qubit,” *Science* **345**, 302–305 (2014), <https://www.science.org/doi/pdf/10.1126/science.1253742>.
- [18] Alexander Erhard, Hendrik Poulsen Nautrup, Michael Meth, Lukas Postler, Roman Stricker, Martin Stadler, Vlad Negnevitsky, Martin Ringbauer, Philipp Schindler, Hans J. Briegel, Rainer Blatt, Nicolai Friis, and Thomas Monz, “Entangling logical qubits with lattice surgery,” *Nature* **589**, 220–224 (2021).
- [19] K. J. Satzinger, Y.-J. Liu, A. Smith, C. Knapp, M. Newman, C. Jones, Z. Chen, C. Quintana, X. Mi, A. Dunsworth, and et al., “Realizing topologically ordered states on a quantum processor,” *Science* **374**, 1237–1241 (2021).
- [20] J. F. Marques, B. M. Varbanov, M. S. Moreira, H. Ali, N. Muthusubramanian, C. Zachariadis, F. Battistel, M. Beekman, N. Haider, W. Vlothuizen, A. Bruno, B. M. Terhal, and L. DiCarlo, “Logical-qubit operations in an error-detecting surface code,” *Nature Physics* (2021), [10.1038/s41567-021-01423-9](https://doi.org/10.1038/s41567-021-01423-9).
- [21] Janine Hilder, Daniel Pijn, Oleksiy Onishchenko, Alexander Stahl, Maximilian Orth, Björn Lekitsch, Andrea Rodriguez-Blanco, Markus Müller, Ferdinand Schmidt-Kaler, and Ulrich Poschinger, “Fault-tolerant parity readout on a shuttling-based trapped-ion quantum computer,” (2021), [arXiv:2107.06368 \[quant-ph\]](https://arxiv.org/abs/2107.06368).
- [22] Ying Li and Simon C. Benjamin, “Efficient variational quantum simulator incorporating active error minimization,” *Phys. Rev. X* **7**, 021050 (2017).
- [23] Suguru Endo, Simon C. Benjamin, and Ying Li, “Practical quantum error mitigation for near-future applications,” *Phys. Rev. X* **8**, 031027 (2018).
- [24] X. Bonet-Monroig, R. Sagastizabal, M. Singh, and T. E. O’Brien, “Low-cost error mitigation by symmetry verification,” *Phys. Rev. A* **98**, 062339 (2018).
- [25] Suguru Endo, Qi Zhao, Ying Li, Simon Benjamin, and Xiaoyuan, “Mitigating algorithmic errors in a hamiltonian simulation,” *Phys. Rev. A* **99**, 012334 (2019).
- [26] M.-H. Yung, J. Casanova, A. Mezzacapo, J. McClean, L. Lamata, A. Aspuru-Guzik, and E. Solano, “From transistor to trapped-ion computers for quantum chemistry,” *Scientific Reports* **4**, 3589 (2014).

- [27] Alberto Peruzzo, Jarrod McClean, Peter Shadbolt, Man-Hong Yung, Xiao-Qi Zhou, Peter J. Love, Alán Aspuru-Guzik, and Jeremy L. O’Brien, “A variational eigenvalue solver on a photonic quantum processor,” *Nature Communications* **5**, 4213 (2014).
- [28] Jarrod R. McClean, Jonathan Romero, Ryan Babbush, and Alán Aspuru-Guzik, “The theory of variational hybrid quantum-classical algorithms,” *New Journal of Physics* **18**, 023023 (2016).
- [29] Abhinav Kandala, Antonio Mezzacapo, Kristan Temme, Maika Takita, Markus Brink, Jerry M. Chow, and Jay M. Gambetta, “Hardware-efficient variational quantum eigensolver for small molecules and quantum magnets,” *Nature* **549**, 242 (2017).
- [30] Suguru Endo, Zhenyu Cai, Simon C. Benjamin, and Xiao Yuan, “Hybrid quantum-classical algorithms and quantum error mitigation,” *Journal of the Physical Society of Japan* **90**, 032001 (2021), <https://doi.org/10.7566/JPSJ.90.032001>.
- [31] M. Cerezo, Andrew Arrasmith, Ryan Babbush, Simon C. Benjamin, Suguru Endo, Keisuke Fujii, Jarrod R. McClean, Kosuke Mitarai, Xiao Yuan, Lukasz Cincio, and Patrick J. Coles, “Variational quantum algorithms,” *Nature Reviews Physics* **3**, 625–644 (2021).
- [32] Jules Tilly, Hongxiang Chen, Shuxiang Cao, Dario Picozzi, Kanav Setia, Ying Li, Edward Grant, Leonard Wossnig, Ivan Rungger, George H. Booth, and Jonathan Tennyson, “The variational quantum eigensolver: a review of methods and best practices,” (2021), [arXiv:2111.05176 \[quant-ph\]](https://arxiv.org/abs/2111.05176).
- [33] J. I. Colless, V. V. Ramasesh, D. Dahlen, M. S. Blok, M. E. Kimchi-Schwartz, J. R. McClean, J. Carter, W. A. de Jong, and I. Siddiqi, “Computation of Molecular Spectra on a Quantum Processor with an Error-Resilient Algorithm,” *Phys. Rev. X* **8**, 011021 (2018).
- [34] Ken M. Nakanishi, Kosuke Mitarai, and Keisuke Fujii, “Subspace-search variational quantum eigensolver for excited states,” *Phys. Rev. Research* **1**, 033062 (2019).
- [35] Kentaro Heya, Ken M. Nakanishi, Kosuke Mitarai, and Keisuke Fujii, “Subspace Variational Quantum Simulator,” (2019), [arXiv:1904.08566 \[quant-ph\]](https://arxiv.org/abs/1904.08566).
- [36] F. Chatelin, *Eigenvalues of Matrices* (SIAM, Philadelphia, 2012).
- [37] Robert M. Parrish and Peter L. McMahon, “Quantum Filter Diagonalization: Quantum Eigendecomposition without Full Quantum Phase Estimation,” (2019), [arXiv:1909.08925 \[quant-ph\]](https://arxiv.org/abs/1909.08925).
- [38] William J. Huggins, Joonho Lee, Unpil Baek, Bryan O’Gorman, and K. Birgitta Whaley, “A non-orthogonal variational quantum eigensolver,” *New Journal of Physics* **22**, 073009 (2020).
- [39] Nicholas H. Stair, Renke Huang, and Francesco A. Evangelista, “A Multireference Quantum Krylov Algorithm for Strongly Correlated Electrons,” *Journal of Chemical Theory and Computation* **16**, 2236–2245 (2020).
- [40] Mario Motta, Chong Sun, Adrian T. K. Tan, Matthew J. O’Rourke, Erika Ye, Austin J. Minnich, Fernando G. S. L. Brandão, and Garnet Kin-Lic Chan, “Determining eigenstates and thermal states on a quantum computer using quantum imaginary time evolution,” *Nature Physics* (2019), [10.1038/s41567-019-0704-4](https://doi.org/10.1038/s41567-019-0704-4).
- [41] Kübra Yeter-Aydeniz, Raphael C. Pooser, and George Siopsis, “Practical quantum computation of chemical and nuclear energy levels using quantum imaginary time evolution and Lanczos algorithms,” *npj Quantum Information* **6**, 63 (2020).
- [42] Kazuhiro Seki and Seiji Yunoki, “Quantum power method by a superposition of time-evolved states,” *PRX Quantum* **2**, 010333 (2021).
- [43] Kazuhiro Seki, Tomonori Shirakawa, and Seiji Yunoki, “Symmetry-adapted variational quantum eigensolver,” *Phys. Rev. A* **101**, 052340 (2020).
- [44] Guglielmo Mazzola, Pauline J. Ollitrault, Panagiotis Kl. Barkoutsos, and Ivano Tavernelli, “Nonunitary operations for ground-state calculations in near-term quantum computers,” *Phys. Rev. Lett.* **123**, 130501 (2019).
- [45] Takashi Tsuchimochi, Yuto Mori, and Seiichiro L. Ten-no, “Spin-projection for quantum computation: A low-depth approach to strong correlation,” *Phys. Rev. Research* **2**, 043142 (2020).
- [46] Pooja Siwach and Denis Lacroix, “Filtering states with total spin on a quantum computer,” *Phys. Rev. A* **104**, 062435 (2021).
- [47] Armin Khamoshi, Francesco A. Evangelista, and Gustavo E. Scuseria, “Correlating agp on a quantum computer,” *Quantum Science and Technology* **6**, 014004 (2020).
- [48] E. A. Ruiz Guzman and D. Lacroix, “Accessing ground state and excited states energies in many-body system after symmetry restoration using quantum computers,” (2021), [arXiv:2111.13080 \[quant-ph\]](https://arxiv.org/abs/2111.13080).
- [49] Jie Liu, Lingyun Wan, Zhenyu Li, and Jinlong Yang, “Simulating periodic systems on quantum computer,” (2020), [arXiv:2008.02946 \[quant-ph\]](https://arxiv.org/abs/2008.02946).
- [50] David Zsolt Manrique, Irfan T. Khan, Kentaro Yamamoto, Vijja Wichitwechkarn, and David Muñoz Ramo, “Momentum-space unitary couple cluster and translational quantum subspace expansion for periodic systems on quantum computers,” (2020), [arXiv:2008.08694 \[quant-ph\]](https://arxiv.org/abs/2008.08694).
- [51] Nobuyuki Yoshioka, Takeshi Sato, Yuya O. Nakagawa, Yu-ya Ohnishi, and Wataru Mizukami, “Variational quantum simulation for periodic materials,” *Phys. Rev. Research* **4**, 013052 (2022).
- [52] Ilya G. Ryabinkin, Scott N. Genin, and Artur F. Izmaylov, “Constrained variational quantum eigensolver: Quantum computer search engine in the fock space,” *Journal of Chemical Theory and Computation* **15**, 249–255 (2019), pMID: 30512959, <https://doi.org/10.1021/acs.jctc.8b00943>.
- [53] Kohdai Kuroiwa and Yuya O. Nakagawa, “Penalty methods for a variational quantum eigensolver,” *Phys. Rev. Research* **3**, 013197 (2021).
- [54] Shun-Ichi Amari, “Natural gradient works efficiently in learning,” *Neural Comput.* **10**, 251–276 (1998).
- [55] J. P. Provost and G. Vallee, “Riemannian structure on manifolds of quantum states,” *Comm. Math. Phys.* **76**, 289–301 (1980).
- [56] Michael Kolodrubetz, Dries Sels, Pankaj Mehta, and Anatoli Polkovnikov, “Geometry and non-adiabatic response in quantum and classical systems,” *Physics Reports* **697**, 1 – 87 (2017), geometry and non-adiabatic response in quantum and classical systems.
- [57] James Stokes, Josh Izaac, Nathan Killoran, and Giuseppe Carleo, “Quantum Natural Gradient,” *Quantum* **4**, 269 (2020).
- [58] Koen Ruymbeek, Karl Meerbergen, and Wim Michiels, “Calculating the minimal/maximal eigenvalue of symmetric parameterized matrices using projection,” *Numerical Linear Algebra with Applications* **26**, e2263 (2019).
- [59] L. I. Schiff, *Quantum Mechanics*, 1st ed. (McGraw-Hill, New York, 1949) Chap. 25.
- [60] Jun Li, Xiaodong Yang, Xinhua Peng, and Chang-Pu Sun, “Hybrid Quantum-Classical Approach to Quantum Optimal Control,” *Phys. Rev. Lett.* **118**, 150503 (2017).

- [61] K. Mitarai, M. Negoro, M. Kitagawa, and K. Fujii, “Quantum circuit learning,” *Phys. Rev. A* **98**, 032309 (2018).
- [62] Maria Schuld, Ville Bergholm, Christian Gogolin, Josh Izaac, and Nathan Killoran, “Evaluating analytic gradients on quantum hardware,” *Phys. Rev. A* **99**, 032331 (2019).
- [63] Karol Kowalski and Bo Peng, “Quantum simulations employing connected moments expansions,” *The Journal of Chemical Physics* **153**, 201102 (2020).
- [64] Harish J. Vallury, Michael A. Jones, Charles D. Hill, and Lloyd C. L. Hollenberg, “Quantum computed moments correction to variational estimates,” *Quantum* **4**, 373 (2020).
- [65] Daniel Claudino, Bo Peng, Nicholas P Bauman, Karol Kowalski, and Travis S Humble, “Improving the accuracy and efficiency of quantum connected moments expansions,” *Quantum Science and Technology* **6**, 034012 (2021).
- [66] Tatiana A. Bespalova and Oleksandr Kyriienko, “Hamiltonian Operator Approximation for Energy Measurement and Ground-State Preparation,” *PRX Quantum* **2**, 030318 (2021).
- [67] Guillermo González, Rahul Trivedi, and J. Ignacio Cirac, “Quantum algorithms for powering stable hermitian matrices,” *Phys. Rev. A* **103**, 062420 (2021).
- [68] Joseph C. Aulicino, Trevor Keen, and Bo Peng, “State preparation and evolution in quantum computing: A perspective from Hamiltonian moments,” *International Journal of Quantum Chemistry* **n/a**, e26853, <https://onlinelibrary.wiley.com/doi/pdf/10.1002/qua.26853>.
- [69] H. F. Trotter, “On the product of semi-groups of operators,” *Proc. Am. Math. Soc.* **10**, 545 (1959).
- [70] Masuo Suzuki, “Generalized Trotter’s formula and systematic approximants of exponential operators and inner derivations with applications to many-body problems,” *Comm. Math. Phys.* **51**, 183–190 (1976).
- [71] P. Jordan and E. Wigner, “Über das Paulische Äquivalenzverbot,” *Zeitschrift für Physik* **47**, 631–651 (1928).
- [72] Sergio Rodriguez, “Linear Antiferromagnetic Chain,” *Phys. Rev.* **116**, 1474–1477 (1959).
- [73] Chen Ning Yang, “ η pairing and off-diagonal long-range order in a Hubbard model,” *Phys. Rev. Lett.* **63**, 2144–2147 (1989).
- [74] Hal Tasaki, *Physics and Mathematics of Quantum Many-Body Systems* (Springer International Publishing, 2020) Chap. 9.
- [75] Hiroyuki Shiba, “Thermodynamic Properties of the One-Dimensional Half-Filled-Band Hubbard Model. II: Application of the Grand Canonical Method,” *Progress of Theoretical Physics* **48**, 2171–2186 (1972).
- [76] Yi-Zhuang You, Andreas W. W. Ludwig, and Cenke Xu, “Sachdev-Ye-Kitaev model and thermalization on the boundary of many-body localized fermionic symmetry-protected topological states,” *Phys. Rev. B* **95**, 115150 (2017).
- [77] Seher Karakuzu, Kazuhiro Seki, and Sandro Sorella, “Study of the superconducting order parameter in the two-dimensional negative- U Hubbard model by grand-canonical twist-averaged boundary conditions,” *Phys. Rev. B* **98**, 075156 (2018).
- [78] Ryo Fujiuchi, Tatsuya Kaneko, Koudai Sugimoto, Seiji Yunoki, and Yukinori Ohta, “Superconductivity and charge density wave under a time-dependent periodic field in the one-dimensional attractive Hubbard model,” *Phys. Rev. B* **101**, 235122 (2020).
- [79] Kai Li, “ η -pairing in correlated fermion models with spin-orbit coupling,” *Phys. Rev. B* **102**, 165150 (2020).
- [80] Elliott H. Lieb, “Two theorems on the hubbard model,” *Phys. Rev. Lett.* **62**, 1201–1204 (1989).
- [81] Teturo Inui, Yukito Tanabe, and Yoshitaka Onodera, *Group Theory and Its Applications in Physics* (Springer, Heidelberg, 1990).
- [82] P. Ring and P. Schuck, *The Nuclear Many-Body Problem* (Springer, Heidelberg, 1980).
- [83] K.W. Schmid, “On the use of general symmetry-projected hartree-fock-bogoliubov configurations in variational approaches to the nuclear many-body problem,” *Progress in Particle and Nuclear Physics* **52**, 565–633 (2004).
- [84] Takahiro Mizusaki and Masatoshi Imada, “Quantum-number projection in the path-integral renormalization group method,” *Phys. Rev. B* **69**, 125110 (2004).
- [85] Benjamin Bally and Michael Bender, “Projection on particle number and angular momentum: Example of triaxial bogoliubov quasiparticle states,” *Phys. Rev. C* **103**, 024315 (2021).
- [86] Morris E. Rose, *Elementary Theory of Angular Momentum* (Wiley, New York, 1957).
- [87] Eugene P. Wigner, *Group Theory and Its Application to the Quantum Mechanical* (Academic press, New York, 1959).
- [88] D A Varshalovich, A N Moskalev, and V K Khersonskii, *Quantum Theory of Angular Momentum* (World Scientific, 1988).
- [89] Daisuke Tahara and Masatoshi Imada, “Variational monte carlo method combined with quantum-number projection and multi-variable optimization,” *Journal of the Physical Society of Japan* **77**, 114701 (2008).
- [90] Sergey B. Bravyi and Alexei Yu. Kitaev, “Fermionic quantum computation,” *Annals of Physics* **298**, 210 – 226 (2002).
- [91] Fabian H. L. Essler, Holger Frahm, Frank Göhmann, Andreas Klümper, and Vladimir E. Korepin, *The One-Dimensional Hubbard Model* (Cambridge University Press, New York, 2005).
- [92] Frank Verstraete, J. Ignacio Cirac, and José I. Latorre, “Quantum circuits for strongly correlated quantum systems,” *Phys. Rev. A* **79**, 032316 (2009).
- [93] Thomas Barthel, Carlos Pineda, and Jens Eisert, “Contraction of fermionic operator circuits and the simulation of strongly correlated fermions,” *Phys. Rev. A* **80**, 042333 (2009).
- [94] Dave Wecker, Matthew B. Hastings, Nathan Wiebe, Bryan K. Clark, Chetan Nayak, and Matthias Troyer, “Solving strongly correlated electron models on a quantum computer,” *Phys. Rev. A* **92**, 062318 (2015).
- [95] Ian D. Kivlichan, Jarrod McClean, Nathan Wiebe, Craig Gidney, Alán Aspuru-Guzik, Garnet Kin-Lic Chan, and Ryan Babbush, “Quantum Simulation of Electronic Structure with Linear Depth and Connectivity,” *Phys. Rev. Lett.* **120**, 110501 (2018).
- [96] Matthew B. Hastings, Dave Wecker, Bela Bauer, and Matthias Troyer, “Improving quantum algorithms for quantum chemistry,” *Quantum Inf. Comput.* **15**, 1–21 (2015).
- [97] Jan-Michael Reiner, Frank Wilhelm-Mauch, Gerd Schön, and Michael Marthaler, “Finding the ground state of the Hubbard model by variational methods on a quantum computer with gate errors,” *Quantum Science and Technology* **4**, 035005 (2019).
- [98] David C. McKay, Stefan Filipp, Antonio Mezzacapo, Easwar Magesan, Jerry M. Chow, and Jay M. Gambetta, “Universal Gate for Fixed-Frequency Qubits via a Tunable Bus,” *Phys. Rev. Applied* **6**, 064007 (2016).
- [99] E. M. Stoudenmire and Steven R. White, “Minimally entangled typical thermal state algorithms,” *New Journal of Physics* **12**, 055026 (2010).
- [100] Zhenyu Cai, “Resource Estimation for Quantum Variational Simulations of the Hubbard Model,” *Phys. Rev. Applied* **14**, 014059 (2020).

- [101] Chris Cade, Lana Mineh, Ashley Montanaro, and Stasja Stanisic, “Strategies for solving the fermi-hubbard model on near-term quantum computers,” *Phys. Rev. B* **102**, 235122 (2020).
- [102] Zhang Jiang, Kevin J. Sung, Kostyantyn Kechedzhi, Vadim N. Smelyanskiy, and Sergio Boixo, “Quantum Algorithms to Simulate Many-Body Physics of Correlated Fermions,” *Phys. Rev. Applied* **9**, 044036 (2018).
- [103] Michael A Nielsen and Isaac L Chuang, *Quantum Computation and Quantum Information* (Cambridge University Press, New York, 2000).
- [104] Jarrod R. McClean, Sergio Boixo, Vadim N. Smelyanskiy, Ryan Babbush, and Hartmut Neven, “Barren plateaus in quantum neural network training landscapes,” *Nature Communications* **9**, 4812 (2018).
- [105] Dave Wecker, Matthew B. Hastings, and Matthias Troyer, “Progress towards practical quantum variational algorithms,” *Phys. Rev. A* **92**, 042303 (2015).
- [106] Roeland Wiersema, Cunlu Zhou, Yvette de Sereville, Juan Felipe Carrasquilla, Yong Baek Kim, and Henry Yuen, “Exploring entanglement and optimization within the hamiltonian variational ansatz,” *PRX Quantum* **1**, 020319 (2020).
- [107] Hao Shi, Carlos A. Jiménez-Hoyos, R. Rodríguez-Guzmán, Gustavo E. Scuseria, and Shiwei Zhang, “Symmetry-projected wave functions in quantum monte carlo calculations,” *Phys. Rev. B* **89**, 125129 (2014).
- [108] Fabian H. L. Essler, Vladimir E. Korepin, and Kareljan Schoutens, “Complete solution of the one-dimensional hubbard model,” *Phys. Rev. Lett.* **67**, 3848–3851 (1991).
- [109] Sota Kitamura and Hideo Aoki, “ η -pairing superfluid in periodically-driven fermionic hubbard model with strong attraction,” *Phys. Rev. B* **94**, 174503 (2016).
- [110] Tatsuya Kaneko, Tomonori Shirakawa, Sandro Sorella, and Seiji Yunoki, “Photoinduced η Pairing in the Hubbard Model,” *Phys. Rev. Lett.* **122**, 077002 (2019).
- [111] Satoshi Ejima, Tatsuya Kaneko, Florian Lange, Seiji Yunoki, and Holger Fehske, “Photoinduced η -pairing at finite temperatures,” *Phys. Rev. Research* **2**, 032008 (2020).
- [112] Daniel K. Mark and Olexei I. Motrunich, “ η -pairing states as true scars in an extended hubbard model,” *Phys. Rev. B* **102**, 075132 (2020).
- [113] Sanjay Moudgalya, Nicolas Regnault, and B. Andrei Bernevig, “ η -pairing in hubbard models: From spectrum generating algebras to quantum many-body scars,” *Phys. Rev. B* **102**, 085140 (2020).
- [114] Masaya Nakagawa, Naoto Tsuji, Norio Kawakami, and Masahito Ueda, “ η pairing of light-emitting fermions: Nonequilibrium pairing mechanism at high temperatures,” (2021), arXiv:2103.13624 [cond-mat.quant-gas].
- [115] Hirokazu Tsunetsugu, Manfred Sigrist, and Kazuo Ueda, “The ground-state phase diagram of the one-dimensional kondo lattice model,” *Rev. Mod. Phys.* **69**, 809–864 (1997).
- [116] Tomonori Shirakawa, Shohei Miyakoshi, and Seiji Yunoki, “Photoinduced η pairing in the Kondo lattice model,” *Phys. Rev. B* **101**, 174307 (2020).
- [117] Hironobu Yoshida and Hoshio Katsura, “Exact eigenstates of extended $SU(N)$ Hubbard models: Generalization of η -pairing states with N -particle off-diagonal long-range order,” *Phys. Rev. B* **105**, 024520 (2022).
- [118] Dorje C. Brody and Lane P. Hughston, “Geometric quantum mechanics,” *Journal of Geometry and Physics* **38**, 19–53 (2001).
- [119] Samuel L. Braunstein and Carlton M. Caves, “Statistical distance and the geometry of quantum states,” *Phys. Rev. Lett.* **72**, 3439–3443 (1994).
- [120] Seiji Yunoki and Sandro Sorella, “Two spin liquid phases in the spatially anisotropic triangular Heisenberg model,” *Phys. Rev. B* **74**, 014408 (2006).
- [121] Naoki Yamamoto, “On the natural gradient for variational quantum eigensolver,” (2019), arXiv:1909.05074 [quant-ph].
- [122] Adriano Barenco, Charles H. Bennett, Richard Cleve, David P. DiVincenzo, Norman Margolus, Peter Shor, Tycho Sleator, John A. Smolin, and Harald Weinfurter, “Elementary gates for quantum computation,” *Phys. Rev. A* **52**, 3457–3467 (1995).
- [123] Hans De Raedt, Fengping Jin, Dennis Willsch, Madita Willsch, Naoki Yoshioka, Nobuyasu Ito, Shengjun Yuan, and Kristel Michielsen, “Massively parallel quantum computer simulator, eleven years later,” *Computer Physics Communications* **237**, 47–61 (2019).
- [124] Edward Farhi, Jeffrey Goldstone, and Sam Gutmann, “A Quantum Approximate Optimization Algorithm,” arXiv e-prints, arXiv:1411.4028 (2014), arXiv:1411.4028 [quant-ph].
- [125] R. Barends, L. Lamata, J. Kelly, L. García-Álvarez, A. G. Fowler, A. Megrant, E. Jeffrey, T. C. White, D. Sank, J. Y. Mutus, B. Campbell, Yu Chen, Z. Chen, B. Chiaro, A. Dunswoth, I.-C. Hoi, C. Neill, P. J. J. O’Malley, C. Quintana, P. Roushan, A. Vainsencher, J. Wenner, E. Solano, and John M. Martinis, “Digital quantum simulation of fermionic models with a superconducting circuit,” *Nature Communications* **6**, 7654 (2015).
- [126] R. Barends, A. Shabani, L. Lamata, J. Kelly, A. Mezza-capo, U. Las Heras, R. Babbush, A. G. Fowler, B. Campbell, Yu Chen, Z. Chen, B. Chiaro, A. Dunswoth, E. Jeffrey, E. Lucero, A. Megrant, J. Y. Mutus, M. Neeley, C. Neill, P. J. J. O’Malley, C. Quintana, P. Roushan, D. Sank, A. Vainsencher, J. Wenner, T. C. White, E. Solano, H. Neven, and John M. Martinis, “Digitized adiabatic quantum computing with a superconducting circuit,” *Nature* **534**, 222–226 (2016).
- [127] Wen Wei Ho and Timothy H. Hsieh, “Efficient variational simulation of non-trivial quantum states,” *SciPost Phys.* **6**, 29 (2019).
- [128] Glen Bigan Mbeng, Rosario Fazio, and Giuseppe Santoro, “Quantum Annealing: a journey through Digitalization, Control, and hybrid Quantum Variational schemes,” arXiv e-prints, arXiv:1906.08948 (2019), arXiv:1906.08948 [quant-ph].
- [129] Glen Bigan Mbeng, Rosario Fazio, and Giuseppe E. Santoro, “Optimal quantum control with digitized Quantum Annealing,” arXiv e-prints, arXiv:1911.12259 (2019), arXiv:1911.12259 [quant-ph].
- [130] Matteo M. Wauters, Glen Bigan Mbeng, and Giuseppe E. Santoro, “Polynomial scaling of QAOA for ground-state preparation of the fully-connected p-spin ferromagnet,” arXiv e-prints, arXiv:2003.07419 (2020), arXiv:2003.07419 [quant-ph].
- [131] Tomonori Shirakawa, Kazuhiro Seki, and Seiji Yunoki, “Discretized quantum adiabatic process for free fermions and comparison with the imaginary-time evolution,” *Phys. Rev. Research* **3**, 013004 (2021).
- [132] Since θ_{k_i} are variational parameters to be optimized, the prefactors such as $-t$ and $U_H/4$ are not important in practice.